AGU PUBLICATIONS

Geochemistry, Geophysics, Geosystems

RESEARCH ARTICLE
10.1002/2013GC005132

Diverse magmatic effects of subducting a hot slab in SW Japan: Results from forward modeling

Jun-Ichi Kimura[1], James B. Gill[2], Tomoyuki Kunikiyo[3], Isaku Osaka[4], Yusuke Shimoshioiri[5], Maiko Katakuse[6], Susumu Kakubuchi[7], Takashi Nagao[8], Katsuhiko Furuyama[9], Atsushi Kamei[10], Hiroshi Kawabata[11], Junichi Nakajima[12], Peter E. van Keken[13], and Robert J. Stern[14]

[1]Institute for Research on Earth Evolution, Japan Agency for Marine-Earth Science and Technology, Yokosuka, Japan, [2]Department of Earth and Planetary Sciences, University of California Santa Cruz, Santa Cruz, California, USA, [3]WORLD Survey and Design Co. Ltd., Izumo, Japan, [4]IZUTEC Co. Ltd., Izumo, Japan, [5]TANAKA AI (SHANGHAI) Co., Ltd., Shanghai, China, [6]The General Environmental TECHNOS Co. Ltd., Osaka, Japan, [7]Department of Geology, Saga University, Saga, Japan, [8]Department of Geosciences, Yamaguchi University, Yamaguchi, Japan, [9]Department of Geosciences, Osaka City University, Osaka, Japan, [10]Department of Geoscience, Shimane University, Matsue, Japan, [11]Multidisciplinary Science Cluster, Kochi University, Kochi, Japan, [12]Research Center for Prediction of Earthquakes and Volcanic Eruptions, Graduate School of Science, Tohoku University, Sendai, Japan, [13]Department of Earth and Environmental Sciences, University of Michigan, Ann Arbor, Michigan, USA, [14]Geoscience Department, University of Texas at Dallas, Richardson, Texas, USA

Key Points:
- Slab melts generate various magma types in SW Japan arc
- Numerical mass balance geochemical model revealed source conditions of magmas
- Origin of magma genesis between hot and cold subduction zones is discussed

Supporting Information:
- Readme
- Auxiliary Materials 1-8

Correspondence to:
J.-I. Kimura,
jkimura@jamstec.go.jp

Citation:
Kimura, J.-I., et al. (2014), Diverse magmatic effects of subducting a hot slab in SW Japan: Results from forward modeling, *Geochem. Geophys. Geosyst.*, *15*, 691–739, doi:10.1002/2013GC005132.

Received 6 NOV 2013
Accepted 29 JAN 2014
Accepted article online 5 FEB 2014
Published online 26 MAR 2014

Abstract In response to the subduction of the young Shikoku Basin of the Philippine Sea Plate, arc magmas erupted in SW Japan throughout the late Cenozoic. Many magma types are present including ocean island basalt (OIB), shoshonite (SHO), arc-type alkali basalt (AB), typical subalkalic arc basalt (SAB), high-Mg andesite (HMA), and adakite (ADK). OIB erupted since the Japan Sea back-arc basin opened, whereas subsequent arc magmas accompanied subduction of the Shikoku Basin. However, there the origin of the magmas in relation to hot subduction is debated. Using new major and trace element and Sr-Nd-Pb-Hf isotope analyses of 324 lava samples from seven Quaternary volcanoes, we investigated the genetic conditions of the magma suites using a geochemical mass balance model, Arc Basalt Simulator version 4 (ABS4), that uses these data to solve for the parameters such as pressure/temperature of slab dehydration/melting and slab flux fraction, pressure, and temperature of mantle melting. The calculations suggest that those magmas originated from slab melts that induced flux melting of mantle peridotite. The suites differ mostly in the mass fraction of slab-melt flux, increasing from SHO through AB, SAB, HMA, to ADK. The pressure and temperature of mantle melting decreases in the same order. The suites differ secondarily in the ratio of altered oceanic crust to sediment in the source of the slab melt. The atypical suites associated with hot subduction result from unusually large mass fractions of slab melt and unusually cool mantle temperatures.

1. Introduction

The origin of arc magmas remains a central research subject because of its fundamental role in element redistributions in the Earth. This process contributes to the formation of continental crust and element recycling back into the mantle as key components of the Earth's geochemical cycles [*Gill*, 1981; *Kelemen et al*., 2013; *Tatsumi and Eggins*, 1995; *Tatsumi et al*., 2008a]. The sources and processes of arc magmatism vary in part because the geophysical conditions differ considerably between subduction systems [*Syracuse et al*., 2010; *van Keken et al*., 2011].

Among subduction zones worldwide, the late Cenozoic Southwest (SW) Japan arc is an extreme hot end-member having been formed as a result of subducting the young Shikoku Basin of the Philippine Sea Plate [*Kimura et al*., 2005a; *Peacock and Wang*, 1999; *Syracuse et al*., 2010]. Magma compositions in hot arcs differ remarkably from those in cold subduction systems, such as the NE Japan or Izu arcs, where low-K tholeiitic to medium and high-K calc-alkaline magmas are dominant [*Kimura et al*., 2009, 2010; *Tatsumi et al*., 2008b; *Tollstrup et al*., 2010]. In the SW Japan arc, ocean island-type basalt (OIB), arc-type alkali basalt (AB) and shoshonite (SHO), typical subalkalic arc basalt (SAB), high-Mg andesites (HMA), and adakite (ADK) all occur in close proximity [*Iwamori*, 1991; *Kakubuchi et al*., 2000; *Kimura et al*., 2005a; *Morris*, 1995; *Tatsumi and Koyaguchi*, 1989;

Tatsumi and Hanyu, 2003]. This occurrence of multiple magma types is a common feature of hot subduction zones such as Cascadia (OIB, HMA, adakitic dacite) [*Leeman et al*., 2005; *Streck et al*., 2007], Baja California (transitional mafic lavas between alkali basalt and HMA (bajaites), and adakitic dacite) [*Calmus et al*., 2003], and Central Mexico (OIB and adakitic dacite) [*Straub et al*., 2008, 2011]. However, the occurrence of almost all the magma suites, excluding only low-K tholeiite, makes the SW Japan arc unique.

Many models have been proposed for magma genesis in the SW Japan arc. The models include an enriched lithospheric mantle origin of OIB [*Hoang and Uto*, 2003; *Kakubuchi et al*., 2000], aqueous fluid-fluxed mantle melting for AB [*Iwamori*, 1991, 1992], carbonaceous melt-fluxed melting for Miocene OIB [*Tatsumi et al*., 1999], hydrous shallow mantle melting with residual phlogopite for SHO [*Tatsumi and Koyaguchi*, 1989], slab melt-fluxed mantle melting for HMA [*Kimura et al*., 2005a; *Shimoda et al*., 1998; *Tatsumi and Hanyu*, 2003], slab melting for ADK [*Feineman et al*., 2013; *Kimura et al*., 2005a; *Morris*, 1995], remelting of solidified andesite for ADK [*Tamura et al*., 2003], and deep garnet fractionation of hydrous basalt for ADK [*Zellmer et al*., 2012].

These models have been based on limited geochemical data sets. In this paper, we present thorough analytical results for 324 lava samples from seven Quaternary eruption centers that are representative of almost all the magma suites erupted in SW Japan during the Quaternary. We then quantitatively reexamine the proposed models based on the new data set. For this, we use a new version of a forward geochemical mass balance model, Arc Basalt Simulator version 4 (ABS4). The first author (JIK) and coworkers have been developing the ABS model for a decade. The previous version, ABS version 3 (ABS3), has been applied successfully to the low-K tholeiite and medium-K calc-alkaline basalts of the cold NE Japan and North Izu subduction zones [*Kimura et al*., 2009, 2010], low-Ca boninite and high-Mg ADK in the infant Izu-Bonin-Mariana (IBM) arc [*Li et al*., 2013], and calc-alkaline basalts of the Southern Volcanic Zone of Chile [*Jacques et al*., 2013] We summarize the improvements in the ABS4 model in Appendix.

2. Rock Suites

We first introduce the seven rock suites and four subsuites that are examined in this paper. These are OIB (containing OIBL and OIBH), SAB, SHO, AB (containing ABL and ABH), HMA, ADK, and AA. The geochemical criteria for discriminating between the suites are discussed in section 6.

1. *OIB*: Ocean island basalt-type alkali basalt occurs at the Kannabe and Abu monogenetic volcano clusters (Figure 1). All Quaternary basalts at the Kannabe Volcano Group [*Furuyama et al*., 1993b] are OIB, whereas only some in the Abu Monogenetic Volcano Group are [*Kakubuchi et al*., 2000]. OIB at Kannabe is divided into OIBL and OIBH based on Sr isotope ratios that are lower in OIBL than OIBH.

2. *SAB*: Medium-K subalkalic arc basalt and their differentiates also occur in the Abu Monogenetic Volcano Group (Figure 1).

3. *SHO*: Shoshonitic basalt (absarokite) also occurs in the Abu Monogenetic Volcano Group, at Katamata [*Tatsumi and Koyaguchi*, 1989] (Figure 1).

4. *AB*: Arc-type alkali basalt occurs at the Yokota monogenetic volcano [*Fujibayashi et al*., 1989] (Figure 1) (included in Daisen by *Tamura et al*. [2000]). AB is divided into ABL and ABH on the basis of Sr isotope ratios that are lower in ABL than ABH. These two subtypes are the equivalents of the high-Nd and low-Nd isotope groups of *Nagao et al*. [1990].

5. *HMA*: This is the first report of high-Mg andesite at Kasayama and Nagasawadai in the Abu Monogenetic Volcano Group (Figure 1) [*Kakubuchi et al*., 2000]. We compare them to the Middle Miocene Setouchi HMA (~13 Ma) [*Tatsumi and Hanyu*, 2003].

6. *ADK*: Adakite [*Kimura et al*., 2005a; *Morris*, 1995] occurs at the Aonoyama monogenetic volcanoes [*Furuyama et al*., 2002] (hereafter Aono), and at Daisen volcano and the Hiruzen Volcano Group [*Tsukui et al*., 1985] (hereafter collectively called Daisen). We refer to them as Aono ADK and Daisen ADK, respectively (Figure 1).

7. *AA*: Aphyric andesite possessing adakite affinities occur at Daisen Volcano [*Tsukui et al*., 1985].

For completeness, supporting information 2 includes analytical results for a few other locations (e.g., Kurayoshi) and minor rock suites (e.g., Setouchi SAB) that are not discussed in this paper.

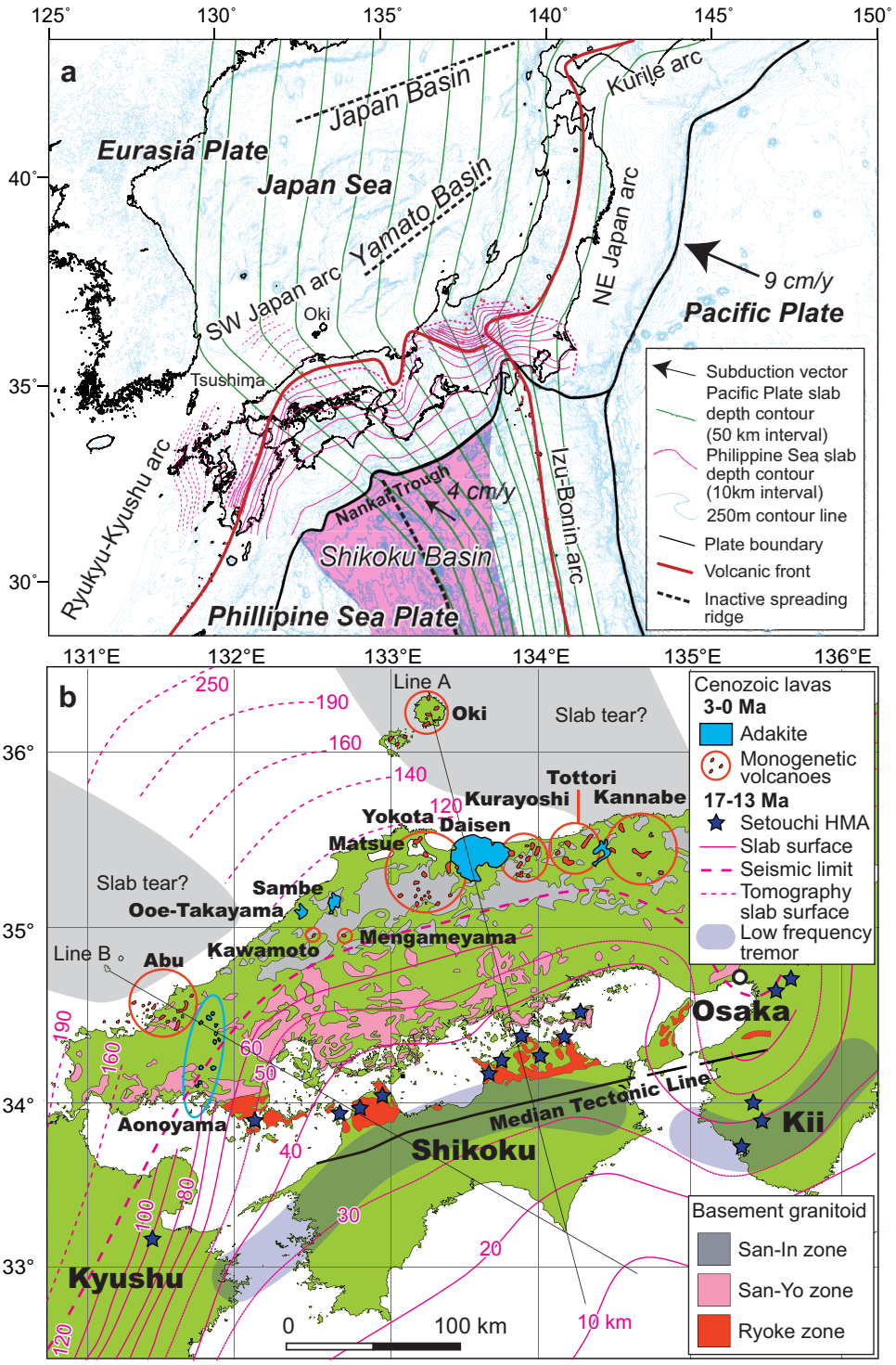

Figure 1. Tectonic setting and distribution of the late Cenozoic volcanoes in the SW Japan arc. (a) The Quaternary volcanic arc develops in response to the subduction of the Shikoku Basin of the Philippine Sea Plate slab in the SW Japan arc. (b) The Quaternary volcanoes consist of basalt monogenetic volcano clusters and adakitic dacite eruption centers. Eruption centers of the Miocene Setouch high-Mg andesites are also shown. The Quaternary volcanic centers are subparallel to the seismic-aseismic transition of the Shikoku Basin plate slab. The aseismic slab can be traced tomographically to 370 km deep beneath the Japan Sea as shown by short-dashed lines [*Zhao et al.*, 2012]. Slab tear windows are also imaged (see shaded areas in Figure 1b). Also shown are regions of low-frequency tremors above the slab beneath Shikoku [*Obara*, 2002]. Lines A and B are positions of cross sections shown in Figure 17. Seismicity contours are from *Nakajima and Hasegawa* [2007]. Basement granitoid distribution is from *Kagami et al.* [1992].

3. Geological Setting and Arc Evolution

3.1. Basement Terranes and Late Cenozoic Tectonic Development

The SW Japan arc is located along the eastern continental margin of the Eurasia Plate beneath which the Shikoku Basin of the Philippine Sea Plate is subducting [*Kimura et al*., 2005a] (Figure 1a). The basement of the arc consists of subparallel Permian to early Cenozoic accretionary prism sedimentary rocks [*Maruyama et al*., 2009]. Large volumes of granitoids intruded the basement terranes during the late Cretaceous to early Oligocene (120–30 Ma) (Figure 1b). They are classified into the Ryoke, San-Yo, and San-In zones based on their Sr-Nd isotope geochemistry. The Ryoke and the San-Yo Zone granitoids have enriched sources whereas the San-In Zone granitoids have more depleted sources [*Ikawa et al*., 1999; *Imaoka et al*., 2011; *Ishioka and Iizumi*, 2003; *Kagami and Imaoka*, 2008; *Kagami et al*., 1988, 1992, 2000; *Kimura et al*., 2005a; *Matsumoto et al*., 1994; *Resanov et al*., 1994; *Takagi and Kagami*, 1995; *Yuge et al*., 1998; *Yuhara et al*., 1998, 2003] (Figure 2). Cooling ages in the San-Yo and San-In Zones are 70–45 Ma, and in the San-In Zone are 40–30 Ma [*Imaoka et al*., 2011].

The youngest plutonic activity is regarded as a precursor to the opening of the Japan Sea. There was associated volcanic activity at 27–17 Ma [*Kimura et al*., 2005a; *Miyake*, 1994; *Uto et al*., 1994]. These lavas are mostly rift-related alkalic to tholeiitic basalt [*Pouclet et al*., 1995], but there are also small amounts of ADK and HMA in the northeast and central Japan rear arc that have been interpreted as the result of melting the Pacific Plate slab during back-arc rifting [*Sato et al*., 2013; *Yamamoto and Hoang*, 2009].

3.2. Volcanic Activity and Tectonics in the Middle Miocene to Pliocene

Volcanism in the current SW Japan arc started in the Middle Miocene (~15 Ma) as a result of subduction of the Philippine Sea Plate beneath SW Japan for the first time due to opening of the Japan Sea back-arc basin [*Kimura et al*., 2005a; *Tamaki et al*., 1992]. The opening first formed rift systems in the back-arc basin starting ~27 Ma and then caused rapid clockwise rotation of SW Japan at ~15 Ma [*Torii et al*., 1986]. This tectonic event resulted in alignment of the basement terranes and the Ryoke to San-In Zone granitoids parallel to the present-day Nankai Trough [*Kimura et al*., 2005a] (see Figures 1a and 1b).

The Shikoku Basin formed during 27–15 Ma as a back-arc basin behind the IBM arc on the northeastern margin of the Philippine Sea Plate. The Shikoku Basin spreading ridge was probably orthogonal to the SW Japan arc just prior to subduction reinitiation. The full width of the young Shikoku Basin seafloor (0–12 Myr old at the time of subduction reinitiation) subducted beneath SW Japan arc after ~15 Ma [*Kimura et al*., 2005a; *Okino et al*., 1994; *Seno and Maruyama*, 1984]. The paleogeography just prior to the subduction is uncertain. *Kimura et al*. [2005a] suggested that the spreading ridge of the Shikoku Basin was in front of the central SW Japan arc and the IBM arc was in front of central Japan. In contrast, *Mahoney et al*. [2011] proposed that the IBM arc was in front of central SW Japan at that time.

Subduction of the young Shikoku Basin induced subduction-related volcanism parallel to the present-day Nankai Trough in the fore and intraarc regions for over 1500 km [*Kimura et al*., 2005a, 2003b; *Tatsumi and Hanyu*, 2003] (Figure 1b). The earlier back-arc rift volcanism was gradually replaced by arc volcanism [*Kimura et al*., 2005a]. Setouchi HMA activity occurred almost simultaneously with subduction reinitiation at ~13 Ma about 250 km from the plate boundary [*Tatsumi et al*., 2008b] (Figures 1a and 1b). Felsic magmatism occurred even closer to the trench at 15–13 Ma. These are thought to be crustal melts formed by the heat from HMA and enriched (E-) MORB-type basalts from the Shikoku Basin spreading ridge [*Kimura et al*., 2005a; *Shinjoe*, 1997].

Subsequently, both OIB and AB erupted in the San-Yo and the San-In Zones during 9–5 Ma [*Kimura et al*., 2005a, 2003b] (Figure 1b) [see details in *Kimura et al*., 2005a, Figures 2 and 3], while OIB tholeiite to alkali basalts remained active in the Japan Sea [*Kimura et al*., 2005a; *Yamada et al*., 2013]. Magmatism changed from OIB to AB in the Pliocene [*Kimura et al*., 2005a], ADK appeared at Wakurayama in Matsue at ~5.0 Ma [*Sato et al*., 2011], and HMA (Chausuyama on the NW slope of Daisen, not shown in Figure 1) and SAB (Daisen) also erupted at that time [*Kimura et al*., 2003b] (Figure 3). The progressive increase of arc-type magmatism continued into the Quaternary after ~3 Ma, as discussed in the following section (Figure 3).

3.3. Tectonic Setting and Volcanic Activity in the Quaternary

The present-day tectonic setting of the SW Japan arc is summarized as follows. The Shikoku Basin (27–15 Myr old) is subducting northwestward at ~4 cm/yr at an oblique angle to the Nankai Trough trench axis

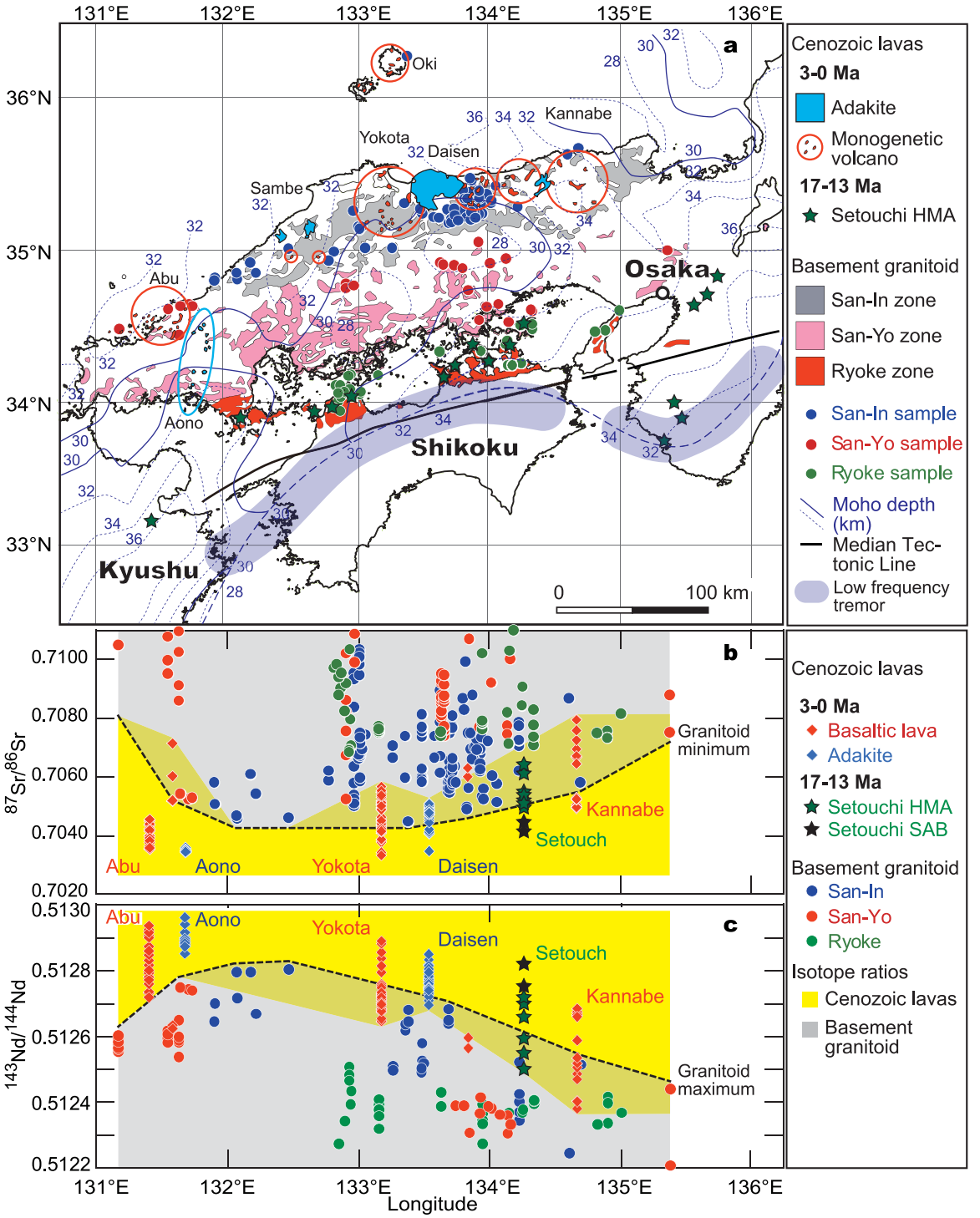

Figure 2. (a) Spatial distribution and (b) Sr and Nd isotope composition of basement granitoids in comparison to the late Cenozoic lavas. Basement granitoid zones (San-In, San-Yo, and Ryoke zones) from *Kagami et al.* [1992]. The San-In zone granitoids have more radiogenic Nd and unradiogenic Sr in comparison to those in the San-Yo and Ryoke zone granitoids when compared at the same longitude. The Quaternary lavas have less radiogenic Sr and more radiogenic Nd than in the basement granitoids. References for isotope data for the basement granitoids and Cenozoic lavas are listed in the text. Crustal thickness in km is from *Katsumata* [2010]. The range in isotope ratios in Figures 2b and 2c show the variability at the locations shown in Figure 2a.

(Figure 1a). The extinct spreading ridge of the Shikoku Basin is currently located offshore between Shikoku and the Kii Peninsula (Figure 1a) [*Nakajima and Hasegawa*, 2007]. The subducted slab is in contact with the arc crust beneath Shikoku and the Kii Peninsula to a depth of ~30 km (Figure 2a) [*Katsumata*, 2010]. Low-frequency tremor occurs near the triple junction of the crust-slab-mantle (Figure 1b) [*Obara*, 2002]. The

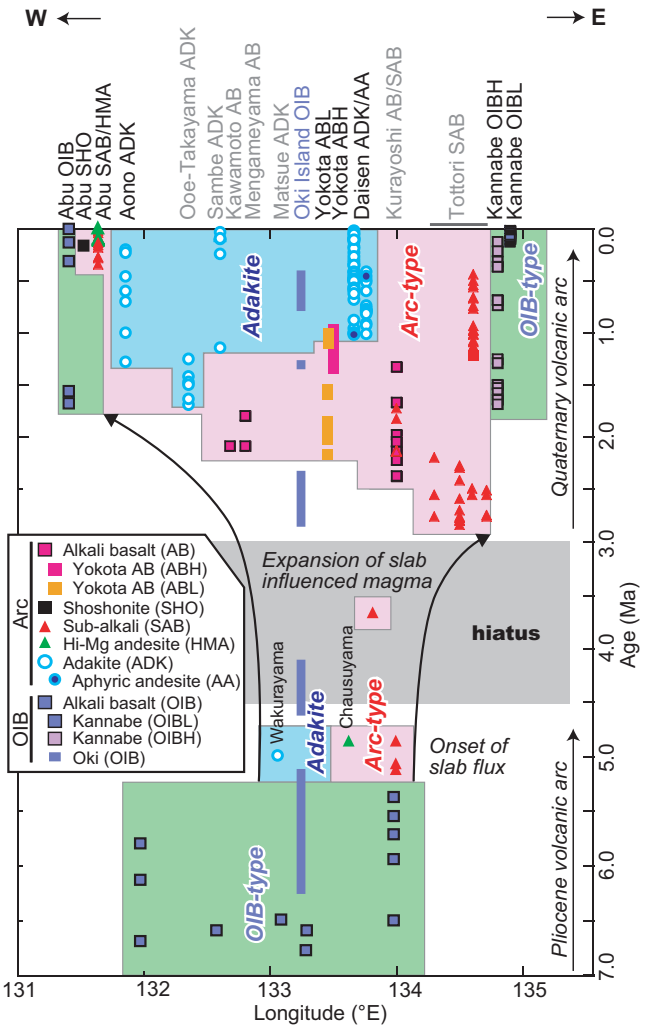

Figure 3. Along-arc temporal and spatial variation of magma activity in the SW Japan arc. For the definition of rock types, see sections 3 and 6. Ocean island basalt (OIB, in green) was dominant before 5.3 Ma and continues to the present at Abu (west) and Kannabe (east), and on Oki Island in the Japan Sea. OIB distribution correlates spatially with the slab tear areas imaged by mantle tomography [*Zhao et al*., 2012] (see Figure 1). Arc-type alkalic basalt (AB) subalkalic basalt (SAB) (in red), and adakite (ADK) (in blue) started at 5.3 Ma and are dominant between the recent areas of OIB. After adakite started between Aono and Daisen at 1–2 Ma, basalt eruptions stopped. Radiometric ages are from *Kimura et al*. [2003b].

subducted Shikoku Basin continues at a shallow angle (<30°) and slab seismicity terminates at ~60 km depth (Figure 1b) [*Nakajima and Hasegawa*, 2007]. Further extension of the slab was imaged by seismic tomography [*Zhao et al*., 2012] to as deep as 370 km behind the SW Japan arc beneath the Japan Sea (Figure 1b). The slab is inferred to be about 100–120 km beneath the volcanic front by projecting between the active seismicity and tomographic mages (Figure 1b) [*Zhao et al*., 2012]. No slab image is detected beneath Kannabe-Oki Island or the Abu-Tsushima Island areas, suggesting a slab tear or window in this area (D. Zhao, personal communication 2012). Crustal thickness beneath the Quaternary arc, as determined by receiver function analysis, is 30–34 km (Figure 2a) [*Katsumata*, 2010].

After a hiatus from ~5 to ~3 Ma, the Quaternary volcanic arc emerged along the Japan Sea coast forming the present-day volcanic front (Figures 1 and 3). From east to west, the arc consists of the following centers. OIB occurs at Kannabe (1.5–0.005 Ma) and mostly consists of OIBH, with subordinate OIBL most recently (0.015–0.005 Ma) [*Furuyama et al*., 1993a, 1993b; *Kimura et al*., 2005a] (Figure 3). AB occurs at Yokota (2.3–1.0 Ma) with eruption of ABL at 2.3–1.1 Ma, and ABH more recently (1.4–1.0 Ma) [*Kimura et al*., 2003b] (Figure 3). ADK erupted almost continuously at Daisen from 1.0 to 0.017 Ma, and AA occurred twice at ~1.0 and ~0.5 Ma [*Kimura et al*., 2003b] (Figure 3). ADK was also active at Aono from 1.3 to 0.2 Ma [*Furuyama et al*., 2002]. The Abu Monogenetic Volcano Group (2.0–0.005 Ma) [*Kakubuchi et al*., 2000] showed complex activity. OIB erupted at ~1.8 Ma and after ~0.3 Ma, SAB erupted at ~0.4–0.2 Ma, SHO erupted at ~0.2 Ma, and HMA erupted at 0.2–0.005 Ma [*Kakubuchi et al*., 2000] (Figure 3). The geochemistry of Tottori SAB, Kurayoshi AB/SAB, Mengameyama AB, Kawamoto AB, and Sambe, Matsue, and Ooe-Takayama ADK are not discussed in this paper but their ages and spatial distributions are shown in Figure 3 as a summary from *Kimura et al*. [2005a, 2003b].

OIB continued to erupt in the Quaternary but only at the western (Abu) and eastern (Kannabe) tips of the arc. OIB also erupted on Oki Island in the Japan Sea at ~0.4 Ma (Figure 3) [*Kimura et al*., 2005a; *Yamauchi et al*., 2009]. These OIB centers are located above the slab tear windows (Figure 1b) [*Zhao et al*., 2012].

In contrast, all the arc-type centers (AB, SAB, SHO, HMA, and ADK/AA) currently overlie the subducting Shikoku Basin (Figures 1b). The overall temporal changes show that AB and SAB first replaced OIB in the central part of the arc at 3.0–1.7 Ma and were followed by ADK/AA after 1.7 Ma. AB is absent where ADK/AA occurs (e.g., Yokota AB versus Daisen ADK/AA, and Kawamoto/Mengameyama AB versus Ooe-Takayama/Sambe ADK in Figure 3).

4. Samples and Methods

We analyzed 324 lava samples from the Kannabe, Yokota, and Abu clusters for OIB, AB, SAB, SHO, and HMA, and from Daisen and Aono for ADK/AA. All samples were analyzed for major and trace elements by X-ray fluorescence spectrometry (XRF), and 129 samples were analyzed for additional trace elements by inductively coupled plasma mass spectrometry (ICP-MS). Selected samples were analyzed for Sr (129), Nd (123), Hf (63), and Pb (64) isotopes by thermal ionization mass spectrometry (TIMS) for Sr and Nd, and by multicollector ICP-MS (MC-ICP-MS) for Hf and Pb. Representative data are given in supporting information 1 and complete analyses including ages are given in supporting information 2.

4.1. Sample Petrography

OIB and AB lavas are olivine−clinopyroxene and olivine+clinopyroxene basalts, with occasional plagioclase phenocrysts in Kannabe OIB [*Furuyama et al*., 1993b], Yokota AB [*Fujibayashi et al*., 1989; *Nagao et al*., 1990; *Tamura et al*., 2000], and Abu AB [*Kakubuchi et al*., 2000]. The Yokota AB were called Daisen basalts by *Tamura et al*. [2000] but we use the original rock unit name [*Nagao et al*., 1990]. Most olivines are euhedral to skeletal in shape. Groundmass phlogopite occurs in some olivine basalt lavas from Yokota [*Fujibayashi et al*., 1989] and tiny mantle xenoliths occur in the Uenodai dike (supporting information 1) at Yokota. No hydrous minerals or mantle xenoliths were found in OIB at Kannabe [*Furuyama et al*., 1993a]. SHO (absarokite) with phlogopite and olivine phenocrysts occurs at Fusumayama (supporting information 1) at Abu [*Tatsumi and Koyaguchi*, 1989]. SAB basalts to andesites from Abu have pyroxene and plagioclase phenocrysts but no hydrous minerals. ADK from Daisen and high-silica ADK lavas from Aono have up to 30% plagioclase and hornblende phenocrysts with trace amounts of biotite, pyroxenes, and iron-titanium oxides [*Kakubuchi et al*., 2000; *Kimura et al*., 2005b; *Tamura et al*., 2003; *Tsukui et al*., 1985]. AA at Daisen and some low-silica ADK at Aono have $<$5% plagioclase and pyroxene phenocrysts with iron-titanium oxides $\pm$ hornblende in the groundmass [*Furuyama et al*., 2002; *Kimura et al*., 2005b; *Tamura et al*., 2003]. There is a clear difference in phenocryst abundance between AA and ADK at Daisen, but a gradation at Aono.

4.2. Analytical Methods

Lava samples were broken into 1–2 cm chips with an iron hammer and subsequently crushed in an iron pestle down to 3–4 mm size. The crushed chips were sonicated in deionized water and dried at 110°C for $>$12 h. The dried samples were pulverized in an agate mortar for 40 min. The sample powder was ignited at 1000°C for 2 h to measure loss on ignition and to oxidize the iron.

Glass disks were prepared using a Tokyo Kagaku NT-2000 high-frequency bead sampler and a 2:1 flux:sample ratio. The glass disks were analyzed using a Rigaku RIX-2000 XRF spectrometer [*Kimura and Yamada*, 1996].

For trace element analysis, exactly 0.1 g of the same powders was digested in acid for OIB, AB, SHO, SAB, and HMA samples [*Kimura et al*., 2001], and by alkali fusion after acid digestion for ADK and AA samples [*Roser et al*., 2000]. The alkali fusion ensured dissolution of zircon crystals in the felsic rocks. Sample solutions were diluted 50,000 times and analyzed using a Thermo ELEMENTAL VG PQ-3 ICP-MS with a standard addition technique [*Kimura et al*., 1995]. XRF and ICPMS results for Rb, Nb, and Y agree to within 10%. Only ICP-MS results are plotted on multielement plots, whereas XRF data are used when available for major element versus trace element binary plots in order to show greater data coverage.

About 0.1g of sample powder was digested in an open beaker for Sr-Nd-Hf isotope analysis. Conventional cation-exchange column methods were used for Sr and REE separation, followed by HIBA separation of Nd from other REE [*Iizumi et al*., 1999]. An additional two-column separation method was used for Hf purification [*Brichert-Toft et al*., 1997]. Pb samples were digested in HF and Pb was separated using a single anion column [*Kimura et al*., 2003a]. A Finnigan MAT262 TIMS was used for Sr and Nd isotope analyses [*Iizumi et al*., 1999]. During the analytical period, $^{87}Sr/^{86}Sr = 0.710250 \pm 0.000030$ for NIST SRM987, and

$^{143}Nd/^{144}Nd = 0.51187 \pm 0.000020$ for La Jolla. A Thermo ELEMENTAL Plasma 54 MC-ICP-MS was used for Pb and Hf isotope analyses [*Kimura et al.*, 2006, 2010]. A Tl spike was used for Pb isotope fractionation correction. Measured isotopic ratios by MC-ICP-MS were normalized to $^{176}Hf/^{177}Hf = 0.282160$ for JMC475 [*Stevenson and Patchett*, 1990], and to $^{206}Pb/^{204}Pb = 16.9416$, $^{207}Pb/^{204}Pb = 15.4998$, $^{208}Pb/^{204}Pb = 36.7249$ for NIST SRM981 [*Baker et al.*, 2004]. For details of the analytical methods, see the references. All the analytical data, including results for rock standard JA-2 which is a Setouchi HMA, are given in supporting information 2.

5. Results

Below we describe the major, trace, and isotopic compositions of each rock suite in the SW Japan arc. The data are grouped by suite in the tables, and each suite has a separate color in the figures. All OIBs are purple, all HMAs are green, all ADK and AA are blue. Western centers are squares; eastern are circles.

5.1. OIB (Kannabe and Abu)

5.1.1. Major Elements

OIB basalts have 1.5–3.3 wt. % TiO_2 which correlates negatively with MgO (not shown). In both respects, this differs from all other suites. SiO_2 contents range from 46 to 53 wt. % (Figure 4a) with total alkali contents of 2.9–7.1 wt. % so that OIB are classified as alkali basalt in a total alkali-silica (TAS) diagram (Figure 4b). K_2O contents vary from medium-K to high-K (Figure 4c). MgO is generally higher (4–10 wt. %) at Abu

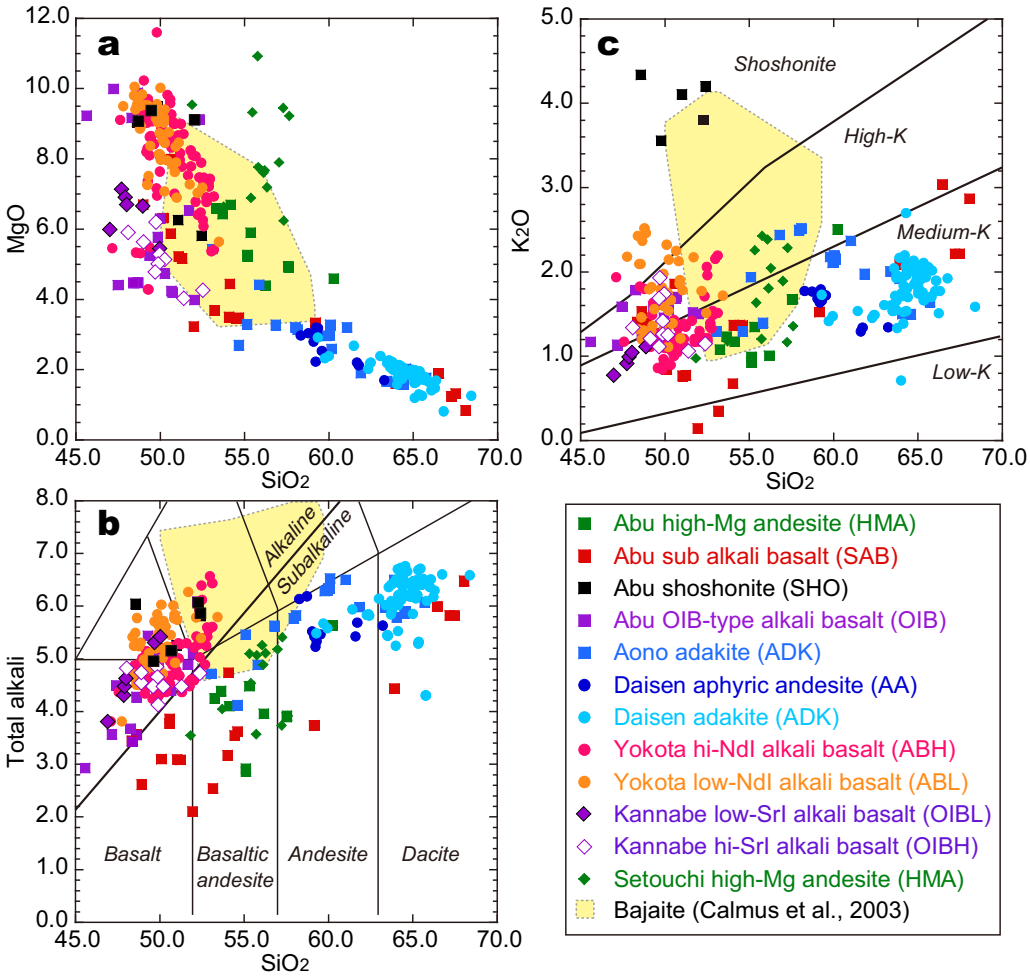

Figure 4. Major element compositions of lavas from the SW Japan arc organized by suites that are discussed throughout this paper. See sections 3 and 6 for the definitions of magma types. The same symbol is used for each suite throughout this paper.

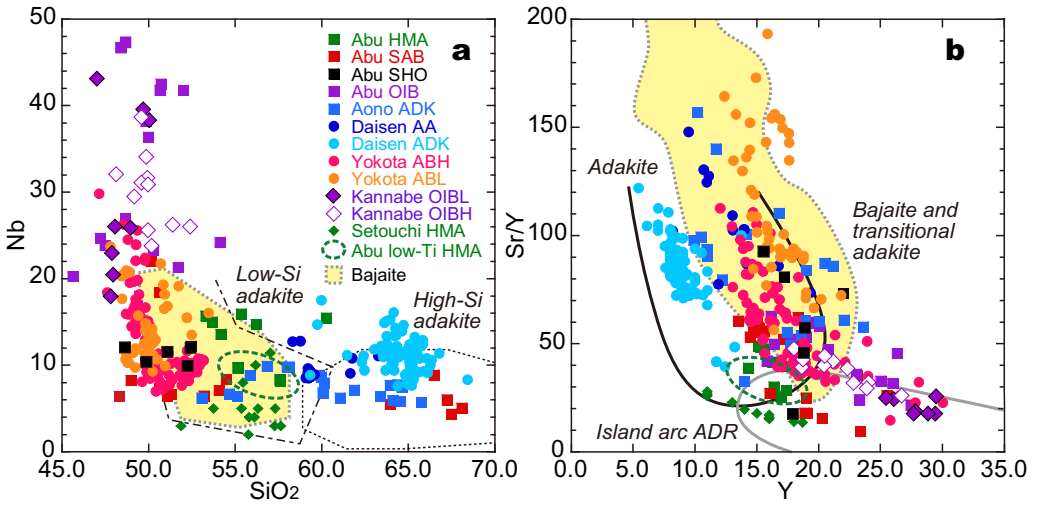

Figure 5. Diagrams for discriminating (a) between high-silica (High-Si) and low-silica (Low-Si) adakite [*Martin et al.*, 2005], and (b) between adakite (above dark line) and Andesite-Dacite-Rhyolite (ADR) (gray field) [*Defant and Drummond*, 1990]. The yellow Bajaite field in Figures 5a and 5b is from *Calmus et al.* [2003].

than Kannabe (4–7 wt. %) (Figure 4a). There are two OIB subtypes at Kannabe-OIBL and OIBH, based on Sr isotopic compositions (see section 5.1.3). However, there is no systematic difference between subtypes in major elements, including TiO_2.

5.1.2. Trace Elements

Nb contents are higher (18–48 ppm) in OIB than in all other suites (Figure 5a). OIB shows no negative troughs in Nb-Ta in a primitive mantle-normalized multielement plot (Figure 6) [*Sun and McDonough*, 1989]. Some Ce/Pb ratios are as high as in normal OIB and MORB (~27) but are usually lower and range down to 10. Consequently, OIB sometimes shows negative Pb troughs in multielement plots (Figure 6) rather than the nil or positive spikes in other suites. This feature is common in OIB worldwide [*Sun and McDonough*, 1989; *Willbold and Stracke*, 2006]. However, Ba and Sr are more enriched in SW Japan OIB than in oceanic OIB (Figures 5a and 5c) [*Sun and McDonough*, 1989; *Willbold and Stracke*, 2006]. This enrichment pattern is similar to that of Quaternary OIB in the even deeper rear arc of North China and is thought to originate from recycling Pacific Plate slab sediment [*Kuritani et al.*, 2011] or from enriched subcontinental mantle lithosphere [*Pouclet et al.*, 1995]. The trace element patterns are the same for OIBL and OIBH. OIB from Abu have more HREE depletion than from Kannabe (Figure 6a).

5.1.3. Isotopes

We distinguish two OIB subtypes on the basis of Sr isotopes. The OIBL subtype is the more common, occurring at both Kannabe and Abu. The OIBH subtype has higher Sr isotope ratios, lower (more enriched) Nd and Hf isotope ratios, and higher Pb isotope ratios (Figure 7). OIBH is also more enriched in trace elements (Figure 6).

The isotopic compositions of crustal granitoids are far more enriched than in OIBL and their compositional range overlaps OIBH in Sr-Nd (Figure 7a). Therefore, crustal assimilation is possible for OIBH. In order to test this, we plot all isotope compositions against SiO_2 (Figure 8). OIB does not show any correlations between isotope ratios and SiO_2, indicating no effect of crustal assimilation during fractionation.

5.2. Arc-Type Alkali-Basalt (AB) (Yokota)

5.2.1. Major Elements

AB are alkali basalts like OIB in a total alkali-silica (TAS) diagram (Figure 4b) but they lack the high Ti and Nb contents of OIB. That is, they are arc-type alkali basalts. They are the most common arc-type basalts in SW Japan. Most have higher MgO (up to 11.8 wt. %) than in OIB at a given SiO_2 (Figure 4a). There is no difference in major elements between the two isotopically different subtypes of AB discussed in section 5.2.3 (ABL versus ABH). K contents are mostly medium-K to high-K (Figure 4c), and a few ABL lavas plot in the shoshonite field.

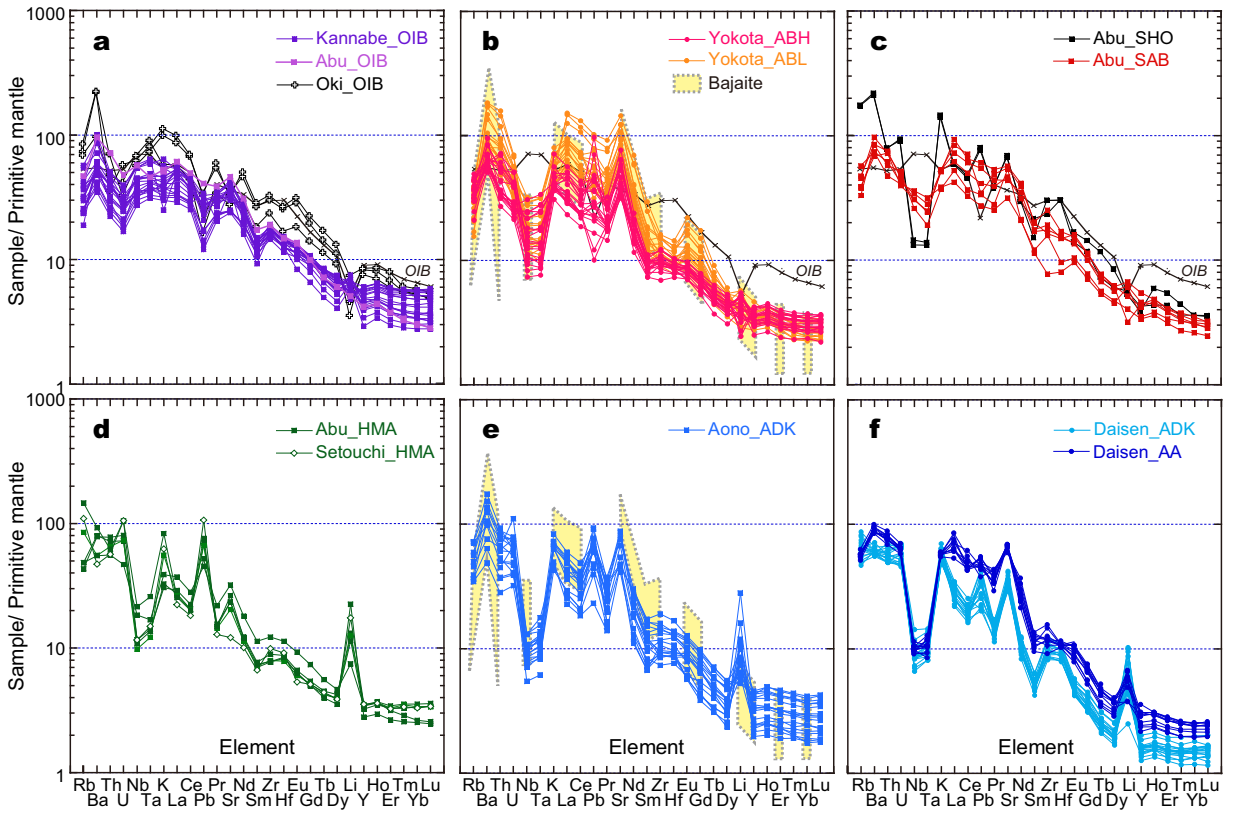

Figure 6. Multielement diagrams normalized to primitive mantle values of *Sun and McDonough* [1989]. Data are from supporting information 2. Data for global average OIB are from *Sun and McDonough* [1989]. Bajaite fields are from *Calmus et al.* [2003].

5.2.2. Trace Elements

Nb in AB is <25 ppm, lower than in OIB (Figure 5a). The compositional range of AB on Sr/Y-Y plots almost exactly overlaps the field of "bajaite," a silica-rich alkali basalt to high-Mg basaltic andesite occurring in Baja California [*Calmus et al.*, 2003] (Figure 5b). This is also true in major elements as shown by SiO_2-MgO, SiO_2-total alkalis, and SiO_2-K_2O plots (Figures 4a–4c). However, Yokota AB is poorer in silica and thus best classified as alkali basalt to distinguish them from HMA.

AB lavas are enriched in large ion lithophile elements (LILEs) and light rare earth elements (LREEs) relative to Nb-Ta and heavy(H) REEs (Figure 6a). Strong enrichments are shown in Ba, U, Th, LREEs, and especially Sr (2000–3000 ppm) [*Nagao et al.*, 1990]. Pb is also enriched, apart from a few samples with nil or even negative Pb anomalies (Figure 6b). Zr and Hf show nil (typically in ABH) to strongly positive (typically in ABL) anomalies. The latter are uncommon in arc basalts [*Pearce et al.*, 1999; *Tollstrup and Gill*, 2005] (Figure 6b). The incompatible trace element characteristics are comparable to those in bajaite [*Calmus et al.*, 2003] (Figure 6b). Some ABH have higher (Ba, Th, La)/Yb ratios than those in ABL (Figure 6b). They are from Uenodai where small mantle xenoliths occur [*Fujibayashi et al.*, 1989] (supporting informations 1 and 2). Other ABH lavas totally overlap ABL.

5.2.3. Isotopes

As with OIB, we distinguish two AB subtypes on the basis of Sr isotopes—lower in ABL, and more radiogenic in ABH (see Figures 7 and 8). They form separate arrays in Sr-Nd isotope plots (Figure 7a). Pb isotopes also are more radiogenic in ABH than in ABL but the two subtypes form a common linear array in all Pb isotope plots (Figures 7c and 7d). In contrast, their Nd-Hf isotopes almost overlap.

Although there are no strong differences in major and trace elements between ABL and ABH (Figures 6 and 7), we examine the subgroups separately in the following sections because of their systematic difference in Sr and Pb isotopes. The Uenodai AB is geochemically extreme and could not be modeled by the scheme used in this paper. We thus will not discuss it further.

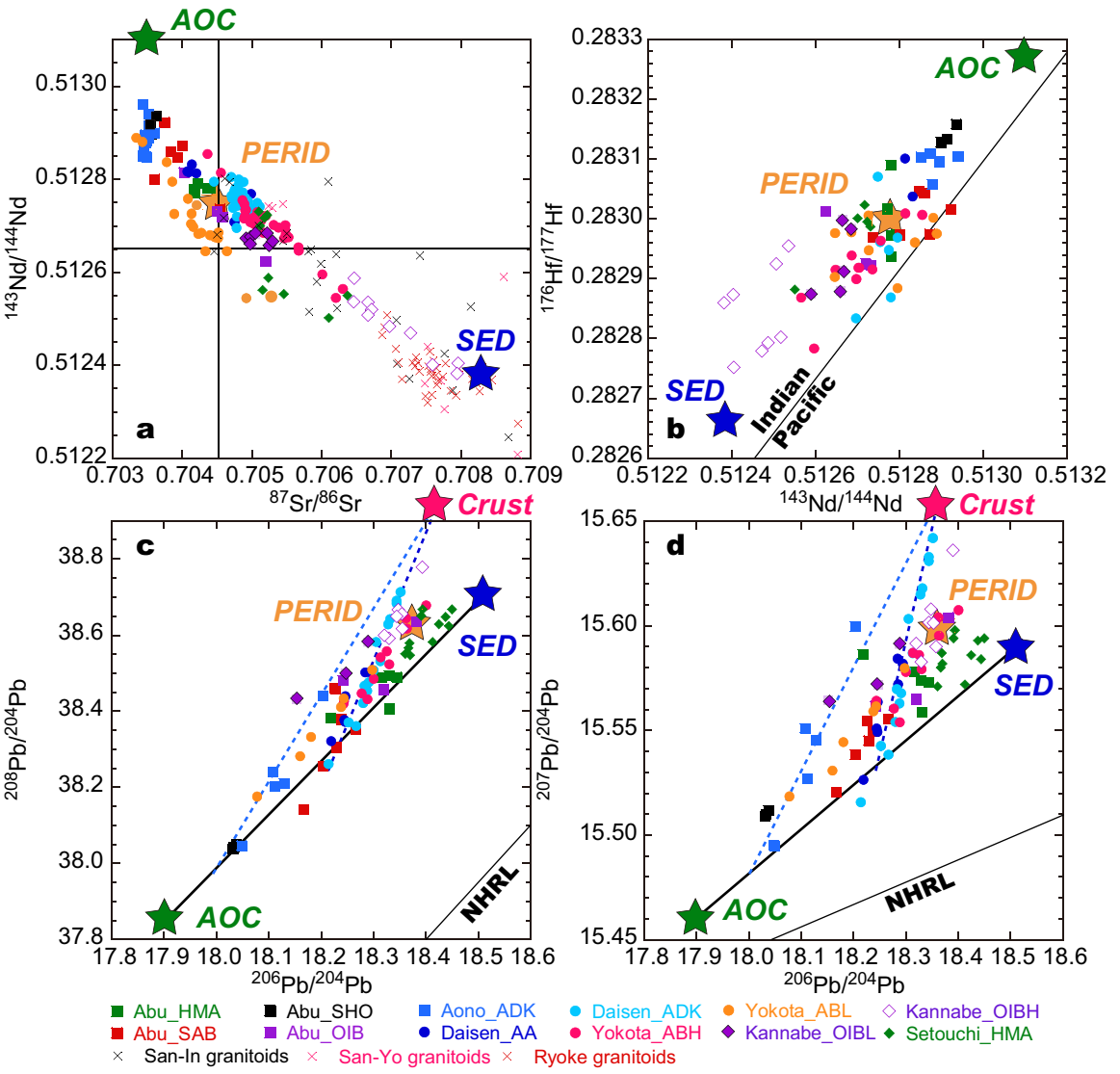

Figure 7. Sr-Nd-Hf-Pb isotope plots for lavas in the SW Japan arc. Compositions of sediment (SED) and altered oceanic crust (AOC) compositions from the Shikoku Basin, and the subarc mantle (PERID) are also shown. NHRL: The Northern Hemisphere Reference Line is from *Hart* [1984], and the Indian-Pacific mantle domain boundary is from *Pearce et al.* [1999]. For data source for the granitoids, see the text.

5.3. Shoshonite (SHO) (Abu)

5.3.1. Major Elements

SHO at Abu is absarokite [*Tatsumi and Koyaguchi*, 1989] with MgO as high as 9.5 wt. % at SiO_2 = 47–52 wt. %, and K_2O = 3.5–4.5 wt. % (Figures 4a–4c). The major element composition of SHO is also within the range of bajaite (Figures 4a–4c) [*Calmus et al.*, 2003].

5.3.2. Trace Elements

SHO has low Nb (<12 ppm) and high Sr/Y, within the range of bajaite [*Calmus et al.*, 2003] (Figures 5a and 5b). Abu SHO clearly possesses arc signatures with very strong Nb-Ta depletions, and enrichments of Rb, Ba, K, Pb, and Sr (Figures 6a and 6c). Zr-Hf shows strong positive enrichments that are, together with Daisen ADK, the most prominent among lavas in the SW Japan arc.

5.3.3. Isotopes

Abu SHO has a narrow range of Sr-Nd-Hf-Pb isotopes that are the most depleted among the examined magmas (Figure 7), matched only by the depleted end of Aono ADK (Figures 7a–7c). Abu and Aono are

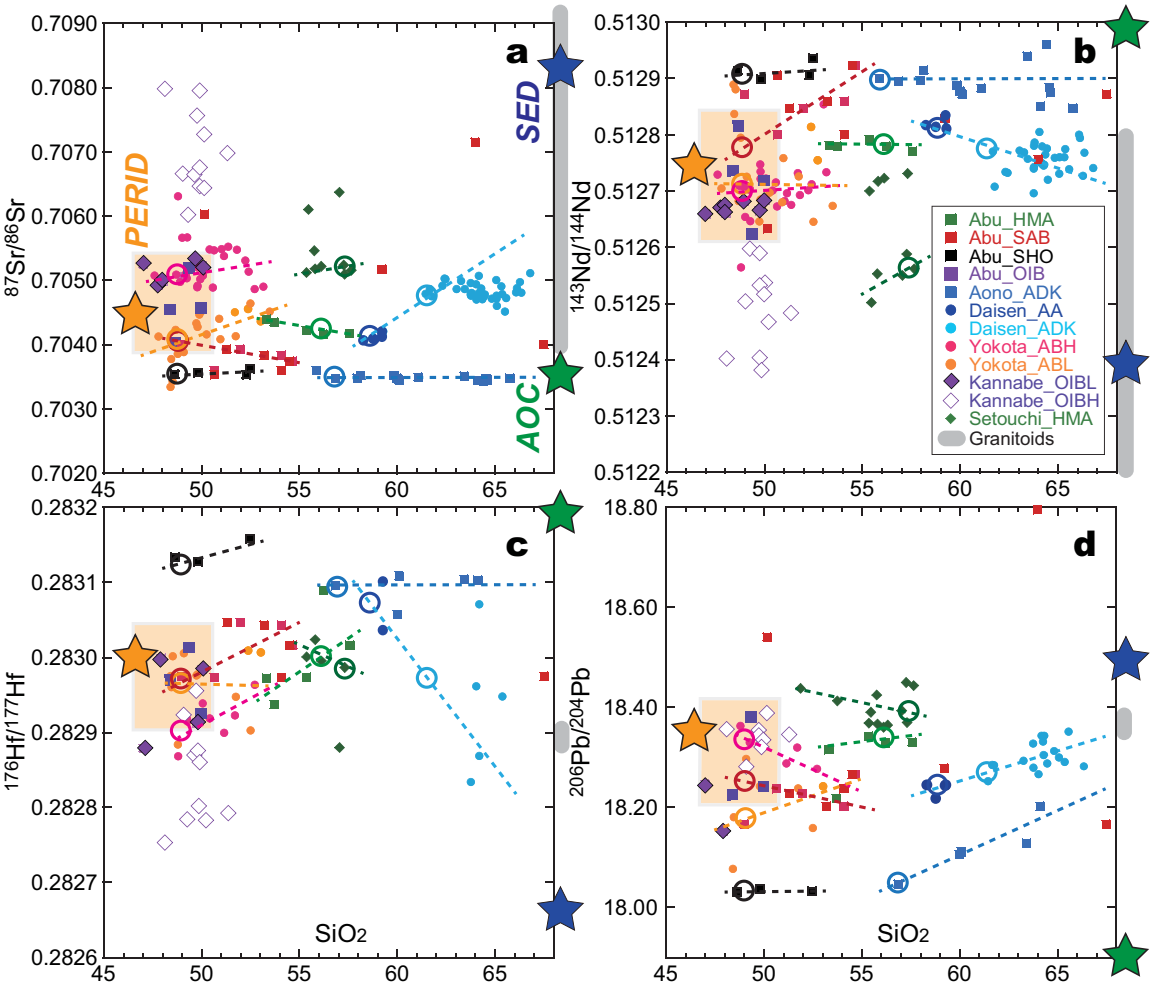

Figure 8. SiO_2 versus Sr-Nd-Hf-Pb isotope plots. Most of lavas have constant or random isotope compositions over the silica range indicating minimal crustal contamination. Aono ADK and Daisen AA/ADK show clear positive slopes for Pb isotopes, and Daisen shows negative slopes for Nd and Hf and a positive slope for Sr, indicating crustal assimilation during differentiation. Shade bars on the right of each plot show the isotopic composition of the basement granitoids. Large open circles are estimated primary magma compositions and dotted lines show possible mixing trends. The isotopic composition of the source peridotite (orange stars and boxes) is an average from the most common OIB type. AOC and SED are estimates for altered oceanic crust and sediment compositions. See details in the text.

relatively close to each other (Figure 1b) and their eruption ages overlap (~0.2 Ma; Figure 3), but their major and trace element geochemistry are totally different (Figures 4 and 6).

5.4. Subalkalic Arc Basalt (SAB) (Abu)

5.4.1. Major Elements

SAB basalts and differentiates have the most ordinary arc compositions but they are relatively uncommon in the SW Japan arc. They occur at Abu along with SHO and OIB (Figure 3) and at Tottori and Kurayoshi for which no new data are given in this paper. SAB basalts have lower total alkalis than in the other magma suites and form a linear array from basalt to dacite within the subalkaline TAS field (Figures 4a and 4c). TiO_2 is <1.5 wt. % (supporting information 2). K_2O contents also are lower than those in AB/OIB and are classified as medium-K (Figure 4c).

5.4.2. Trace Elements

SAB lavas have Nb-Ta troughs in multielement plots (Figure 5b) and their andesites to dacites have low Sr/Y ratios that lie in the nonadakite ordinary andesite-dacite-rhyolite (ADR) field of *Defant and Drummond* [1990] (Figure 5b). LILEs and REEs are somewhat similar to those in AB but there are weaker positive spikes in Sr and Pb in SAB (Figure 5a). SAB have nil to negative Zr-Hf troughs which is also different from AB.

5.4.3. Isotopes

SAB has Sr and Nd isotopes that are almost as depleted as in SHO and Aono ADK (Figure 7a), whereas Hf isotope ratios are distinctively lower (Figure 7b). In contrast, Pb isotope ratios show a wide variation extending from Abu OIB to less radiogenic values (Figures 7c and 7d). In addition, although Sr and Nd isotopic compositions are confined to a narrow range for most SAB basalts, one basalt and two andesite-dacites have extremely radiogenic Sr and Pb (Figure 8). These samples are strongly contaminated by crustal materials and are not discussed further.

5.5. High-Magnesium Andesite (HMA) (Abu and Setouchi)

5.5.1. Major Elements

We will first discuss the HMA in the Quaternary SW Japan arc at the Nagasawadai, Nabeyama, and Kasayama centers in the Abu Monogenetic Volcano Group, and then compare them to the well-known Setouchi HMA [*Tatsumi*, 2006] (Figure 1 and supporting information 2). The major element compositions of Abu HMA, including SiO_2, MgO, K_2O, and total alkalis, are within the field of Setouchi HMA (Figure 4a) [*Tatsumi and Hanyu*, 2003] (see locations in Figure 3). The bajaite field overlaps for some elements but total alkalis are distinctively lower for Setouchi and Abu HMA. That is why we classify the Abu andesites as HMA. Both the Abu and Setouchi HMA are geochemically more similar to high-Mg andesite from the Aleutians [*Yogodzinski et al*., 1995, 2001] than to boninite [*Ishizuka et al*., 2006; *Li et al*., 2013].

Abu HMA has MgO = 4–7 wt. % at SiO_2 = 53–60 wt. % which is not as high as the 6–11 wt. % of Setouchi HMA (Figure 4a). However, the MgO range of Abu HMA is clearly higher than that in Abu SAB (Figure 3a). TiO_2 is low in Setouchi HMA (0.4–0.7 wt. %) [*Tatsumi and Hanyu*, 2003], whereas TiO_2 is bimodal in Abu HMA: lower (0.7–0.8 wt. %) at Nagasawadai and Nabeyama, and higher (1.5–1.6 wt. %) at Kasayama (supporting information 2). The low-Ti HMA also have lower Fe, Ca, and Na, but higher Al, and are more like Setouchi (supporting information 2).

5.5.2. Trace Elements

The trace element composition of low-Ti Abu HMA is almost identical to Setouchi HMA with low Cr, Nb, Sr/Y, and LREEs, and high Pb and U (supporting information 2; Figures 5a, 5b, and 6d). The only differences are higher Sr and lower Rb in Abu HMA (Figure 6d). The overall similarities indicate that Abu HMA is the Quaternary equivalent of the Miocene Setouchi HMA.

Abu HMA has quite different incompatible element patterns from coexisting SAB (Figure 6d) with deeper Nb-Ta troughs and more depleted LREE. K, Pb, Sr, and Li are strongly enriched relative to REE. Zr-Hf is slightly enriched in HMA in contrast to SAB (Figure 6d). These geochemical features also differ from the other SW Japan suites including AB and SHO (Figure 6).

5.5.3. Isotopes

There are no differences in isotopic compositions between low-Ti and high-Ti Abu HMA and they have a narrow compositional range in all isotopes (Figures 7 and 8). Abu HMA is more depleted than Setouchi HMA for all isotopes and is slightly more enriched than Abu SAB (Figure 7).

5.6. Adakite (ADK/AA) (Aono and Daisen)

5.6.1. Major Elements

Daisen adakites include a more abundant porphyritic variety usually with >63% SiO_2 (ADK) and a less common aphyric variety (AA) with <5% phenocrysts and lower SiO_2 [*Kimura et al*., 2003b; *Tamura et al*., 2003]. The two groups have similar compositions despite different texture. In contrast, Aono adakites range in SiO_2 from 54 to 65 wt. % and have a more gradational range from less phyric lower-SiO_2 to mostly porphyritic higher-SiO_2 lavas. The Aono adakites have higher K_2O but are otherwise similar in major element composition to Daisen ADK (Figure 4). The major element compositions of all ADK and AA are within the definition of adakite by *Defant and Drummond* [1990] and *Morris* [1995]. The two ADK centers are separated spatially by about 200 km (Figure 1b) but erupted quite similar lavas at about the same time (Figure 3).

5.6.2. Trace Elements

All ADK/AA lavas have Nb < 18 ppm (Figure 5a). The higher-Si samples lie within the adakite field on the Sr/Y-Y (Figure 5b) and La/Yb-Yb (not shown) discrimination diagrams of *Defant and Drummond* [1990], whereas some lower-Si aphyric samples have higher Y. The higher-Si adakite overlaps the silicic bajaite field of *Calmus et al*. [2003].

Aono ADK has a wide compositional range in incompatible trace elements with subparallel patterns in a multielement diagram (Figure 6e) but most elements do not correlate with SiO_2 (see, for example, the scatter in the SiO_2 versus K_2O plot; Figure 4b). In contrast, Daisen AA and ADK each has a narrow compositional range that is distinct from the other and from Aono's. Daisen AA is more enriched in most incompatible trace elements than ADK despite having lower SiO_2 (Figure 6f). Aono has a positive Ba spike and lower Th/U. Daisen ADK has a positive Zr-Hf spike that is smaller at Aono and almost nil in Daisen AA (Figures 6e and 6f). All ADK/AA are depleted in Nb-Ta and highly enriched in LREEs with prominent positive K, Pb, Sr, and Li spikes (Figures 6e and 6f).

5.6.3. Isotopes

Aono ADK has depleted Sr-Nd isotopes and a vertical trend indicating binary mixing (Figure 7a). Daisen ADK and two Daisen AA are more enriched and overlap the depleted end of the Setouchi HMA field (Figure 7a). Nd isotopic compositions of Daisen ADK widely vary for their narrow Sr isotopic compositions, forming a vertical array similar to Aono ADK (Figure 7a). Hf isotopic compositions show the same depletion-enrichment relationship as Nd between Aono ADK, Daisen AA/ADK, and Setouchi HMA (Figure 7b).

Pb isotopes in Daisen AA/ADK and Aono ADK define steep, linear, and separate binary mixing arrays from the lower bound of the SW Japan compositional field toward an extremely radiogenic composition (Figures 7c and 7d). Daisen AA overlaps the less radiogenic half of the Daisen ADK array (Figures 7c and 7d). The Daisen and Aono arrays appear to converge at the radiogenic end at $^{206}Pb/^{204}Pb \sim 18.4$. In both groups, Pb becomes more radiogenic with increasing SiO_2 (Figure 8d). This feature is not prominent in any other isotopic or trace element ratio.

6. Discussion

The felsic ADK/AA, andesitic HMA, and basaltic OIB/SHOSAB/AB in the Quaternary SW Japan collectively form a quite distinctive magma association including high-Nb basalt [*Defant and Drummond*, 1990; *Kay*, 1980] (OIB/SAB), bajaite [*Calmus et al*., 2003] (AB/HMA) [*Yogodzinski et al*., 1995], HMA, and adakite [*Defant and Drummond*, 1990] (ADK/AA). Some of these coexist elsewhere but SW Japan is the only place where they all occur together.

All of these rock suites are associated with hot subduction zones involving subduction of an actively spreading ridge (Central Mexican Volcanic Field) [*Defant and Drummond*, 1990], or a young oceanic plate (Cascadia and Baja California) [*Calmus et al*., 2003; *Defant and Drummond*, 1990], or a slab tear (West Aleutians to Kamchatka [*Yogodzinski et al*., 2001], Panama [*Gazel et al*., 2011]). The SW Japan arc involves the last two [*Kimura et al*., 2005a; *Zhao et al*., 2012].

Because of this association with hot subduction, slab melting has been invoked to explain the origin of most of these rock suites, particularly HMA and ADK [*Kimura et al*., 2005a, 2005b; *Morris*, 1995; *Tatsumi and Hanyu*, 2003]. However, there are alternative explanations such as remelting the young crustal roots of a volcano [*Tamura et al*., 2003], deep fractionation of hydrous basalt magma [*Macpherson et al*., 2006; *Zellmer et al*., 2012], or remelting lower crust in the garnet amphibolite facies [*Castillo*, 2006; *Moyen*, 2009]. Therefore, thorough examination of the genetic models is necessary. In the following sections, we will discuss the genetic relationships among all the lava suites using our comprehensive geochemical data set. OIB shows large isotopic variations with no arc signatures. We use these variations to define the characteristics of the local mantle unaffected by subduction components. Because our focus in this paper is the genesis of the arc-type magma suites, we leave discussion of the origin of OIB to another paper.

We will first discuss crustal assimilation, fractional crystallization, and primary magma compositions for each magma suite. We then estimate the source mantle and slab compositions, and finally discuss slab-mantle processes operating beneath the SW Japan arc. We propose a quantitative interpretation using our revised petrological/geochemical forward model: the Arc Basalt Simulator version 4 (ABS4).

6.1. Crustal Assimilation

We first examine the bulk rock and hornblende mineral chemistry of ADK because AA/ADK show the clearest evidence of crustal assimilation (see above section 5.6). We estimate the crustal melt composition and then evaluate its presence in the other magma suites (HMA/OIB/AB/SHO/SAB).

6.1.1. Crustal Assimilation in Daisen ADK

Daisen ADK/AA have been interpreted previously as products of mixing between melts of preexisting solidified andesite and differentiates of mantle-derived basalt [*Tamura et al*., 2003]. Daisen AA was regarded as the heat source for crustal remelting and as the differentiate of mantle-derived basalt [*Tamura et al*., 2003]. This hypothesis can be tested using Yokota ABL/ABH as the parental basalt because AB shares many trace element features in common with ADK, the two volcanoes are located near each other (Figure 1b), and they erupted at about the same time (Figure 3). However, Daisen AA cannot be a differentiate of Yokota ABL or ABH because Nd-Hf isotope ratios of AA are higher than those in ABL/ABH (Figure 8).

The Pb isotopes in Daisen AA/ADK form a mixing array in which the radiogenic end-member has higher SiO_2 and is similar isotopically to local San-In granitoids (Figures 7c, 7d, and 8d). The same is also true for Sr-Nd-Hf isotopes. This indicates that the felsic component in Daisen ADK is from the older basement rather than from a contemporaneous adakitic pluton that differentiated from mantle basalt, and it is also evidence against subcrustal differentiation.

Crustal assimilation in Daisen ADK is supported by detailed study of its characteristic hornblende phenocrysts. A typical example was analyzed by EPMA and LA-ICP-MS and the results are presented in supporting information 3 and Figure 9. Our analytical methods for EPMA and LA-ICP-MS have been reported elsewhere [*Tatsumi et al*., 2008b]. The crystal has a Mg-rich core [Mg# = Mg/(ΣFe+Mg) (molar ratio) = 0.76–0.60] mantled by a thick Mg-poor rim (Figure 9b). That is, the hornblende also is normally zoned. The Al_2O_3 content is also higher in the core than rim (Figures 9a and 10c). The core is irregular in shape although the overall crystal is almost euhedral, indicating resorption of the core and later overgrowth of the rim (Figure 9a). The trace element composition of the hornblende varies widely, from cores poor in REE, Th, and U, to rims with higher concentrations. Sr is the opposite, resulting in a high Sr/Y ratio in the core (40) and low in the rim ($<$5) (Figure 9a).

In order to examine the composition of the melt from which the hornblende core and rim crystallized, we calculated melt compositions using the average hornblende partition coefficients of *Pilet et al*. [2011]. In order to obtain fine adjustments, we modified partition coefficients for several elements (see Figure 9e, D(Hb)) that are within the range of the compiled values [*Pilet et al*., 2011]. The resulting melt compositions are shown in Figure 9f. The melt composition that crystallized the Mg-rich core closely approximates the ADK bulk rock composition. In contrast, the Mg-poor rim crystallized from a very different melt with elevated U, Th, and HREE, and depleted Sr (Figure 9f).

This surprised us because the rim is almost euhedral in shape yet it is not in equilibrium with the bulk magma. However, it is highly oxidized, not completely euhedral, and has some embayments (Figure 9a). Our interpretation is that the core crystallized from ADK and later mixed with a more felsic melt, resulting first in a resorption boundary, and then in growth of the rim. Finally, it became oxidized and partially decomposed during decompression and eruption. The hornblende crystal clearly shows that both low Mg + Sr melts and high Mg + Sr melts were present beneath Daisen. Most of the mass of the system is like the high Mg + Sr melt. The Sr-poor melt had high Th, U, and REE contents and could be formed by melting pelitic or granitic basement rocks.

Based on the correlations between bulk rock SiO_2 and isotope ratios (Figure 8) and the hornblende data (Figure 9), we conclude that the porphyritic Daisen adakites (ADK) include a mixing component derived from crustal assimilation. This component was a felsic melt characterized by high Si, Na, REE, Th, and U, but low Mg and Sr, and radiogenic Pb and Sr. It mixed with a more mafic component that had a typical adakitic signature that we interpret as being subcrustal in origin. The least phyric samples (AA) are the least contaminated isotopically (Figure 8). Crustal assimilation diluted rather than caused the adakitic signature. Internal mixing as proposed by *Tamura et al*. [2003] is not supported by our data.

6.1.2. Crustal Assimilation in Aono ADK

Aono ADK has a similar Pb-isotope mixing array (Figure 8d). Crystal poor low-silica samples and more porphyritic silica-rich ADK at Aono share similar petrographic features as in Daisen AA/ADK. However, in contrast to the Pb isotopes, Sr-Nd-Hf isotope compositions at Aono are almost identical over a wide silica range (Figures 8a–8c). Many incompatible trace element ratios including Ce/Pb, (La,Th,Nb)/Yb, La/Nb, and Ba/Th also are quite uniform at Aono but variable due to mixing at Daisen (not shown but see supporting information 2). Thus, the crustal assimilation indicated by Pb isotopes for Aono adakites had much less effect on

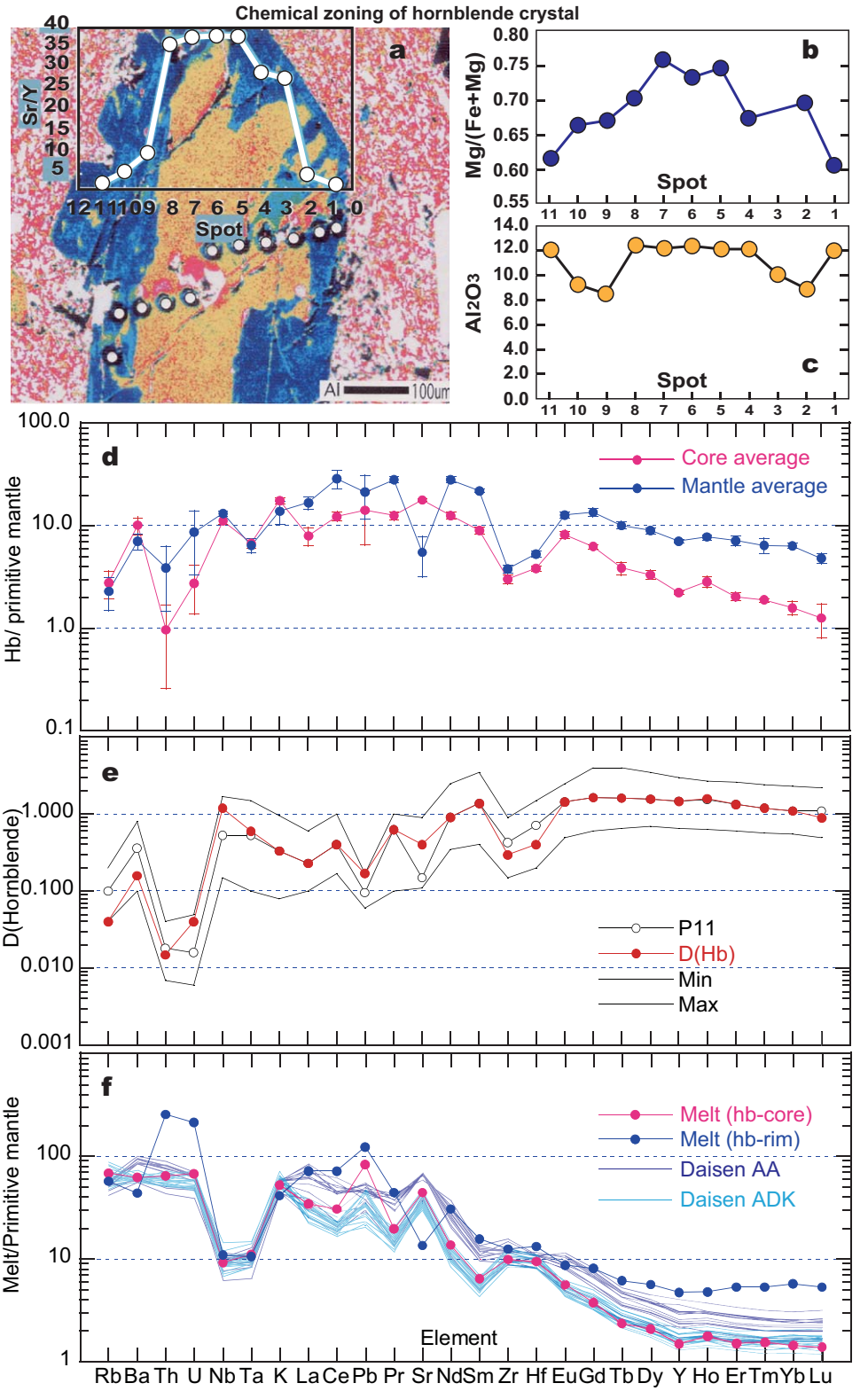

Figure 9. Chemical zoning of a hornblende crystal in Daisen ADK lava. The colors in Figure 9a show Al contents. (a–d) Sr/Y, Mg#, and Al_2O_3 are all higher in the core than in the thick overgrowth rim. Multielement plots are normalized to the primitive mantle of *Sun and McDonough* [1989]. Estimated melt compositions in Figure 9f use the partition coefficients shown by red dots in Figure 9e. They are the same as the P11 coefficients in *Pilet et al.* [2011] except for a few elements, shown by open black circles, for which we adopted slightly different values that lie between the minimum and maximum range of measured hornblende partition coefficients that are shown by Min and Max, respectively [*LaTourrette et al.*, 1995; *Tiepolo et al.*, 2007, 2000a, 2000b; *Rollinson*, 1993]. The calculated composition of melt from which the hornblende core crystallized is adakitic.

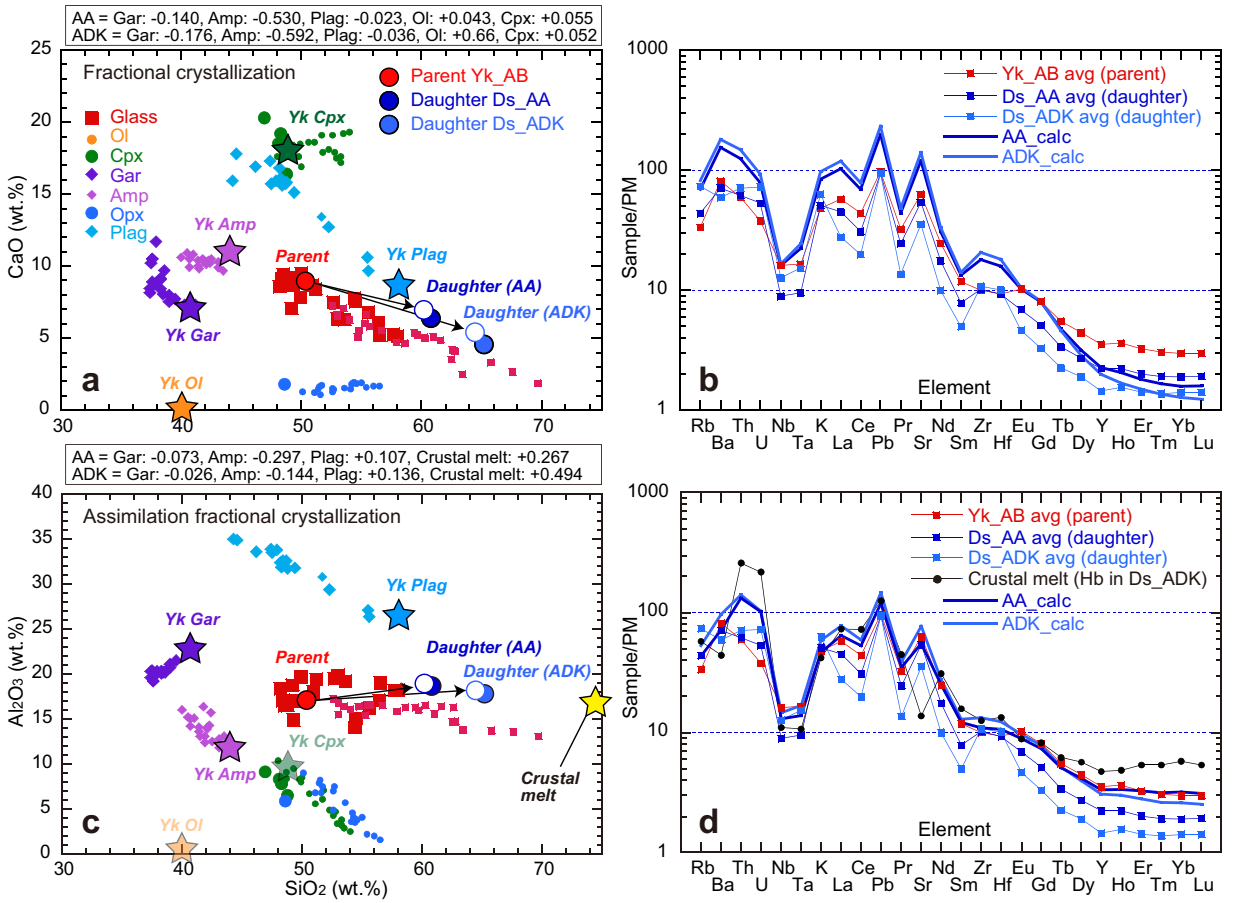

Figure 10. Model calculation results of high-pressure fractional crystallization (FC) and assimilation fractional crystallization (AFC) including garnet. The assumed parent basalt is assumed to be the average of Yokota Basalts. Daughters are from averages of Daisen aphyric andesite (AA) and Daisen (ADK) adakite lavas. Mineral compositions are measured values for plagioclase and amphibole crystals in Daisen adakite and olivine crystals from Yokota Basalt, whereas those for garnet and clinopyroxene are from experiments by *Müntener et al.* [2001] and *Alonso-Perez et al.* [2009] at ~1 GPa for basalt and andesite, respectively. Experimental mineral and glass data are also shown with large and small symbols for the basalt and andesite, respectively. (a and c) Examples of major element mass balances for FC and AFC, respectively. The crustal melt composition used for AFC is calculated using the amphibole rim composition in a Daisen ADK lava (Figure 9). Calculated results by least square mass balance are also shown in squares; details are given in supporting information 4. Using the FC and AFC major element mass balance, trace element compositions are calculated based on the partition coefficients given in supporting information 4. Although fractional crystallization can produce similar spikes and troughs as in the Daisen adakites, it underpredicts the observed high concentration of elements more incompatible than Y, and does not explain the differences in trace element ratios between Yokota AB and Daisen ADK. AFC results in a better fit for many of the more incompatible elements, but a worse fit for the critical HREE.

other elements than at Daisen. Alternatively, the San-Yo granitoids beneath Aono (Figure 2a) could be similar isotopically to the Aono adakites (e.g., Nd isotope shown in Figure 2c) in contrast to the larger contrast between the San-In granitoids and Daisen adakites.

6.1.3. Crustal Melt Origin of Low-Silica AA/ADK?

We have shown that a common felsic crustal melt with radiogenic Pb is present in both adakite centers even though they are more than 200 km apart (Figure 1b). Although we attribute the unradiogenic end of the Pb isotopic mixing arrays in Figures 7 and 8 to subcrustal processes, others have argued that adakite originates in the lower crust [e.g., *Moyen*, 2009]. The maximum thickness of the crust beneath SW Japan is ~35 km [*Katsumata*, 2010] (Figure 2) which means that garnet would be a residual mineral during lower crustal melting [*Alonso-Perez et al.*, 2009; *Beard and Lofgren*, 1991; *Johannes and Holtz*, 1996; *Müntener et al.*, 2001] and could be responsible for the adakitic characteristics of the melt.

However, the isotopic composition of the basement granitoids rules out this possibility (Figure 2). Although the Sr and Nd isotope ratios of basement granitoids, AA, and low-silica ADK overlap, the isotopically depleted and more adakitic mixing components are more depleted than the basement granitoids (Figures 2b and 2c) and, therefore, cannot be derived from them. Consequently, we will seek to explain the depleted, more adakitic end-member by subcrustal processes.

6.1.4. Crustal Assimilation in HMA, OIB, AB, SHO, and SAB

HMA has a narrow range of Nd, Hf, and Pb isotope compositions that do not vary with SiO_2 (Figure 8). The exception is Sr for which there is a negative correlation with SiO_2. Setouchi HMA has more radiogenic Sr, less radiogenic Nd, and similar Hf and Pb isotope compositions than Abu HMA. However, the differences do not correlate with SiO_2 or other differentiation indices. Thus, there is not yet any firm evidence of crustal assimilation in HMA.

Kannabe OIB has a wide variation in Sr isotope composition that we refer to as OIBH (high) to OIBL. However, this variation does not correlate with SiO_2, MgO, or other differentiation indices (Figure 8). Apart from the most mafic sample (HG-25), this is also true for Abu OIBs that are similar isotopically to Kannabe OIBL. Therefore, we attribute the isotopic diversity of OIB to the mantle.

ABL and ABH at Yokota have different trends in SiO_2-isotope ratio plots (Figure 8). ABL shows an increase in Sr isotope ratio with increasing SiO_2 (Figure 8a) but other isotopes scatter widely (Figures 8b–8d). Similarly ABH has a positive correlation between Hf isotopes and SiO_2 but other isotopes scatter widely (Figure 8). Consequently, there is no clear evidence of crustal assimilation in either AB group.

SHO has almost constant isotopic compositions within a narrow SiO_2 range. Its positive correlation between Nd and Hf isotopes (Figure 7b) is unrelated to SiO_2 and seems to be, instead, from the mantle.

SAB has clear negative correlations between SiO_2 and Sr and Pb isotopes, and crude positive correlations with Nd and Hf isotopes (Figure 8). However, these trends do not point toward the crustal granitoids, precluding assimilation of such crust as the explanation for the correlations in SAB. The low-silica end of the isotopic trends of SAB falls within the Abu OIB field, whereas the high-silica end points toward low-Si Aono ADK for all isotopes except Pb (Figure 8). Earlier (section 6.1.2), we interpreted low-Si Aono ADK as largely free of crustal contamination, so we draw the same conclusion for SAB.

6.2. Primary Magma Compositions

Because our forward models involve comparison to primary magmas, the effects of fractional crystallization need to be examined. Deep fractionation of garnet has been suggested for ADK [*Zellmer et al*., 2012], and fractionation of olivine has been examined for Yokota AB [*Tamura et al*., 2000]. Therefore, in this section we will examine the effects of fractional crystallization and estimate primary magma compositions for all the magma suites. Fractionation corrected representative primary basalts are listed in supporting information 5 for OIB/SHO/AB/SAB and representative primary magma compositions are listed in supporting information 6 for all magma suites.

6.2.1. Fractional Crystallization and Primary AA/ADK

Having already shown that Daisen ADK is derived from AA by crustal assimilation (section 6.1.1), we now explore whether the AA is derived from primary basalt by deep fractionation of amphibole and garnet [*Macpherson et al*., 2006; *Zellmer et al*., 2012]. To test this, we again examine the relationship between Yokota AB and Daisen AA/ADK because Yokota AB are the most plausible mafic parents based on their trace element characteristics and their close association in space and time.

First, as we showed in section 6.1.1, the isotope geochemistry precludes closed system fractionation. Although the isotopic trends of Yokota ABH on SiO_2 versus Nd-Hf-Pb isotope plots appear to point to Daisen AA (Figures 8b–8d), $^{87}Sr/^{86}Sr$ does not (Figure 8a). The situation is worse for Yokota ABL; none of the isotopic trends for Yokota AB point to Daisen AA.

Second, we tested garnet fractionation even though no garnet is present. We assumed the average composition of ABL and ABH as the parents, and the average compositions of Daisen AA and ADK as the daughters, and performed mass balance calculations in order to examine the effect of fractional crystallization. Because we have shown the need for crustal assimilation in ADK, we also examined assimilation plus fractional crystallization (AFC) using the estimated trace element composition of crustal melt from hornblende rims (section 6.1.1). The calculation results are shown in supporting information 4 and Figure 10. For details of the mass balance calculations see Appendix A. The fractionation scheme that best explains the major element trends (e.g., Figures 10a and 10c) requires about 78% fractionation with amph:gar proportions ~4:1. However, this scheme results in a mismatch for most trace elements (e.g., see Figures 10b and 10d and Appendix A for details). Therefore, neither trace elements nor isotopes are consistent with the garnet-fractionation hypothesis.

Based on our discussion of crustal contamination in section 6.1, the adakites with the lowest silica and least radiogenic Pb should be the least contaminated and therefore the best estimate of parental magma. Such samples have a narrow compositional range for trace elements at Daisen AA/ADK but a wide range at Aono. Consequently, we used the average trace element concentrations and the most depleted isotopes to calculate the primary magma target composition for Aono ADK and Daisen AA and ADK (supporting information 6).

6.2.2. Fractional Crystallization and Primary HMA

Setouchi HMA has been rigorously studied with the conclusion that they are partial melts of the subducted Shikoku Basin that later equilibrated with overlying mantle wedge peridotite [*Shimoda et al*., 1998; *Tatsumi and Hanyu*, 2003]. The low-Ti Abu HMA are similar to Setouchi HMA in terms of major and trace element compositions (section 5.5). Their high Mg-Ni-Cr contents are clearly distinct from the other Quaternary magma suites. They may have equilibrated with the mantle and could be primary magmas [*Tatsumi and Hanyu*, 2003; *Tsuchiya et al*., 2005; *Yogodzinski et al*., 1995].

Because their narrow compositional range makes it difficult to constrain fractional crystallization processes, we use their average composition as the primary melt (supporting information 6). We used the reference standard JA-2 as the primary melt composition for Setouchi HMA because it is so comprehensively analyzed and is almost an average composition of Setouchi HMA (supporting information 6). For Abu we used the average isotopic and major and trace element composition as the primary magma. The major and trace element, and isotopic composition of primary Abu and Setouchi HMA that we will use for model calculations are given in supporting information 6.

6.2.3. Fractionation Crystallization and Primary OIB, SHO, AB, and SAB

Estimating a primary basalt composition is not easy because of uncertainties in both the fractionating mineral phases and the source mantle composition. It is particularly difficult for arc basalts that may be products of (1) hydrous peridotite melting [*Grove et al*., 2006; *Katz et al*., 2003], (2) open system flux melting of variably depleted peridotite, or (3) melting of pyroxenite [*Kelemen et al*., 1998; *Straub et al*., 2008, 2011], and (4) subsequent crystal fractionation with variable water contents at various depths [*Almeev et al*., 2013a, 2013b].

Because of the likelihood of flux melting, applying petrogenetic grids based on dry peridotite experiments [*Herzberg*, 2011; *Herzberg and Asimow*, 2008] would introduce errors in the back calculations to primary magmas. Consequently, we corrected for crystal fractionation by assuming that (1) H_2O contents of the SW Japan primary basalts are $<$2% [*Zellmer et al*., 2012] and (2) mantle melting is deeper than 2 GPa. We apply $>$2 GPa cotectics from both peridotite and pyroxenite sources using CMAS plots [*Herzberg*, 2011]. Details of the model and the model calculations are given in Appendix B and the results are shown in Figure 11.

Back calculations begin with representative MgO-rich parental basalts from Kannabe and Abu OIB, Yokota ABL/ABH, and Abu SAB/SHO. Both the original parental and calculated primary compositions are listed in supporting informations 1 and 5, respectively. We added 0–16 wt. % clinopyroxene and 7–26 wt. % olivine. The sum (17–36 wt. %) is almost equal to the amount of olivine addition required to reach equilibrium with Fo_{90} as an alternate indicator of primary melts equilibrated with the mantle [*Herzberg and Asimow*, 2008]. Although the difference has little effect on the trace element composition of primary melts it is important for the major elements. We will use the CMAS plot to examine slab and mantle melts in later sections, so use of the same scheme for all primary magma estimates is convenient (see section 6.5.5).

Most of the primary basalts plot in the pyroxenite field of *Herzberg and Asimow* [2008] in Figure 11a, which is also true for many more ordinary arc basalts. This could reflect pyroxene-rich sources resulting from the addition of slab-derived silicic melt to the mantle wedge [*Kogiso et al*., 2004]. However, it is more likely a result of expanding the olivine volume by addition of H_2O [*Kushiro*, 1969]. Our estimated primary melt compositions lie in the peridotite field of the CMAS plot in the pressure range 2.0–3.2 GPa (Figures 11b and 11c), and rear the 2–3 GPa garnet lherzorite multiple saturation points of *Grove et al*. [2013] and *Till et al*. [2012a] (Appendix B2 and Figure A1). The composition of melts from ol+opx+cpx-saturated experiments with natural peridotites at 2–3 GPa from the LEPR database of *Hirschmann et al*. [2008] lie near the same peridotite cotectics (see shaded areas in Figures 11b and 11c). These indications of derivation from a peridotite source support our use of ABS4 which was designed for peridotite melting. The 2–3 GPa pressures indicate a relatively deep source for the SW Japan basalts. Two SAB samples plot in the pyroxenite field, to

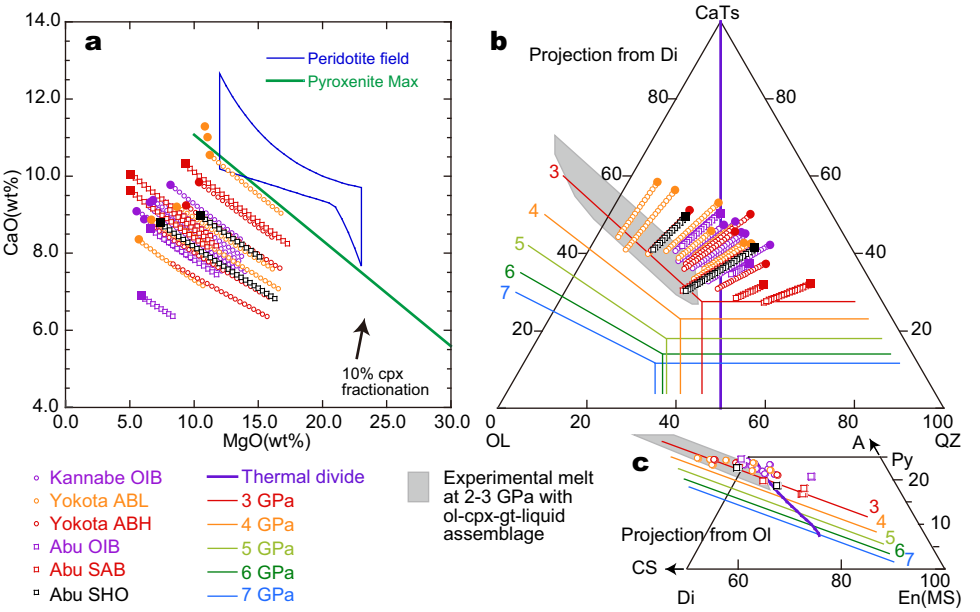

Figure 11. Estimates of primary magma compositions for parental basalts (not adakites or HMA) that are given in supporting information 1. (a) The blue peridotite field and green maximum CaO for melts of pyroxenite and (b) the 3–7 GPa cotectics and dark blue thermal divide are from *Herzberg* [2011]. Solid symbols show the result of adding variable amounts of clinopyroxene to the parental compositions. The actual amount of clinopyroxene is given in supporting information 5, and the effect of the addition is illustrated by the arrow for 10%. (b and c)Then, the clinopyroxene fractionation-corrected compositions were adjusted by adding equilibrated olivine until the magma compositions reached the pressure in the CaTs-Ol-Qz diagram that is indicated by its location in the Py(A)-Di(CS)-En(MS) of *Herzberg* [2011]. The final composition (i.e., the last open symbol on each olivine-addition line) is the primary melt composition for that sample (see supporting information 5). The gray field in Figures 11b and 11c show the composition of melts from melting experiments of peridotite at 2–3 GPa from the LEPR database of *Hirschmann et al.* [2008]. The validity of our models is confirmed by the agreement between our primary melt compositions and the experimental melt compositions.

the right of the thermal divide in Figures 11b and 11c, and farthest from the multiple saturation points of *Till et al*. [2012a] in Figure A1, reflecting their more silica-rich source compositions relative to AB. This will be discussed in section 6.5.5.

Our back calculations for the trace element concentrations in these primary melts used clinopyroxene partition coefficients from *Wood and Blundy* [1997] and *Pilet et al*., [2011], and olivine partition coefficients from *Bédard* [2005]. Our estimated primary magma compositions for OIB, AB, SHO, and SAB are given in supporting information 6.

6.3. Target Magma Composition for ABS4

In light of the differentiation processes in each rock suite as discussed above, we now need to choose one primary melt composition as the target to explain by subcrustal processes using ABS4. Supporting information 6 compiles the major and trace element compositions of all the possible primary melts, and the trace element compositions are shown in Figures 12a–12i. We used the average for each suite as our target. We also used the average isotopic compositions in all cases in which the isotopic compositions scatter widely and without correlation against SiO_2. However, when there is crustal assimilation (i.e., a correlation between isotopic composition and SiO_2 as in Daisen ADK), we chose compositions at the silica-poor end of the trends (Figure 8). This criterion applies to all isotopes for SHO and SAB and some isotopes for ABL/ABH. Our target isotope compositions are given in supporting information 6 and shown by circles in Figure 8.

6.4. Compositions of Mantle and Slab Source Materials for ABS4

We concluded above that the parental magmas for all suites are derived from the mantle or slab or both rather than the crust. Our next task is to estimate the slab and mantle processes that generate the target composition for each suite. To do this, we need to assume compositions of the mantle and the slab beneath SW Japan. New acronyms (e.g., PERID, MwP) in this and following sections refer to parameters in our ABS4 models and are defined in Table A1.

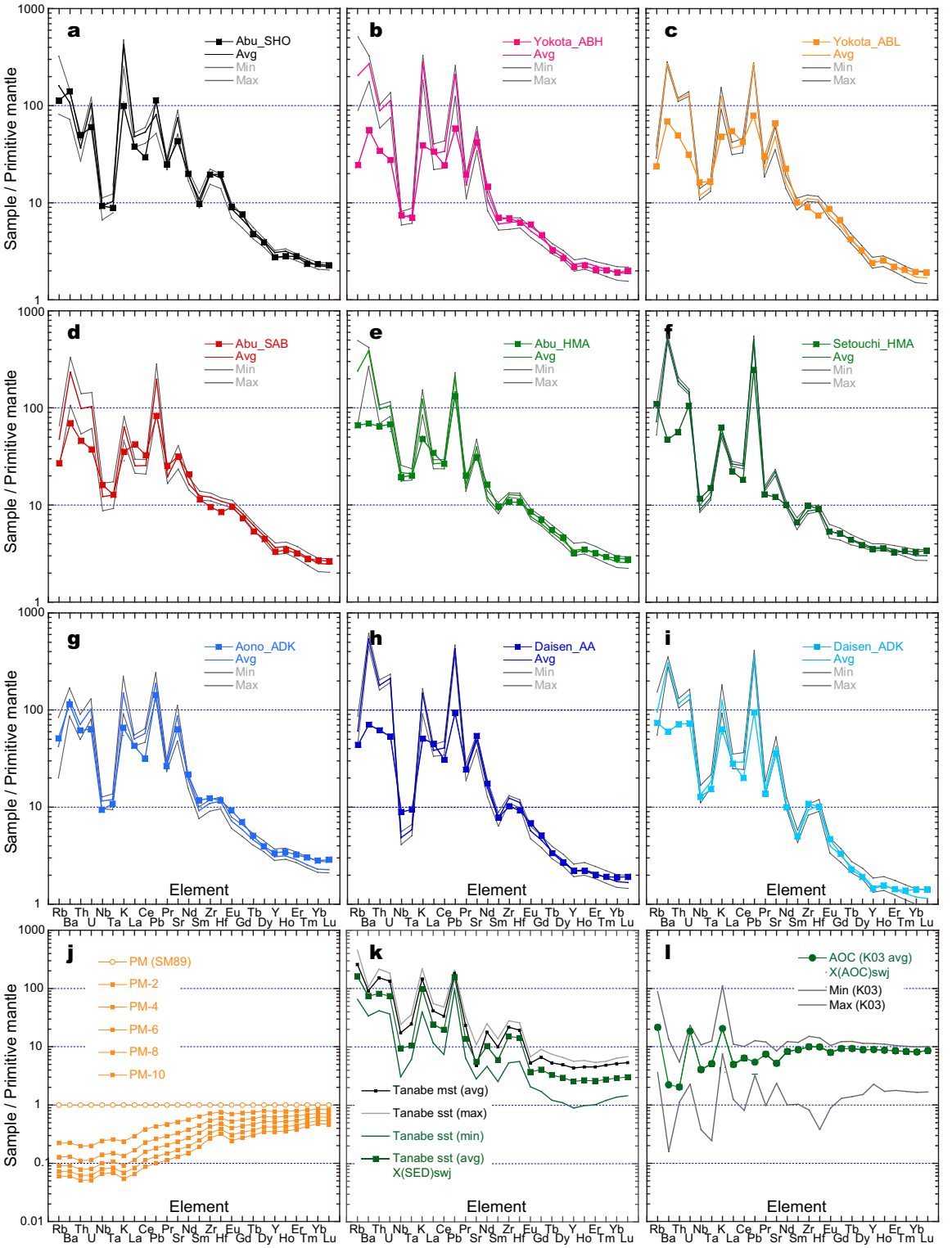

Figure 12. (a–i) Primary magma compositions calculated using ABS4, and comparison to nine target primary magma compositions. The thick lines with filled square symbols are the target magmas from supporting information 6. The thick lines without symbols are the average of calculated parent magmas from supporting information 6. The thin gray lines show the 2 sigma range of satisfactory matches, also from supporting information 6. All values are normalized to the primitive mantle composition of *Sun and McDonough* [1989]. The compositions of source materials are shown in Figures 12j–12l: PM (SM89) is the primitive mantle of *Sun and McDonough* [1989]; PM-2 to PM-10 shows residues after extracting 2–10% MORB melt from PM; AOC (K03) is the average and 1 sigma the range of altered oceanic crust compositions from ODP Site 1149 [*Kelley et al*., 2003]; Tanabe sst and mst are the average composition of turbidite sandstone and mudstone of the Tanabe Group from *Roser et al*. [2000]; and X(AOC)swj and X(SED)swj show the altered oceanic crust and sediment compositions assumed in this paper.

6.4.1. Mantle Wedge Composition

Although SW Japan OIB is more enriched in Ba and Sr than oceanic OIB, it is the least affected by the slab component. Therefore, we chose the average isotopic compositions of Kannabe OIBL and Abu OIB for the mantle wedge because they are the most common OIB types. Their compositions are shown in the orange rectangles in Figure 8, and our chosen compositions are shown in Figures 7 and 8 by orange stars. They are similar to those used by *Tatsumi and Hanyu* [2003] which they deduced from Miocene Setouchi SAB.

Because the trace element composition of the mantle wedge also is difficult to determine, we considered global estimates for depleted [*Workman and Hart*, 2005] and primitive mantle [*Sun and McDonough*, 1989] for PERID, including its base just above the slab (MwP). Because SW Japan OIB has a trace element composition similar to oceanic OIB [*Sun and McDonough*, 1989], we used primitive mantle concentrations for the mantle wedge as in our earlier papers [*Kimura and Stern*, 2008]. Depletion from these values is a free variable in our models (see examples in Figure 12j).

6.4.2. Slab Sediment Composition

For the trace element composition of the sediment input, we used the average composition of turbidite sediment in a Miocene fore-arc basin in SW Japan (~16 Ma) [*Roser et al*., 2000]. This is reasonable because these Miocene turbidites are the immediate source of the trench fill sediments in the modern Nankai Trough and were reworked from the same sources that have fed the Nankai Trough throughout the Neogene and, therefore, would have been in the trench at 13–14 Ma when the plate now beneath the volcanic arc was at the trench [*Kimura et al*., 2005a]. Because the isotopic compositions of the Miocene turbidites have not been measured, we used average values for the current Nankai Trough sediments [*Shimoda et al*., 1998; *Tatsumi et al*., 2008b] (supporting information 7).

6.4.3. Slab Altered Oceanic Crust (AOC) Composition

For AOC trace element concentrations, we assumed the weighted average composition of altered MORB in ODP Site 1149 [*Chauvel et al*., 2009; *Hauff et al*., 2003; *Kelley et al*., 2003] (Figure 12l). We assumed that the isotopic composition of AOC is the same as the most depleted Shikoku Basin basalts [*Hickey-Vargas*, 1998], apart from more radiogenic Sr derived from seawater alteration for which we used the average value for Site 1149 AOC [*Hauff et al*., 2003]. All the slab compositions are given in supporting information 7.

6.4.4. Slab Dike/Gabbro/Peridotite Compositions

Oceanic lithosphere has dike, gabbro, and peridotite layers beneath AOC. We assume that the slab peridotite (SlbP) has the trace element composition of depleted MORB source mantle (DMM) [*Workman and Hart*, 2005] because the mantle beneath the Shikoku Basin is depleted [*Hickey-Vargas*, 1998]. We assume that the isotopic composition of SlbP is the same as for AOC except for Sr for which we used the most depleted value of Shikoku Basin basalts [*Hickey-Vargas*, 1998].

The trace element composition of dikes is assumed to be the same as for normal (N)-MORB [*Pearce and Parkinson*, 1993] because they are quenched N-MORB [*Hickey-Vargas*, 1998] and not much affected by sea water alteration [*Staudigel et al*., 1996]. The composition of the gabbro layer is assumed to be 0.5 times N-MORB assuming that it is olivine, clinopyroxene, and plagioclase accumulated from MORB based on the high and homogeneous seismic velocity of oceanic lower crustal Layer 3 (*Vp* ~7 km/s) [*Wilson*, 1989]. The isotopic compositions for gabbro/dike are as same as for slab peridotite [*Hickey-Vargas*, 1998] (supporting information 7).

6.5. Forward Models Using Arc Basalt Simulator Version 4 (ABS4)

6.5.1. ABS4 Overview

ABS4 is a geochemical mass balance model for arc magma genesis including calculations of slab dehydration/melting and fluid/melt-fluxed melting of peridotite using thermodynamically [*Connolly and Kerrick*, 1987; *Connolly and Petrini*, 2002; *Ghiorso et al*., 2002] and experimentally [*Hermann and Spandler*, 2008; *Katz et al*., 2003; *Schmidt et al*., 2004; *Skora and Blundy*, 2010] tuned petrogenetic grids for both prograde metamorphism and melting of the slab, and fluid/melt-fluxed melting of peridotite in the mantle wedge [*Kimura et al*., 2010]. Details of ABS4 and the differences from ABS3 are given in Appendix C. A brief summary is given below. The acronyms used in ABS4 are summarized in Table A1 and defined below. A representative ABS4 Excel spreadsheet is available in supporting information 8 dynamic content.

ABS4 makes the following assumptions that are keyed to specific Worksheets in the ABS program (supporting information 8). (1) All layers of the oceanic crust and the first 10 km of underlying slab mantle are fully

hydrated as assumed by *van Keken et al*. [2011]. From bottom to top, these layers are the slab mantle (SlbP), lower and upper gabbro (LGAB/UGAB), dike (DIKE), lower and upper basalt (LBAS/UBAS = AOC), sediment (SED), and the basal mantle wedge peridotite that is mechanically coupled to the slab (MwP). The modal composition of each layer during the prograde metamorphism is calculated using Perple_X [*Connolly and Kerrick*, 1987; *Connolly and Petrini*, 2002] for the subsolidus, and our parameterization of experimental results for supersolidus regions [*Kimura et al*., 2010]. This information can be found in ABS4 Worksheet Slb_Mode. (2) Each slab layer acts as a sponge that receives all the fluids/melts lost from the layer beneath and releases reactants to the layer above. This reaction is controlled by the degree of dehydration or partial melting of each slab unit and is similar to chromatographic reactions (see Figure A2). This information can be found in ABS4 Worksheet SDMS4.0. (3) Element partitioning during slab dehydration and melting is calculated using temperature-dependent partition coefficients where known (D(Cpx) and D(Gar) [*Kessel et al*., 2005], D(Opx) and D(Amp) [*Kimura et al*., 2010]), and fixed partition coefficients otherwise (e.g., for phlogopite, phengite, zoisite, chlorite, etc.) [*Feineman et al*., 2007; *Green and Adam*, 2002]. The resulting bulk partition coefficient of each layer at each depth for the appropriate P-T path can be found in rows 290–498 of ABS4 Worksheet SDMS4.0. (4) The thermal model for each layer from *Syracuse et al*. [2010] and *van Keken et al*. [2011], modified slightly according to P. E. van Keken (personal communication, 2012) is applicable. This information can be found in ABS4 Worksheet Slb_PT(PvK2011). (4) The solidi, percent melting, and residual mineral percentages for SED and AOC from *Hermann and Spandler* [2008], *Schmidt et al*. [2004], and *Skora and Blundy* [2012] are applicable, and the water-saturated and dehydration solidi of AOC and SED are the same (~700°C and ~770°C at 3 GPa, respectively). This information can be found in ABS4 Worksheet Slb_Mode. (5) Fluids or melts from the AOC, SED, and MwP layers at their appropriate depth mix in proportions defined by the user and are added to the overlying mantle to cause flux melting. (6) The primary arc magmas are derived from melting of mantle wedge PERID by fluxing with the mixed slab fluid/melt. The flux melting model of *Ozawa* [2001] and *Ozawa and Shimizu* [1995] is applicable. This information can be found in ABS4 Worksheets OSM and IOSM. (7) The fixed D(Ol), D(Cpx), D(Opx), and D(Gar) trace element partition coefficients from *Green et al*. [2000] apply to hydrous mantle melting. (8) The solidi and percent melting are calculated using the experimentally determined parameterization of *Katz et al*. [2003], and residual mineral percentages for PERID and the effects of flux melting are calculated using the thermodynamic model of pMELTS [*Ghiorso et al*., 2002]. This information can be found in ABS4 Worksheets Peri_Mode, MJ_pMELTS, and Katz+.

The slab P-T path is one of the most important predefined parameters. In general, ABS4 assumes the geodynamic model of *Syracuse et al*. [2010] and *van Keken et al*. [2011] but they did not give a slab temperature profile the arc for Nankai. Instead, we used values provided by P. E. van Keken (personal communication, 2012) that are given for each of the eight slab layers in Worksheet Slb_PT(PvK2011).

ABS4 is a forward model that calculates a primary magma composition from slab and mantle sources based on nine intensive and extensive petrological parameters (see Appendix C). These parameters can be varied by the user and the resulting calculated magma composition compared to a target magma that is based on observations. Incompatible trace element, Sr-Nd-Hf-Pb isotope, and major element compositions are used in the comparison. A Monte Carlo calculation is used to make a quantitative comparison in order to avoid artificial correlations between the parameters. Successful results are those in which calculated and observed compositions agree to within user-defined limits (supporting information 8).

Representative successful ABS4 calculation results for major, trace, and isotope compositions, and the corresponding intensive/extensive parameters for slab and mantle melting, are listed in supporting information 6 and shown in Figures 12a–12i for incompatible trace elements. We modeled target primary magma compositions for Abu SHO, Yokota ABH/ABL, Abu SAB, Abu HMA, Setouchi HMA, Aono ADK, and Daisen AA/ADK that are given in supporting information 6 but we did not model OIB because ABS4 is particularly designed for arc magmas.

6.5.2. ABS4 Results: Incompatible Trace Elements

We start each model by fitting the incompatible trace element concentrations. The matches for each target primary magma in supporting information 6 are averages and one standard deviation for approximately 100 satisfactory models per target in which agreement between the forward calculation and the target composition lies within the limits that are given in Appendices C7 and C8. The range of satisfactory results is shown by the minimum and maximum lines in Figure 12 that bracket the 2 sigma deviation spread of

satisfactory results. As shown in this diagram, Rb, Ba, Th, U, K, and Pb concentrations in otherwise successful matches are often too high. Sr generally agrees except for high values for Setouchi HMA. The overestimate of these elements probably reflects unrealistic compositions and mineralogies for the SED and AOC components, or inaccurate partition coefficients for these elements.

Twenty incompatible trace elements excluding those listed above are given high priority in fitting calculations [*Kimura et al*., 2009, 2010]. Among them, the highest priority is given to REEs (see Appendices C7 and C8), because their abundances and patterns constrain many important parameters such as the mass fraction of slab flux, source mantle depletion, and the degree and depth of mantle melting.

Residual accessory phases in the slab may exercise important controls on trace elements in slab-derived fluids and melts [*Hermann and Rubatto*, 2009]. Perple_X solutions include modes of phengite and rutile in SED and AOC. For them, we use fixed partition coefficients from *Ayers et al*. [1997] and *Green et al*. [2000]. In addition, the garnet and clinopyroxene partition coefficients of *Kessel et al*. [2005] already include the effects of some residual rutile in their experiments. The calculated HFSE concentrations can be refined in ABS4 by modifying the amount of rutile in the residual SED and AOC (supporting information 8 ABS4 CONTROL_PANEL Worksheet Cell L19). For the models in this paper, successful matches of HFSE concentrations and HFSE/REE ratios typically required up to 1% more rutile than calculated using Perple_X. Even so, Zr-Hf and Nb-Ta abundances are matched only to within 25–40% in our models (Figure 12). Other potentially important accessory minerals during slab dehydration and melting include zircon, allanite, monazite, and apatite. ABS4 allows the user to specify the mode of zircon and allanite in the slab residue, but we have not used that capability for the models in this paper.

6.5.3. ABS4 Results: Sr-Nd-Hf-Pb Isotopes

The ABS4 calculation results for isotopes are shown in Figure 13 by open symbols with error bars indicating averages with 2 sigma deviations. The target primary magma compositions are almost always matched within those errors, except for Sr-Nd-Hf isotopes in Setouchi HMA. This shows that the ABS4 results successfully keep internal consistency between Sr-Nd-Hf±Pb element abundances and Sr-Nd-Hf-Pb isotopes, which is often a problem for forward models.

Overall, the successful results show mixing between SED, AOC, and PERID source components. However, complex geochemical mixing processes are assumed in ABS4 (see Appendix C). The assumptions that most affect isotope ratios include (1) reactions between fluids/melts and overlying layers in the slab, (2) effects of fracture versus porous flow of liquids in the slab, (3) mixing of slab fluid/melt from SED/AOC/MwP sources, and (4) open system fluid/melt fluxed-mantle melting controlled by the mass fraction of flux and the degree of mantle melting. Because the resulting mixing lines between SED/AOC/PERID sources are not simple hyperbolae in isotope ratio diagrams as in most other models, mixing lines are not shown in Figure 13. However, isotopically enriched slab components are dominated by SED, whereas depleted slab components are mostly from AOC (see Figure 7). The SW Japan PERID component lies between SED and AOC, so that the contribution of PERID is not prominent in isotopic variations.

6.5.4. ABS4 Results: Major Elements

The major element composition of primary melts calculated using ABS3.1 was discussed by *Li et al*. [2013] for low-Ca boninite and high-Mg adakite in the IBM arc. The magmatic SiO_2 content is fundamentally important in discriminating between silica undersaturated (strongly alkaline) versus oversaturated (subalkaline) basalts, and estimating the corresponding depth of mantle melting [*Kushiro*, 1973]. The high SiO_2 of HMA and ADK may be caused by slab melt-fluxed melting of mantle peridotite [*Kelemen et al*., 1998] or H_2O-fluxed melting [*Umino and Kushiro*, 1989]. Trace element mass balances alone cannot distinguish between these alternatives. Therefore, we used the SiO_2 content of target primary melts as an additional filter. ABS3 and ABS4 calculate the major element composition of open system mantle melting using the pMELTS algorithm [see Appendix C and *Kimura et al*., 2010]. Although such calculations have large uncertainties, they can still provide a useful guideline.

The major element results for each target composition are shown in Figure 14 with mean values and 2 sigma error bars. The results almost reproduce the major element compositions of primary magmas. In addition to SiO_2 MgO and Fe_2O_3 contents for SHO/AB/SAB/HMA/AA/ADK are reproduced to within 2–4 wt. % (Figure 14a). Calculated Al_2O_3 contents are systematically high, whereas CaO are systematically low. This

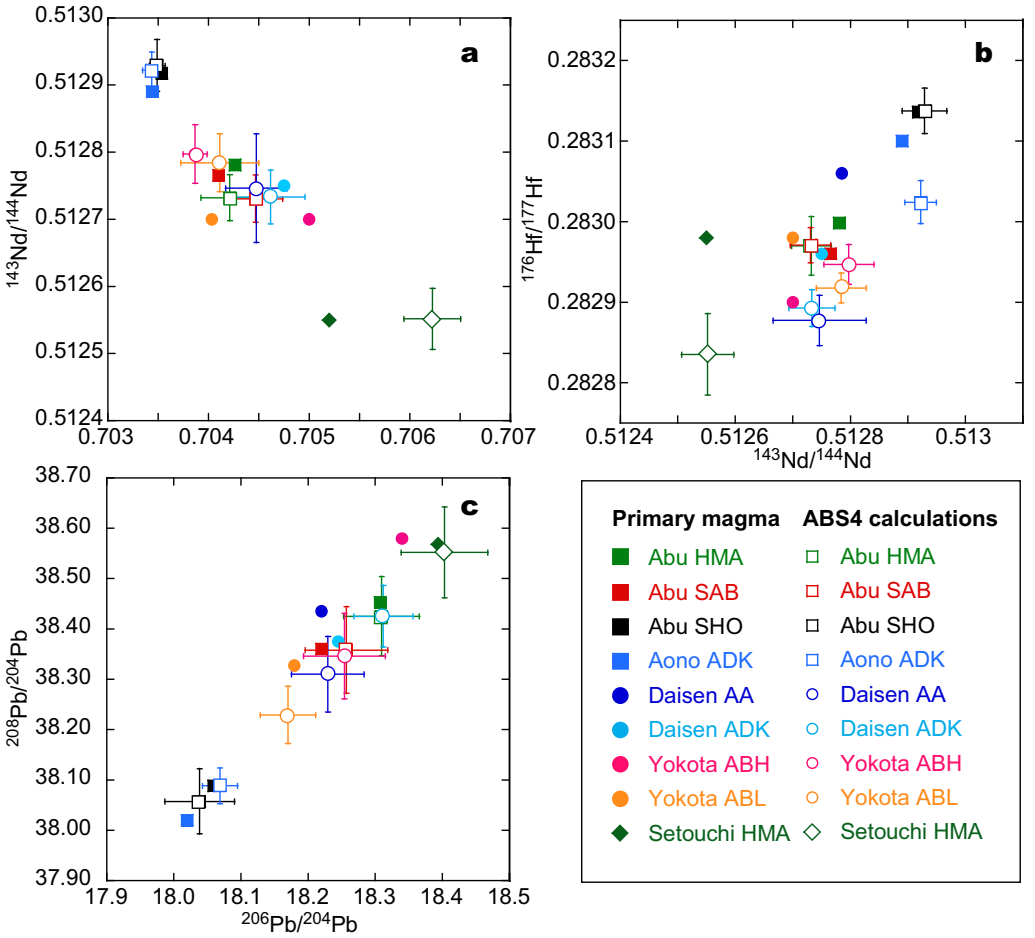

Figure 13. Comparison between the isotope compositions of target (solid symbols) and calculated magmas using ABS4. The ABS4 results are averages (open symbols) with 2 sigma standard deviations (error bars).

reflects uncertainties in our assumed slab melt composition (shown by a yellow star in Figure 14) and in the pMELTS calculations [*Kimura et al.*, 2010].

6.5.5. ABS4 Results: Phase Relations of the Primary Melt

The major element compositions of the calculated primary melts are discussed next using CMAS plots (Ol-CaTs-Qz projected from Di: Figure 15). As noted in section 6.2.3 (Figure 11), the primary basalt compositions of SHO/AB/SAB all plot near the 2–3 GPa peridotite cotectics (Figures 15a–15d). ABS4 results plot on lines that emanate from the slab melt composition (yellow star in Figure 15), pass through the model results, and extend to pure mantle melts at an appropriate pressure. This indicates that, after filtering on SiO_2, ABS4 results show the expected mixing between a slab-derived felsic melt and basalt melts from PERID.

The target and calculated primary AA/ADK melt compositions plot close to the slab melt composition and near the high-silica end of the silica-rich pyroxenite cotectic (Liquid (L) + Qz + Cpx + Gt) of *Herzberg* [2011]. This suggests that AA/ADK is a melt of quartz-eclogite in the garnet stability field that later reacted with mantle peridotite (Figures 15g–15i).

Abu and Setouchi HMA plot between the quartz-eclogite (slab) melt and basalt melts from PERID (Figures 15e and 15f). The apparent basalt melt components for HMA and AA/ADK point to lower pressure cotectics (<2 GPa) in contrast to deeper equilibration for the basaltic suites (2.5–3 GPa). This is consistent with ABS4 estimates for mantle melting depths as will be discussed in section 6.6.3.

6.5.6. ABS4 Results: Residual Mantle Mineralogy

The residual mantle mineralogy calculated by ABS4 for each suite [see Appendix C and *Kimura et al.*, 2010, for the method] is shown in Figure 16. In all cases, the residue lies between the source PERID (DMM)

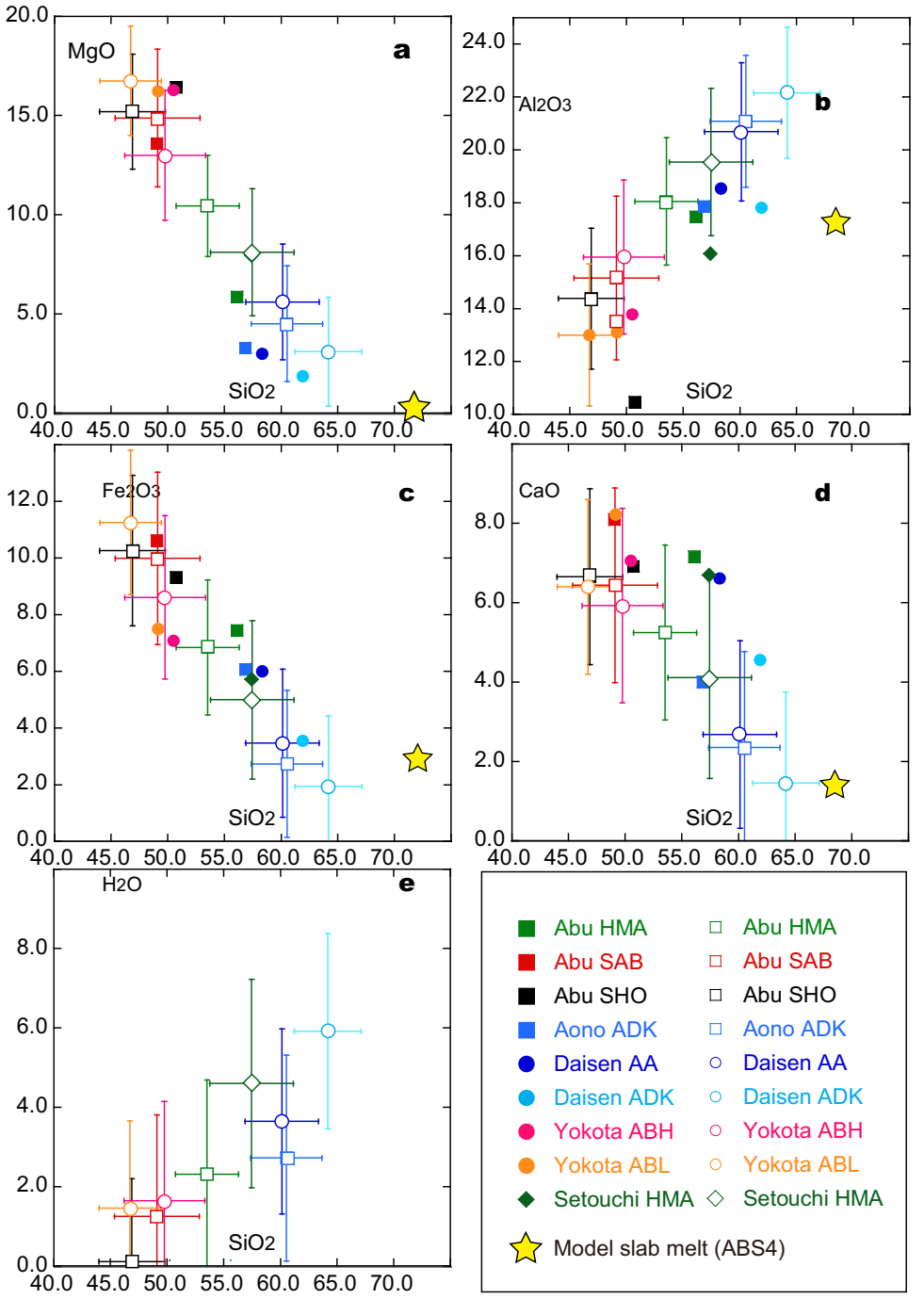

Figure 14. Comparison of the major element compositions between the target (solid symbols) and calculated magmas using ABS4. ABS4 results are averages (open symbols) with 2 sigma standard deviations (error bars). Agreement is better for SiO_2, MgO, and FeO than for Al_2O_3 and CaO. H_2O compositions are predictions from ABS4. See discussion in the text about H_2O in primary magmas.

composition and the Opx apex (the amount of garnet is not shown). This indicates that the residual mantle mineralogy is largely controlled by reactions between peridotite and a silicic slab melt. Increases in SiO_2 in PERID result in Opx-rich residua due to consumption of olivine and clinopyroxene in a peritectic reaction [*Kelemen et al.*, 1998], and the reactions are somehow reproduced by ABS4 using the pMELTS algorithm. ABS4 calculations for fluid-fluxed mantle melting at 1–3 GPa exemplified by the North Izu frontal arc are also shown for comparison (see DMM 1.0 GPa–3.0 GPa results in Figure 16).

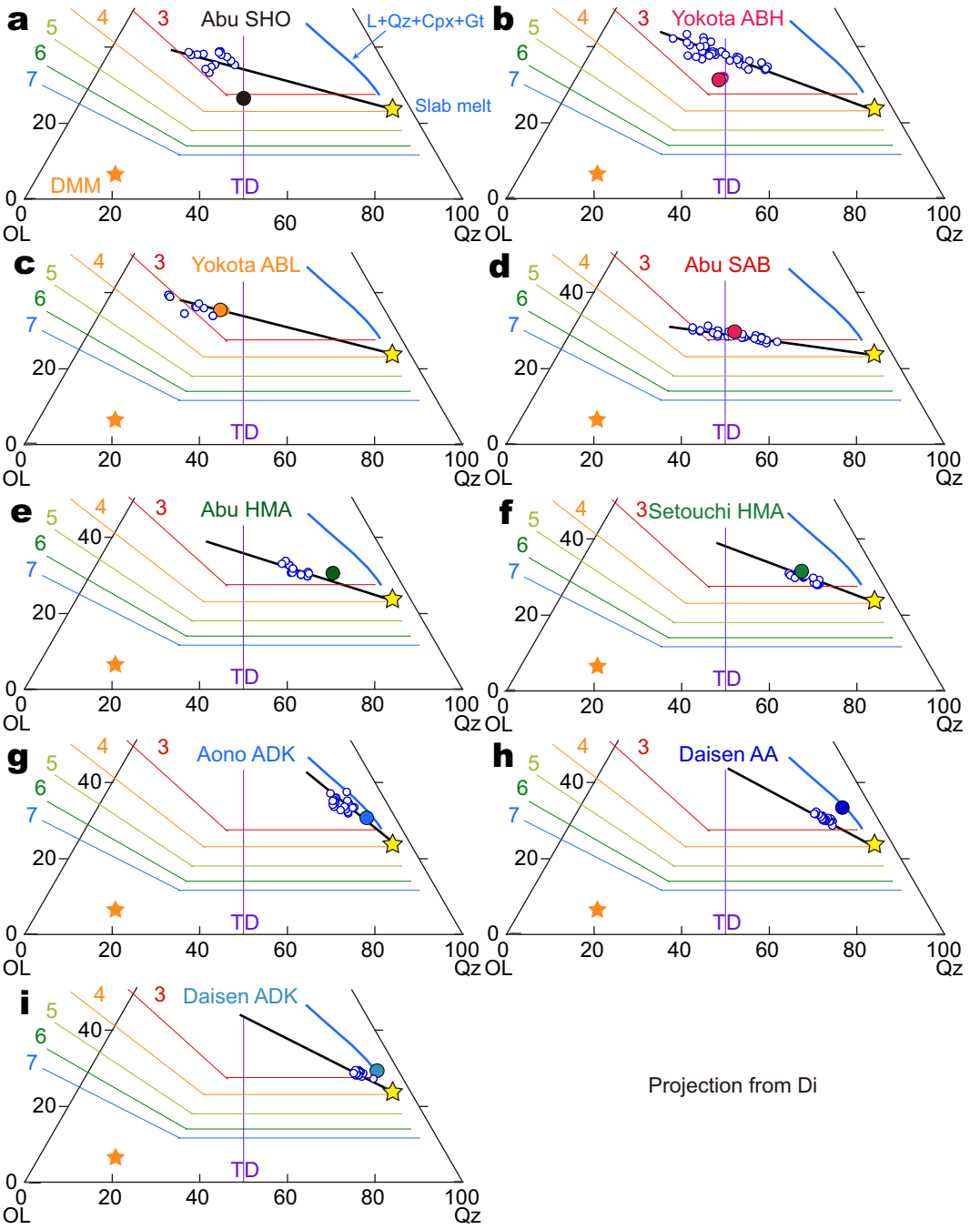

Figure 15. CaTs-Ol-Qz plot (a–i) comparing the target primary melt composition (solid colored circles) to primary melt compositions calculated using ABS4 (small blue open circles), the source PERID from *Workman and Hart* [2005] (solid orange star), and an average slab melt (solid yellow star) from *Moyen* [2009] and *Moyen and Stevens* [2006]. The rainbow colored thin lines show peridotite cotectics at 3–7 GPa from *Herzberg* [2011]. The thick blue line within the L + Qq + Cpx + Gt field shows the silica-rich pyroxenite cotectic from *Herzberg* [2011] The vertical line labeled TD is a thermal divide, also from *Herzberg* [2011].

The calculated residual mineralogy for SW Japan magmas overlaps the field of mantle xenoliths from Shiveluch volcano (Figure 16). The xenoliths were considered to be examples of melt fluxed mantle by *Bryant et al*. [2007]. In contrast, mantle xenoliths from the NE Japan arc [*Abe and Arai*, 2005] mostly overlap the residue from fluid-fluxed melting. Therefore, ABS4 calculations reproduce quite well the expected residual mantle mineralogy for slab melt-fluxed mantle melting beneath the SW Japan hot subduction zone.

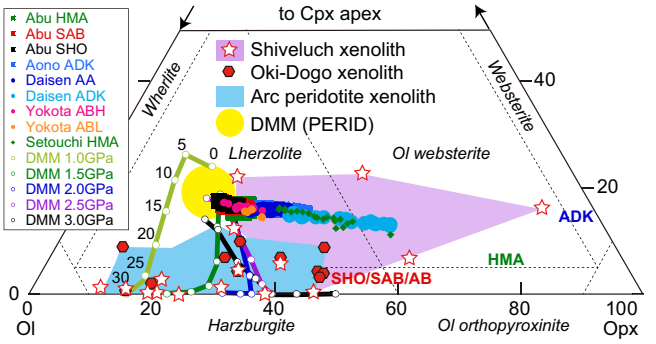

Figure 16. Residual mantle mineralogy for the primary magmas in SW Japan arc calculated by ABS4. ABS4 calculations for the DMM source without slab flux at 1.0–3.0 GPa and 0–30% partial melting are also shown for comparison by thick colored lines. Modal compositions of supra-subduction zone mantle xenoliths from Shiveluch volcano (red open stars surrounding the purple field) [*Bryant et al*., 2007] and those from Oki Island (red filled hexagons and light blue field) [*Abe and Arai*, 2005] are also shown for comparison.

The calculated residual mineralogy falls in the lherzorite, Ol-websterite, Ol-orthopyroxenite, and websterite fields. All of these contain olivine in contrast to the Ol-free pyroxenite source for HMA and AA/ADK primary melts inferred from the CMAS plots (Figure 15). This is due to mixing between PERID-derived basalt melts and a slab-derived felsic melt to account for HMA and AA/ADK, as discussed in section 6.5.5. The apparent Ol-free pyroxenite lithology inferred from Figure 15 does not reflect the source mantle for SW Japan. Instead, an Opx-rich residue is expected during production of HMA and AA/ADK, similar to the mantle xenoliths from Setouchi HMA [*Tsuchiya et al*., 2005].

6.6. Intensive-Extensive Parameters of Magma Genesis

As shown in the preceding section, the primary magma calculated using ABS4 can reasonably well reproduce the incompatible trace elements, Sr-Nd-Hf-Pb isotopes, major element compositions, and residual mantle mineralogy during genesis of SHO, ABL/ABH, SAB, HMA, and AA/ADK. We will now explore the implied conditions of slab and mantle melting.

ABS4 uses nine intensive/extensive variables including: (1) the depth of melt release from the slab [Slab P]; (2) the extent of liquid focusing in the slab [%R slab] related to diffuse versus channel flow; (3) the fraction of slab flux from AOC [Fliq(AOC)], SED [Fliq(SED)], and MwP [Fliq(DMM)]; (4) mantle melting pressure [P]; (5) mantle melting temperature [T]; (6) the mass fraction of slab flux added to the mantle [Fslb liq.%]; (7) degree of mantle melting [F]; and (9) the extent of depletion of the mantle source prior to melting [%MORBext.]. Average results and standard deviations for these parameters are included in supporting information 6, and ~20 successful results for each suite are shown graphically in Figure 17. We show results that cover the range of the variables listed above drawn from the Monte Carlo random fittings.

6.6.1. Depth of Slab Melt Release [Slb P], Slab Liquid Fraction [Fliq(AOC/SED/DMM)], and Focusing of Slab Melt [%R slab]

We assumed the P-T paths for eight slab layers Nankai from P. E. van Keken (personal communication, 2012). This model predicts melting of both AOC and SED deeper than ~80 km (~2.5 GPa) under water-saturated conditions (supporting information 8, ABS4 [Slb_Mode] Worksheet). We used the water-saturated solidi because we assume saturation of bound water during prograde metamorphism in each layer. The necessary water is supplied from the lower layer. This type of melting is termed "flush melting" by *Skora and Blundy* [2010]. Calculated degrees of melting of both the AOC and SED layers vary from 32 to 37%.

All successful models for the SW Japan arc require slab melting. However, melting degrees and the composition of the slab melt do not change significantly between 2.5 and 6.0 GPa because the P-T path of the slab is subparallel to the solidus [*Syracuse et al*., 2010; *van Keken et al*., 2011] (also see [Slb_Mode] Worksheet of ABS4 in supporting information 8). Consequently, ABS4 models are successful for a wide range of pressures (3.7–5.0 GPa) of slab melting (see supporting information 6). In contrast, colder arcs may involve only fluid-fluxed melting beneath the volcanic front and slab melts only beneath rear arc volcanoes [e.g., Izu: *Hochstaedter et al*., 2001; *Kimura et al*., 2010].

A flux component from the base of the mantle wedge overlying the slab (MwP: [Fliq(DMM)]) is not necessary in SW Japan in contrast to its fundamental importance in modern Izu [*Kimura et al*., 2010] and for the low-Ca boninite early in Izu arc history [*Li et al*., 2013]. None of the successful ABS4 models for SW Japan required this layer mainly because of the steep REE patterns in the primary magmas combined with low degrees of mantle melting. The slab fluxes are only melts of AOC [Fliq(AOC)] and SED [Fliq(SED)].

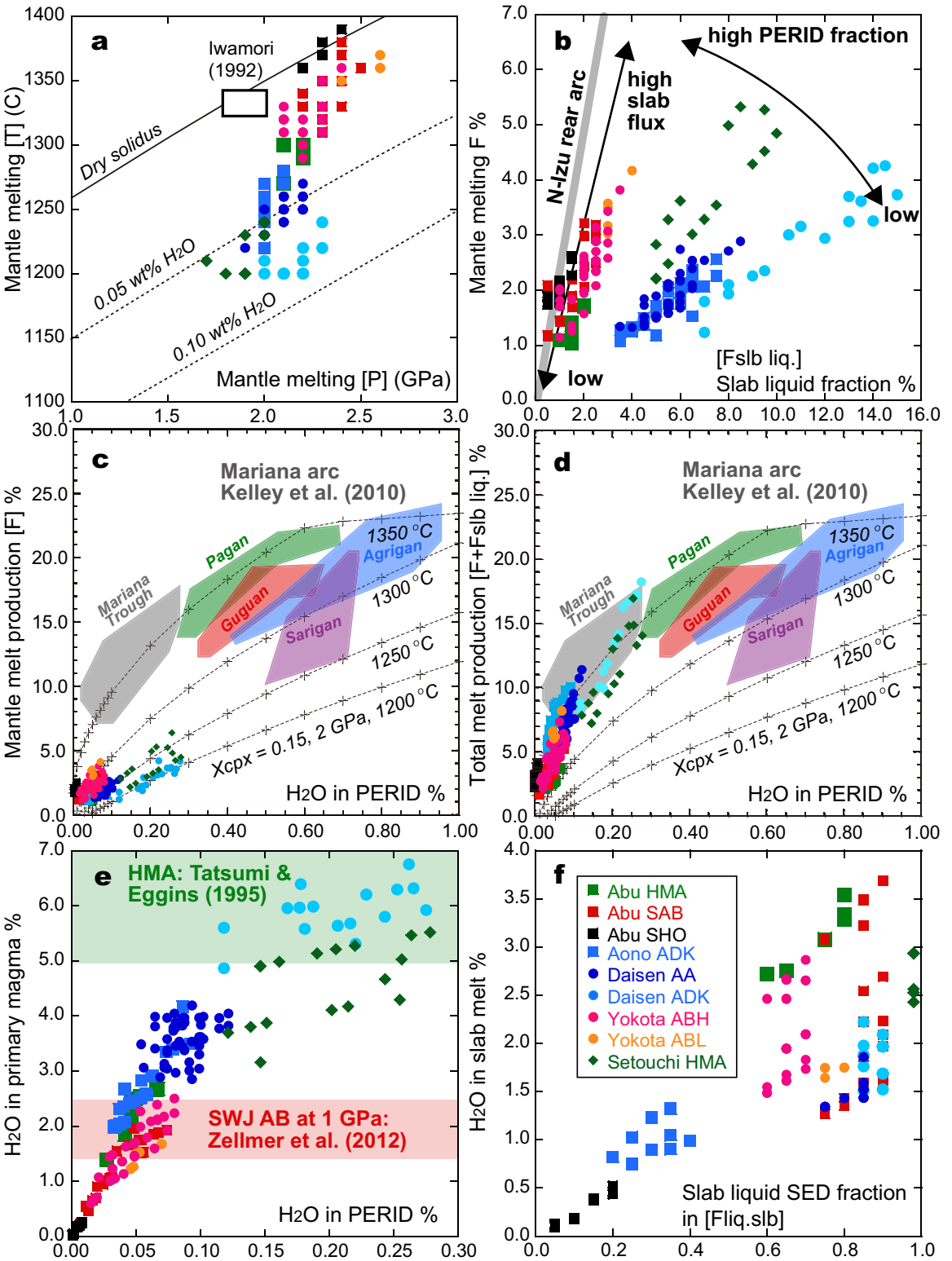

Figure 17. Intensive/extensive parameters assumed and calculated by ABS4 for successful matches of target primary magmas for the SW Japan arc. Results for representative matches that cover the range of parameters are shown for each magma suite. The dry and damp peridotite solidi in Figure 17a are from *Katz et al.* [2003]. The fields for the Mariana Trough and Mariana Arc basalts (Pagan, Guguan, Agrigan, and Sarigan), and the isothermal melting curves in Figures 17c and 17d, are from *Kelley et al.* [2010].

Consequently, the coupled flow that transports the lowermost mantle wedge "sponge" downward seems to be much diminished above hot slabs.

The [%R slb] parameter reflects the focusing of slab liquids as they move into higher layers (see Appendix C and Figure A2). The isotopic composition of the final slab liquid is especially sensitive to this parameter. Successful results for SW Japan generally have small [%R slb] values (25–50%) (supporting information 6) that we interpret as reflecting porous flow through the slab. Only Aono ADK requires higher values (~120%).

6.6.2. Mantle Depletion Prior to Melting [%MORB ext.]

Mantle more depleted than the Primitive Mantle of [*Sun and McDonough*, 1989] is required for most of the SW Japan suites. This is calculated in ABS4 as the residue from bulk partial melting of peridotite using the parameter [%MORB ext.]. Predepletions of 1–3% were required for most of the magma suites, but 5–9% for Daisen AA/ADK and ~7% for Yokota ABH (supporting information 6).

A 4 wt. % melt extraction is not enough to form DMM from PM, which requires ~10 wt. % [*Workman and Hart*, 2005]. Consequently, the SW Japan mantle has trace element concentrations similar to an E-MORB source. This is more enriched than in NE Japan and Izu where forward models require PERID to be 1–5% more depleted than DMM [*Hochstaedter et al*., 2001; *Kimura and Yoshida*, 2006; *Kimura et al*., 2010]. The more fertile mantle in SW Japan is consistent with its inferred greater isotopic enrichment (Figure 7) [*Hoang and Uto*, 2003; *Kimura and Stern*, 2008].

6.6.3. Mantle Melting Pressure [P] and Temperature [T]

Figure 17a shows the P-T conditions for mantle melting in the successful models for each magma suite. They result mostly from fitting the REE patterns and SiO_2. There is a crude positive correlation between P-T within the basaltic suites in the range 2.2–2.5 GPa and 1300–1390°C. SHO equilibrated at the highest P-T conditions ($P = 2.2$–2.5 GPa, $T = 1360$–1390°C), and SAB and ABL/ABH at slightly lower $T = 1280$–1350°C at similar P. In contrast, HMA equilibrated at lower $P = 1.6$–2.2 GPa and $T = 1190$–1300°C, and Aono and Daisen AA/ADK at the lowest $P = 2.0$–2.3 GPa and $T = 1200$–1260°C. The higher pressure origin for SHO and AB are consistent with their silica-deficient compositions. Estimated pressures >2 GPa are consistent with residual garnet in the sources (supporting information 6) and their HREE-depleted patterns (Figure 12). In all cases, the final depth of melt equilibration with the mantle lies between the top of the slab and base of the crust, but there is no spatial pattern.

Iwamori [1992] concluded that AB equilibrated with mantle peridotite at 1.65–1.90 GPa, 1320–1340°C (Figure 17) with $H_2O = 0.5$–1.5 wt. % and $CO_2 = 0.5$–1.0 wt. % in the primary melts. The major element composition of AB used in his experiments is similar to that of the ABL/ABH primary magmas in this study (supporting information 5). The estimated temperature range is similar in the two studies despite their very different constraints, although his estimated pressure and H_2O contents are slightly lower (Figure 14e).

HMA and AA/ADK appear to originate at shallower depths than the basaltic suites. Most, although not all, AA/ADK and HMA require a little residual garnet in their mantle source (supporting information 6). Intermediate-silica magma can be in equilibrium with garnet peridotite as shallow as 1 GPa [*Alonso-Perez et al*., 2009], which is consistent with the ABS4 results.

6.6.4. Degree of Mantle Melting [F] and the Mass Fraction of Slab-Melt Flux [Fslb liq.]

Figure 17b shows the inferred degree of mantle melting [F] as a function of the mass fraction of slab-melt flux [Fslb liq.] for the successful ABS4 models. The slope (dF/dflux) gives the productivity of flux melting. The suites define three distinct trends for SHO/AB/SAB, HMA, and AA/ADK, respectively. We draw three main conclusions from these relationships.

First, the degree of mantle melting is proportional to the slab-melt flux. This is petrologically reasonable because the slab-derived melts contain H_2O, and the addition of H_2O increases the degree of mantle melting at a given P-T [e.g., *Hirschmann et al*., 2008; *Kelley et al*., 2010].

Second, mantle melting productivity is greatest (the dF/dflux slope is steepest) for SHO/AB/SAB, intermediate for HMA, and lowest for AA/ADK decreasing from Aono ADK, to Daisen AA, to Daisen ADK (Figure 17a). We attribute the different slopes to differences in mantle temperature such that a fixed amount of flux results in the most mantle melting when the temperature is highest (for SHO/AB/SAB), and the least mantle melting when the temperature is lowest (for Daisen ADK).

Third, all *d*F/*d*flux slopes for SW Japan basalts are shallower than inferred by similar ABS models for the North Izu rear arc [*Kimura et al*., 2010] (Figure 17b). We attribute the relatively low degree of mantle melting beneath the SW Japan arc to low water in the slab flux in this hot subduction zone, and we attribute the low productivity of mantle melting in the unusual HMA and ADK suites to unusually low temperatures of melting.

We explore this idea further using Figure 17c which is similar to those in *Kelley et al*. [2010] and related papers about water contents and melting in other arcs and back arcs. This comparison is possible because ABS4 calculates H_2O contents in the fluxed peridotite source [H_2O in PERID] that is analogous to C_0 in *Kelley et al*. [2010] despite very different methods and assumptions in the two studies. H_2O in PERID has a crude positive correlation with degree of mantle melting [F] (Figure 17c) as is typical of subduction environments but not ocean ridges [*Kelley et al*., 2010]. Hydrous experiments also show that melt productivity defined as *d*F/*d*T decreases with the addition of H_2O to mantle peridotite [*Gaetani and Grove*, 1998; *Till et al*., 2012b]. In addition, the different slopes between SW Japan suites are the same in Figures 17b and 17c, and the most distinctive suites (HMA and ADK) have shallower slopes than anything in the Mariana Arc or Trough.

Our SHO suite plots on ABS4's $T = 1350°C$, $P = 2.0$ GPa isotherm (which is consistent with our estimate for the SHO mantle melting conditions; see Figure 17a) just as do basalts from the Mariana Trough and Pagan Island of *Kelley et al*. [2010]. This indicates that the hottest mantle beneath SW Japan is similar to that beneath the Mariana Trough and parts of the Mariana Arc, but with less H_2O (Figure 17c). AB/SAB share the same $T \sim 1300°C$ isotherm with Guguan and Agrigan from the Marianas, again with less H_2O. AA/ADK and HMA are on $T = 1200–1250°C$ isotherm, more Sarigan-like but with lower H_2O. The comparisons indicate that the SW Japan mantle has a wider range in temperature as well as less H_2O and, therefore, lower F than in the Mariana arc and back arc, supporting our conclusion above from Figure 17b. The *d*F/*d*H_2O slope for each suite is controlled by the local mantle temperature [T] but the overall lower [F] reflects drier mantle in SW Japan.

The degree of mantle melting [F] is small in SW Japan (Figure 17c) but slab melt production is twice or more the mantle melt production and the *d*(F+Fslb liq.)/*d*H_2O slopes of all rock suite almost overlap each other on $T = 1350°C$ isotherm (Figure 17d). Consequently, melt productivity estimates that are based only on major and trace element compositions or H_2O contents of basalts will be too low in hot subduction zones. Because ABS4 deals with [F] and [Fslb liq.] separately, we can see that SW Japan is characterized by high melt production from the slab due to the hot subduction.

Note that if the slab flux is water rich (e.g., at the N. Izu volcanic front) [*Kimura et al*., 2010] it mostly dissolves in the mantle melt. Therefore, [F] is almost equal to [F] + [Fslb liq.]. However, if the slab flux is water-poor melt (e.g., at the N. Izu rear arc [*Kimura et al*., 2010] and in SW Japan), then the total magma production should be close to [F] + [Fslb liq.].

6.6.5. H_2O in the Magmas

The H_2O contents of the most mafic Abu SAB and Yokota AB at ~1 GPa were estimated by *Zellmer et al*. [2012] to be 1.5–2.5 wt. % (Yokota is called Daisen by *Zellmer et al*. [2012]), and to be 0.5–1.5 wt. % at ~2.0 GPa by *Iwamori* [1992]. Our estimates are 0.5–2.5 wt. % (Figure 17e), almost consistent with these other thermodynamic and experimental approaches. The values are similar to those for basalts in the N. Izu rear arc (0.9–1.3 wt. %) [*Kimura et al*., 2010] despite lower degrees of mantle melting in SW Japan ($F = 1–4$ %) than in N. Izu (2–15%), which is consistent with a drier slab flux in SW Japan (see discussions in above section 6.6.4).

ABS4 predicts that HMA magma has relatively high $H_2O = 3.0–5.5$ wt. % (Figure 17e) at [T] = 1190–1280°C and [P] = 1.6–2.2 GPa (Figure 17a). Experiments show that H_2O-undersaturated HMA melts with 5–8 wt. % H_2O equilibrate with harzburgite to lherzolite residues at $T = 1100–1280°C$ and $P = \sim 1$ GPa [*Tatsumi and Eggins*, 1995]. Therefore, the ABS4 parameters are reasonable for mantle melting reactions with a lherzorite residue (Figure 15).

The high calculated water content in Daisen AA/ADK and Aono ADK (3–5.5 wt. %) is consistent with the occurrence of hornblende in these lavas. All ADK lavas contain hornblende crystals which crystallized from adakite melts (see sections 5.1 and 6.1.1) and hornblende is a phase in andesite-dacite melts with >5 wt.

% H_2O [*Almeev et al*., 2013a, 2013b; *Grove and Kinzler*, 1986; *Merzbacher and Eggler*, 1984; *Sisson and Grove*, 1993].

6.6.6. Slab Flux Sources [Fliq(SED)], [Fliq(AOC)]

Three separate slab liquid fractions are calculated in ABS4: [Fliq(SED)], [Fliq(AOC)], and [Fliq(DMM)]. For the P-T path in and just above the slab in the Nankai subduction zone, [Fliq(SED)] and [Fliq(AOC)] are hydrous silicate melts in the pressure range 2.8–6.0 GPa, whereas [Fliq(DMM)] is a hydrous fluid (supporting information 8). [Fliq(DMM)] is not discussed further for reasons given in section 6.6.1. Figure 17f shows the relationship between the SED:AOC proportion in the slab source and the water content of the resulting slab melt. H_2O contents increase with increasing [Fliq(SED)] in ABS4 because H_2O from deeper AOC layers accumulates in the overlying sediment layer.

Successful ABS4 models require the highest proportion of AOC in the slab source for Abu SHO (0.79–0.95 AOC mass fraction), followed by Aono ADK (0.60–0.80 AOC). Models for Abu SAB, Abu HMA, Yokota ABL/ABH, and Daisen AA/ADK need more sediment in the slab source (0.60–0.90 SED), and Setouchi HMA needs the most (0.98 SED). These source proportions mostly reflect the isotopic composition of the magmas. Setouchi HMA has the most enriched isotopic composition, whereas Abu SHO has the most depleted (see Figures 7 and 14). Slab melt mobility [%R slb] also affects isotopic mixing, but this parameter is relatively uniform in our models.

A large role for subducted sediment in the origin of Setouch HMA in the Miocene has been proposed before [*Shimoda et al*., 1998; *Tatsumi and Hanyu*, 2003] and is confirmed in our model. However, our results show a previously unrecognized spatial relationship in the Quaternary SW Japan arc. Abu SHO and Aono ADK in the west are derived more from AOC requiring deeper melting in the slab, whereas Yokota AB and Daisen AA/ADK in the east and Abu HMA and SAB are more from the overlying sediment. This pattern may reflect subduction of the Kyushu-Palau Ridge (KPR) beneath Abu-Aono (Figure 1a). The northern KPR includes isotopically and trace elementally depleted tonalitic middle crust [*Haraguchi et al*., 2003; *Ishizuka et al*., 2011] and this could account for greater AOC melt production during subduction of the western margin of the Shikoku Basin (see Figure 1a).

6.7. Petrological Summary: Controlling Factors of Arc Magma Genesis

ABS4 models show how various magma suites can form from the same slab and mantle with different intensive/extensive petrogenetic parameters. The key factors for arc magma genesis beneath SW Japan are summarized as follows.

The first-order control on the diversity of the magma suites in SW Japan is the variation in the mass fraction of slab flux added to the mantle. As shown in Figure 17b, the slab flux is largest for AA/ADK (3.5–15 wt. % of mantle mass), intermediate for HMA (1.5–10 wt. %), and lowest for SHO/AB/SAB (0.5–4 wt. %) that are the most like ordinary arc magmas. The amount of slab flux controls the degree of partial melting of the mantle because the addition of water and solutes reduces the mantle solidus (Figure 17c). Although mantle temperature also controls the degree of melting of the mantle (Figure 17a) and compensates to some extent for the increase in degree of mantle melting by large slab flux additions (Figures 17b–17d), the mass fraction of slab flux has the most fundamental control on magma type.

Mantle melting is deepest for SHO/AB/SAB, intermediate for Abu HMA, and shallowest for AA/ADK (Figure 17a). Small amounts of slab melt react immediately with the ambient mantle at a greater depth to form SHO/AB/SAB. The melting temperature is higher for these suites because the pressure is greater, and less water and silica are added to the mantle by less flux. In contrast, when there is a large mass fraction of slab flux, it can reach shallower depths because of its buoyancy and because it reacts less with surrounding mantle due to the higher liquid/rock ratio [*Tsuchiya et al*., 2005]. The lower mantle melting temperature in AA/ADK also reflects the lower temperature of the slab melt which cools the mantle wedge.

The second-order control of the geochemical variation between suites is the proportion of sediment versus AOC in the slab melt source. The sediment component is most prominent in Setouchi HMA, followed by Abu SAB, Abu HMA, Yokota ABL/ABH, and Daisen AA/ADK, with the least in Aono ADK and Abu SHO (Figure 17f). This proportion affects H_2O contents in the peridotite and primary magma (Figure 17f) and is a function of the isotopic composition of the magma suite (Figures 7 and 14). The proportion of slab melt from AOC is greatest where the extinct spreading center (the Palau Kyushu Ridge) is subducting (section 6.6.7).

6.8. Subarc Processes Beneath Hot Subduction Zones

We next compare the intensive/extensive variables in our ABS4 models to seismic tomography results in order to examine the relationships between geochemistry and geophysics.

6.8.1. Mantle Tomography and Seismicity

Using the latest estimates of the Moho and the surface of the Philippine Sea Plate depths [*Katsumata*, 2010; *Nakajima and Hasegawa*, 2007; *Zhao et al*., 2012] (Figure 2a), we present two new crust-mantle cross sections (Lines A and B in Figure 1b). The corresponding Vp/Vs velocity structures are shown in Figure 18 which also includes dehydration/melting profiles from ABS4 for five representative slab layers (MwP, SED, UBAS = AOC, LGAB, SlbP) using the geodynamic model of *Syracuse et al*. [2010] and *van Keken et al*. [2011] modified slightly by P. E. van Keken (personal communication, 2011).

Key features of Figure 18 include the following. The subduction angle of the slab is shallow (10–30°). Slab seismicity extends to ~80 km and is most frequent at ~40–50 km [*Nakajima and Hasegawa*, 2007]. The deeper slab is aseismic but is imaged by tomography to extend to >270 km at a steeper angle (>50°) [*Zhao et al*., 2012]. Low-frequency tremor occurs between 35 and 40 km [*Katsumata and Kamaya*, 2003; *Obara*, 2002], roughly corresponds to the location of the slab-mantle-crust triple junction and is associated with a high Vp/Vs region in the uppermost slab. The wedge mantle beneath the fore arc always has high Vp/Vs (Figure 18c).

6.8.2. Slab Dehydration and Melting

The Perple_X-based petrogenetic grids used in ABS4 (supporting information 8) provide the water release and melting profiles of the slab in the Nankai Subduction Zone that are shown in Figures 18a and 18b. Two loci of fluid release from the slab are predicted. The first at depths shallower than 80 km is gradual and corresponds to the breakdown of serpentine minerals in MwP/SlbP and the breakdown of zoisite in SED/AOC/GAB (the blueschist to hydrous eclogite transformation). This results in high Vp/Vs in the corner of the mantle wedge that is a distinctive characteristic of SW Japan and other hot subduction zones [*Hyndman and Peacock*, 2003; *Nakajima and Hasegawa*, 2007]. The second at 80–90 km corresponds to the breakdown of chlorite in MwP/SlbP and amphibole and lawsonite in SED/AOC/GAB (the hydrous eclogite to dry eclogite transformation) [*Hacker et al*., 2003; *Kita et al*., 2006; *Omori et al*., 2009]. It reflects slab melting with total breakdown of most hydrous minerals in all slab layers resulting in an almost anhydrous residual slab apart from phengite in metasediment (Figures 18a and 18b).

The released fluids hydrate the overlying mantle wedge and form high Vp/Vs serpentinized mantle beneath the fore arc (Figures 18c and 18d). Hot springs occur in the SW Japan fore-arc and intraarc regions, many of which have mantle-type $^3He/^4He$ isotope ratios [*Sano et al*., 2009]. This may reflect interaction between slab-derived fluids and mantle wedge peridotite that scavenges ^3He from the mantle [*Sano et al*., 2009]. Serpentinized mantle and high $^3He/^4He$ hot springs also characterize the fore arc of the Cascadia hot subduction system [*Hyndman and Peacock*, 2003]. These features reflect the shallow dehydration of the slab. In contrast, there are few hot springs in the NE Japan fore arc and none of them has mantle-type $^3He/^4He$ isotope ratios. Neither is there evidence of extensive serpentine in the fore-arc mantle based on seismic velocities there [*Tsuji et al*., 2008].

ABS4 also predicts slab melting after transformation to dry eclogite at ~80 km (Figure 18b). The onset of melting in ABS4 corresponds to the seismic-aseismic transition of the slab at 2.6 GPa (~85 km) and 670°C (Figures 18c and 18d). This correlation has been pointed out before and has been interpreted as evidence of slab melting beneath SW Japan [*Kimura et al*., 2005a; *Morris*, 1995; *Peacock and Wang*, 1999]. Our combination of seismic observations and ABS4 models confirm that 20–35% of slab melting is followed by near-vertical ascent of the melt (Figures 18c and 18d).

6.8.3. Mantle Convection

If there is extensive shallow dehydration of the slab in hot subduction zones, why is not there magmatism closer to the trench? The answer may be a lower mantle temperature in the fore arc. We infer that the wedge mantle beneath the SW Japan fore arc is too thin to yield much melt, the mechanical coupling at the slab-mantle interface beneath the fore arc is too weak to drag down the overriding mantle peridotite, and these two conditions limit how far hot mantle can advect from the rear arc toward the trench. In effect, the shallow subduction angle, the hot and buoyant slab [*van Keken et al*., 2002], and the weak wet mantle beneath fore arc [*Katayama et al*., 2012] prevent hot mantle from going closer to the plate boundary. HMA

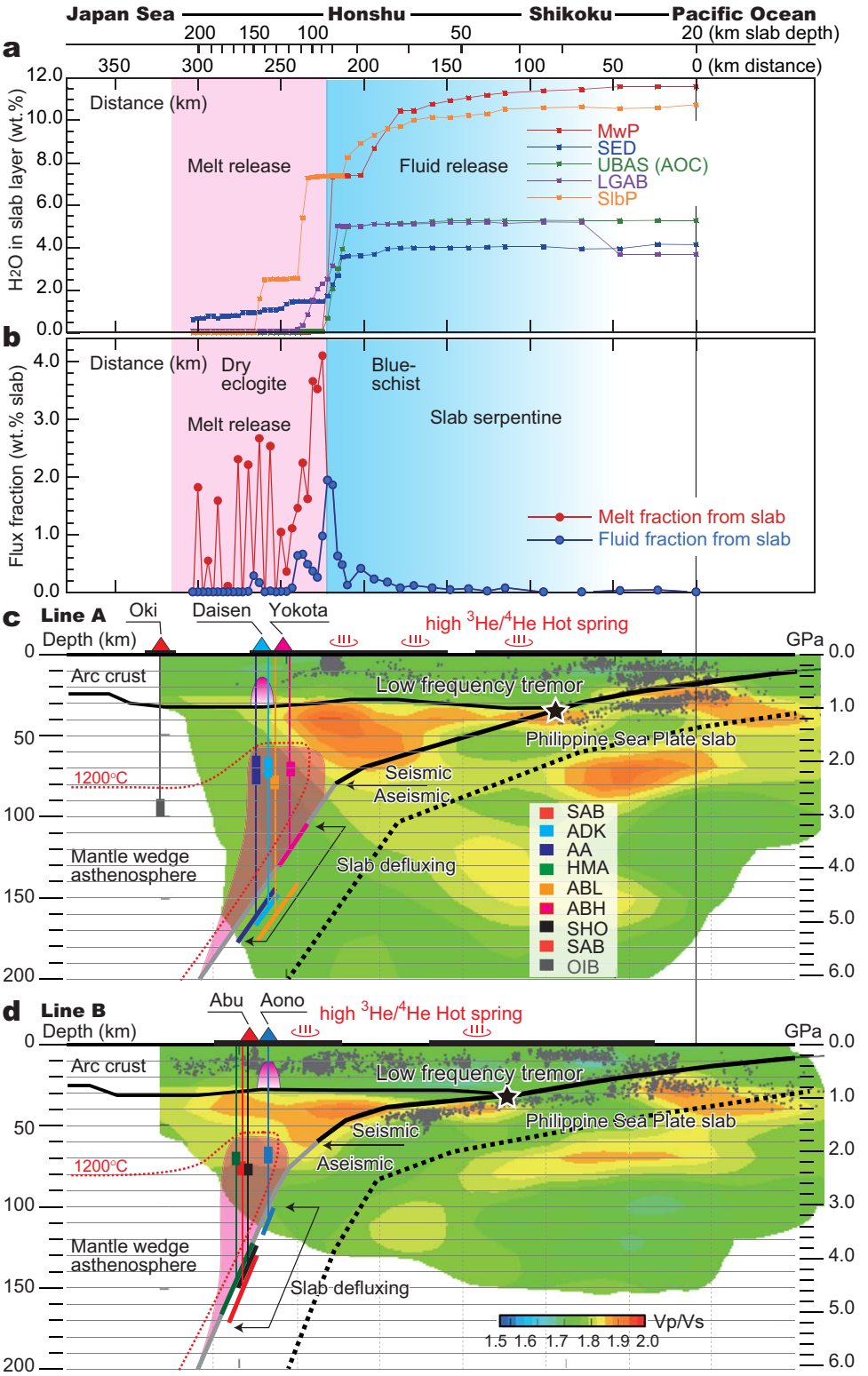

Figure 18. Depths of slab and mantle melting calculated by ABS4 compared to the Vp/Vs structure of the SW Japan arc from *Nakajima and Hasegawa* [2007] updated for this paper. The location of the slab is from *Nakajima and Hasegawa* [2007] for its seismic portion, and from *Zhao et al.* [2012] for its aseismic portion. (a) Dehydration profile of slab layers. (b) Slab fluid and melt fractions (in wt. %) calculated along the Nankai thermal profile assuming the dynamic model of *Syracuse et al.* [2010]. (c and d) The depth of melting in both the slab and overlying mantle in our models. A different color is used for each magma suite. The locations of the two cross sections are shown as Lines A and B in Figure 1. The depth of slab melting in our model coincides with the aseismic portion of the slab.

and ADK come from the coldest mantle with, therefore, the lowest mantle melting productivity. Ironically, the most distinctive magmas of the hottest subduction zones come from the coldest mantle.

ABS4 predicts that the slab will melt at 85–160 km (Figures 18c and 18d) and that final equilibration during flux melting of the mantle will occur at 60–80 km (Figures 18c and 18d). The OIB suites in SW Japan equilibrated with garnet peridotite at >70 km (section 6.2.3) and are isotopically similar over 200 km between OIBL at Kannabe and OIB at Abu. Therefore, the mantle at >70 km should be well-mixed asthenosphere rather than lithosphere (see 1200°C isotherm in Figures 18c and 18d). Convection could be passively induced by coupling to the slab deeper than ~80 km [*van Keken et al*., 2002], or actively induced by the buoyancy of slab melts [*Behn et al*., 2011]. This is beyond the scope of this paper and should be examined by geophysical observations or geodynamic models.

6.9. Key Factors of Arc Magma Genesis: Hot Versus Cold Arcs

The hot subduction system in SW Japan is a global end-member and, therefore, a key to understanding the origin of arc magma suites globally including calc-alkaline basalt, shoshonite, high-Mg andesite, and adakite, alone and in combinations [*Feineman et al*., 2013; *Kimura et al*., 2005a; *Morris*, 1995; *Peacock and Wang*, 1999; *Tatsumi and Hanyu*, 2003]. Alternative views have been proposed for the origin of adakite in SW Japan [*Zellmer et al*., 2012], but our more comprehensive data set and integrative models support the traditional explanation that emphasizes a large role for slab melting rather than adakite origin from the lithospheric mantle or lower crust. However [*Zellmer et al*., 2012], estimate of lower water contents in basalts from hot SW Japan (1.5–2.5 wt. %) than in colder Kyushu volcanic front basalts (3.5–6.0 wt. %) is consistent with our models that estimate 5–8 wt. % H_2O in basalts from the cold N. Izu volcanic front [*Kimura et al*., 2010] versus 1.5–2.5 wt. % in AB/SHO/SAB from hot SW Japan which is similar to that in rear arc basalts from N. Izu.

Although models like ABS that use the geodynamic models of *Syracuse et al*. [2010] and *van Keken et al*. [2011] predict slab melting in most arcs (e.g., N. Izu rear arc) [*Kimura et al*., 2010], the erupted magmas usually are only medium-K to high-K subalkalic arc basalt (SAB) and lack the diversity found in the SW Japan arc. SAB in SW Japan is similar to the medium to high-K rear arc SAB in colder subduction zones like N. Izu. SHO also occur in atypical environments in cold subduction zones such as the Quaternary shoshonites in the northern Mariana arc [*Sun et al*., 1998]. SHO and SAB magmas are both characterized by a relatively low slab-melt flux and by mantle melting in the garnet peridotite stability field (Figures 17a and 17b). This, therefore, is the norm for arcs globally, as shown by the similarity between melting relationships for SW Japan SHO/SAB and basalts at the Mariana volcanic front in Figure 17c.

High degrees of mantle melting characterizes the volcanic front of colder subduction zones. This is attributable to the large H_2O flux from the slab at the hydrous to dry-eclogite transformation, as suggested by ABS3 analyses for N. Izu [*Kimura et al*., 2010]. In contrast, the H_2O-poor slab melts dominate beneath the hot SW Japan arc instead of H_2O-rich fluids, and there is less mantle convection beneath the arc (section 6.8.3). This combination of dry flux and cold mantle is the reason for the lower magma productivity in SW Japan [*Kimura et al*., 2005a] than in colder subduction zones such as NE Japan.

The presence or absence of particular magma suite(s) and their relative amounts primarily depend on the thermal structure of the slab and the mantle wedge. If slabs were hotter in ancient subduction zones (e.g., in the Archean), then slab melting and larger volumes of HMA/ADK would result and contribute to continent formation [*Defant and Drummond*, 1990; *Martin et al*., 2005]. Processing of low-K tholeiitic basalt within the crust would account for the development of continental crust later in Earth's history [*Tatsumi et al*., 2008a]. Contrasting magma types between cold and hot subduction zones can be a probe to identify which process was dominant in an arc at any particular place and time in Earth history.

7. Summary

We have newly analyzed 324 Quaternary lavas of SHO, AB, SAB, HMA, AA, and ADK suites from SW Japan and used the geochemical data to investigate the source conditions and materials for magma genesis. We used an improved geochemical mass balance model, ABS4, for the investigation. Our results indicate that all the magma suites can be generated beneath the crust from the same mantle and slab sources by slab melt-fluxed mantle melting that is induced by subduction of the hot Shikoku Basin. Fundamental

controlling factors of the heterogeneous magma genesis are (1) the mass fraction of slab melt, (2) the relative proportion of AOC and SED sources in the slab, and (3) the P-T conditions of mantle melting.

The basaltic SHO/SAB/AB suites were derived from the deepest and hottest mantle with the addition of 0.5–4% slab-melt flux, which is within the range of arcs globally. In contrast, the more unusual HMA and ADK suites originated from shallower and cooler mantle with the addition of 1.5–10% and 3.5–15% slab-melt flux, respectively. The higher slab melt fractions result in more Si-rich parental magmas. The total melt production (slab plus mantle melting) is surprisingly similar for all suites relative to the water content of the mantle because the degree of interaction between the mantle and slab melt decreases as the mass fraction of slab melt increases. The most distinctive magma suites of hot subduction zones come from atypically cold mantle.

Other key conclusions about the hot SW Japan subduction zone are as follows. The percent of slab melting is high (32–37%) but the percent of mantle melting is low (<5%). The mantle is less depleted than beneath NE Japan and Izu despite lying in front of the Japan Sea back-arc basin. The amount of melted AOC versus sediment from the slab is greatest above the site of subducting an extinct spreading ridge, the Palau Kyushu Ridge. Unlike colder arcs, there is no need to invoke melting of the base of the mantle wedge, perhaps because its coupling to the slab is too weak. We predict relatively low water contents of 0.5–2.5 wt.% in the primitive parental magmas of the basaltic suites, versus 3–6 wt. % for the HMA and adakite suites.

Our results are internally consistent with the major and trace element and Sr-Nd-Hf-Pb isotopic composition of the least crustally contaminated parental magmas. Our results are specific about the slab and mantle source compositions, slab dehydration and melting conditions, and the residual slab and mantle mineralogy. These in turn are consistent with seismic tomography images and seismic profiles for the SW Japan arc. The results show that the ABS4 petrogenetic model is a powerful tool for constraining the geochemical and geophysical processes occurring beneath arcs.

Appendix A: Deep Fractional Crystallization for AA/ADK

Supporting information 4 gives details about the mass balance calculations to test whether Yokota basalt can differentiate to Daisen adakite via high pressure closed (FC) or open system (AFC) processes. Because there are no garnet crystals in either Yokota AB or Daisen AA/ADK, we used garnet compositions from experiments at ~1 GPa for basalt and andesite [*Alonso-Perez et al*., 2009; *Müntener et al*., 2001]. The basalt composition used by *Müntener et al*. [2001] and the andesite compositions used by *Alonso-Perez et al*. [2009] are similar to Yokota AB and Daisen AAs/ADK (supporting information 4 and Figures 10a and 11c).

The experimental mineral compositions are plotted on CaO-SiO_2 and Al_2O_3-SiO_2 diagrams together with the melt, olivine, and clinopyroxene compositions from Yokota AB and melt, orthopyroxene, hornblende, and plagioclase compositions from Daisen AA/ADK (Figures 10a and 11c). The observed mineral compositions in the natural lavas agree well with the experimental run products. The experimental garnet composition (Figures 10a and 11c), clinopyroxene, olivine, hornblende, and plagioclase compositions used for the calculations are given in supporting information 4 and shown by stars in Figure 10.

The mass balance calculations converged with $r^2 = 0.999$ for AA when Gar = −0.140, Amp = −0.530, Plag = −0.023, Ol = +0.043, Cpx = +0.055, and for ADK when Gar = −0.176, Amp = −0.592, Plag = −0.036, Ol = +0.066, Cpx = +0.052 (supporting information 4 and Figure 10a). Fractionation of large amounts of garnet and amphibole are accompanied by the subtraction of a few percent plagioclase and addition of a few percent clinopyroxene and olivine. Petrologically, the mass balance is consistent with simple fractional crystallization plus some internal mixing between the fractionated and parent basalts [*Almeev et al*., 2013a; *Sakuyama*, 1984].

We also tested an alternative model including assimilation of a crustal melt. The major element composition of the crustal melt was assumed to be the average from the sediment melting experiments compiled by *Kimura and Yoshida* [2006] (supporting information 4 and Figures 10a and 11c). The results showed that the calculations converge with $r^2 = 0.999$ for AA when Gar = −0.073, Amp = −0.297, Plag = +0.107, Crustal melt = +0.267, and for ADK when Gar = −0.026, Amp = −0.144, Plag = +0.136, Crustal melt = +0.494 (supporting information 4 and Figure 10c). The mass balance result requires about half as much crustal melt

addition as crystallization for AA and even more for ADK, plus addition of plagioclase together with subtraction of amphibole and trace garnet. This is also petrologically feasible if crustal melting remobilized plagioclase and added it to the daughter magma.

The two mass balance calculations appear to be feasible for major elements. In the next step, we calculated trace element compositions for the two models using appropriate partition coefficients. D(Gar) was calculated using the *Draper and van Westrenen* [2007] model with the Py52 garnet major element composition of *Alonso-Perez et al*. [2009], the average Yokota AB composition, $P = 1.0$ GPa, and $T = 1200^{\circ}$C. D(Cpx) was calculated using the *Wood and Blundy* [1997] model and the same conditions. *D*(Amp) was basically from *Pilet et al*. [2011] with modifications as shown in Figure 9. D(Plag) was calculated using the *Bindeman* [2007] and *Bindeman et al*. [1998] model for An_{52} and $T = 1100^{\circ}$C. The trace element composition of the crustal melt was estimated from the hornblende rims in a Daisen ADK (see Figure 9 and supporting information 3). All the melt and mineral compositions are listed in supporting information 4.

The calculated trace elements results agree poorly despite good matches for the major elements. The fractional crystallization model resulted in strong depletions and a good match in HREE but greater enrichments than observed in all other elements (supporting information 4 and Figure 10b).

The assimilation fractional crystallization model also failed because the fractionation of hornblende and garnet was compensated by the addition of crustal melt and plagioclase that resulted in almost no change in trace element abundances (Figure 10d). Large amounts of crustal contaminants for the adakitic andesite source are also not feasible because the least radiogenic AA/ADK has less radiogenic Pb than any of the Yokota ABs (Figure 8d).

Appendix B: Primary Basalt Estimates for SHO, AB, and SAB

B1. Fractionation Correction

For each of these basaltic suites, we first estimated several parental basalt compositions as summarized in section 6. These are given in supporting information 5. However, because these have only 4.6–10 wt. % MgO, whereas ABS models primary mantle melts, it is necessary to correct the parental basalts for crystal fractionation. This is notoriously difficult because the fractionating mineral assemblage depends heavily on bulk composition and especially water contents. In the case of SW Japan basalts (including Yokota AB and Abu SAB), H_2O contents estimated using the olivine-plagioclase geohygrometer are <2 wt. % at 1 GPa and lower than in northern Kyushu volcanic front basalts ($\sim$5 wt. % at 1 GPa) [*Zellmer et al*., 2012]. The estimated H_2O contents are noticeably lower than in the low-K to medium-K basalts in other arcs [e.g., *Plank et al*., 2013]. Therefore, for simplicity we assumed dry conditions for estimating fractional crystallization corrections.

A pyroxenite source is possible [*Straub et al*., 2008]. Phase relationships for deep peridotite and pyroxenite melting have been examined by *Herzberg* [2011] who formulated peridotite and pyroxenite cotectics in CMAS plots of CaTs-Ol-Qz (from Di) and Py(A)-Di(CS)-En(MS) (from Ol). This allows us to calculate the amount of olivine that needs to be added to form a primary basalt. CMAS plots are especially useful for estimating the residual mantle mineralogy for both peridotite and pyroxenite lithologies in the garnet stability field (>2 GPa). This is appropriate for the sources of alkaline OIB/AB/SHO in which residual garnet is suggested by the depleted HREE patterns (Figure 6). SAB in Abu is subalkaline but also has a residual garnet signature (Figure 6) and is intermediate between OIB and arc magma. Therefore, we used the same back-calculation procedure for all the basalt suite magmas.

Clinopyroxene is the most ubiquitous phenocryst in most of the basalt suite lavas. The effect of clinopyroxene fractionation can be examined using CaO/Al_2O_3 versus MgO plots [*Sisson et al*., 2009]. Most of the OIB/AB/SAB suite lavas show a monotonous decrease in CaO/Al_2O_3 when MgO is <7 wt. % (not shown, see supporting information 2), indicating clinopyroxene fractionation. Therefore, we added equilibrated clinopyroxene stepwise to each parental basalt until the MgO content reached 7 wt. % (the black arrow in Figure 11a). This required the addition of up to 16% clinopyroxene. The equilibrated clinopyroxene compositions were calculated using the method in Appendix of *Wood and Blundy* [1997].

Then, the clinopyroxene fractionation-corrected compositions were adjusted by adding equilibrated olivine until the magma compositions reached the cotectic in the CaTs-Ol-Qz diagram (Figure 11b) at the pressure

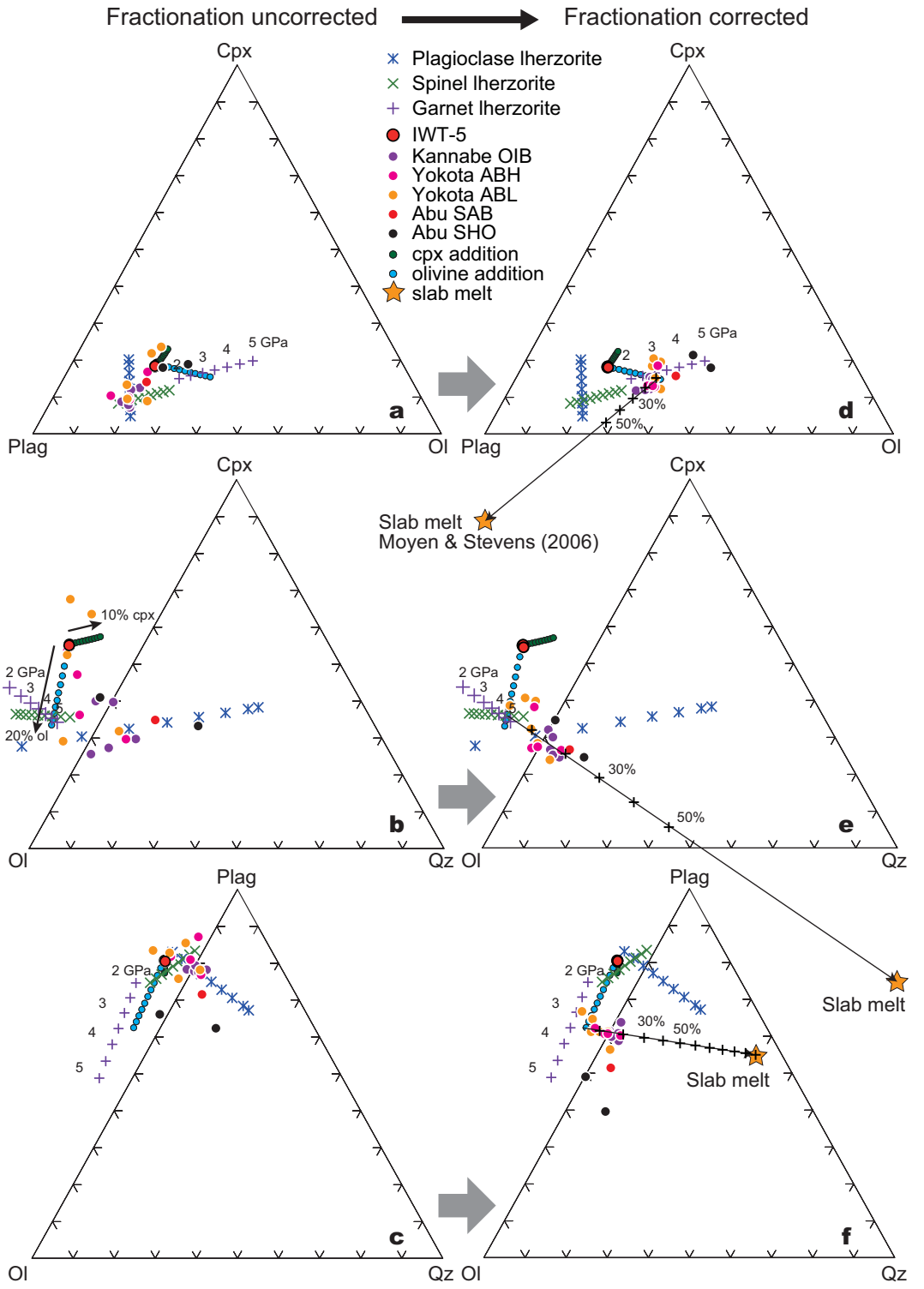

Figure A1. Pseudo-ternary projections showing the results of an experimentally calibrated method for calculating the multiple saturation points for plagioclase (blue stars), spinel (green x's), and garnet (purple +'s) lherzolite sources at various pressures from 2 to 5 GPa [*Grove et al.*, 2013; *Till et al.*, 2012a]. We use the relatively primary magma IWT-5 to calculate the multiple saturation points. (a–c) Fractionation uncorrected OIB, ABH, ABL, SAB, and SHO compositions (supporting information 1). (d–f) Fractionation corrected compositions (supporting information 5). Also shown are trends of clinopyroxene (green filled circles: cpx) and olivine (blue filled circles: ol) addition for up to 10 wt. % and 20 wt. %, respectively. Orange stars connected to a black line with tick marks show mixing between mantle melts and slab melt (orange star) in wt. % slab melt. The slab melt composition is from *Moyen and Stevens* [2006].

that is indicated by its location in the Py(A)-Di(CS)-En(MS) plot of *Herzberg* [2011] (Figure 11c). The open symbols in Figures 11a and 12b show this olivine addition in 1 wt. % increments. (The mantle equilibration pressure can be estimated using the Py(A)-Di(CS)-En(MS) plot (Figure 11c) because it is unaffected by Ol composition.) The equilibrated olivine compositions are calculated using the PLIMELT2 package [*Herzberg and Asimow*, 2008] which was linked with the CMAS back calculations.

Note that the total amount of clinopyroxene and olivine added to the basalts is almost identical with that by the PLIMELT2 olivine maximum fractionation model [*Herzberg and Asimow*, 2008]. The calculated incompatible trace element compositions are almost identical by the two methods. Therefore, the difference in back-calculation approach has little effect on ABS4 results.

B2. Evaluation of the Correction Method

We tested the validity of our fractionation correction calculations using modeled phase equilibria for plagioclase (Pl), spinel (Sp), and garnet (Gt) lherzolite [*Grove et al*., 2013; *Till et al*., 2012a]. Figure A1 shows the pseudo-ternary plots of fractionation uncorrected and corrected basalt compositions for ABH, ABL, SAB, and SHO from supporting informations 1 and 5. We used the relatively primitive IWT-5 sample (MgO = 10.10 wt. %) to calculate the multiple saturation points for each lithology at various pressures. We also calculated trends of 10% clinopyroxene fractionation and 20% olivine fractionation using the same scheme noted above. The fractionation-uncorrected samples plot around the plagioclase to spinel lherzorite fields with wide scatter.

In contrast, the fractionation-corrected ABH, ABL, and SAB compositions plot more tightly around the 2–3 GPa garnet lherzolite multiple saturation points in the Plag-Cpx-Ol (Qz) pseudo-ternary system (Figure A1d), as does the SHO composition at 5 GPa. These show coherent results with CaTs-Ol-Qz plots in Figure 11b apart from SHO that has extremely high alkalis and may not be from a typical lherzolite source [*Tatsumi and Koyaguchi*, 1989]. Extremely enriched K reduces Plag component in the pseudo-ternary plot. Thus, the erroneously high P given by the plot would originate from this.

The corrected compositions are systematically offset from the garnet lherzorite multiple saturation points toward Qz apex on both Ol-Cpx-Qz(Plag) and Ol-Plag-Qz(Cpx) plots (Figures A1c and A1d). Mixing with ~20 wt. % of slab melt (represented by averaged experimental slab AOC-SED melt compositions [*Kimura et al*., 2010; *Moyen*, 2009]) explains the shifts in both the pseudo-ternary systems. Note that the Plag-Cpx-Ol(Qz) plot less affected by the slab melt mixing because it is projected from Qtz. Mixing with the slab melt (Figures A1e and A1f) is supported by our ABS4 models as discussed in section 6.5.5.

The agreement between our fractionation corrected compositions and the garnet lherzolite multiple saturation points of *Grove et al*. [2013] and *Till et al*. [2012a] indicates that our fractionation correction method is reasonable. Errors in the multiple saturation points are about 10% in the pseudo-ternary spaces for garnet lherzolite [*Grove et al*., 2013] (see 10% additions for olivine and cpx in Figure A1 as an example of scale). Therefore, the scatter in the corrected SW Japan primary basalt compositions is almost within error (Figure A1d). Errors from the fractionation correction will propagate in the ABS4 mass balance calculations and thus the calculated intensive and extensive parameters. Our models accept a 20% mismatch of REE abundances between calculated and observed target compositions. Therefore, a 10% error in fractionation correction has little effect on our method [see details for ABS4 in Appendix C and *Kimura et al*., 2010].

Appendix C: ABS 4 Model

The first ABS model was applied to the cold NE Japan arc so that it considered only slab dehydration followed by fluid-fluxed mantle melting (ABS2) [*Kimura et al*., 2009]. The option of slab dehydration melting were added later and applied to the cold North Izu subduction zone (ABS3) [*Kimura et al*., 2010]. The additional option of water-saturated slab melting was added in ABS3.1 [*Kimura*, 2012] and applied to a low-Ca boninite and a high-Mg adakite in the infant IBM arc [*Li et al*., 2013].

We have now developed ABS4 to better model processes applicable to all subduction zones, and to investigate a wider compositional range of arc magmas including HMA and ADK. The outline of the calculation scheme and improvements in the ABS4 model are briefly described below. An Excel spreadsheet, ARC_BASALT_SIMULATOR_ver.4.00.xlsm is available in supporting information 8 in a zipped folder of the dynamic content.

Table A1. Acronyms Used in ABS4

PERID	Mantle wedge peridotite
MwP	Mantle wedge base peridotite regarded as a part of slab
SED	Sediment layer in slab
AOC	Altered oceanic crust layer in slab
UBAS(= AOC)	Upper basalt layer in slab. The equivalent of altered oceanic crust in ABS3
LBAS	Lower basalt layer in slab
DIKE	Dike layer in slab
UGAB	Upper gabbro layer in slab
LGAB	Lower gabbro layer in slab
SIbP	Peridotite layer in slab
[Slab P(GPa)]	Pressure of slab
[Slab T(C)]	Temperature of slab
[Fliq(SED)]	Slab liquid fraction from SED
[Fliq(AOC)]	Slab liquid fraction from AOC
[Fliq(DMM)]	Slab liquid fraction from mantle wedge base peridotite
[%R slab]	Reaction factor of slab liquid in the slab. More diffused flow when small
[n(PERID)]	Zone refining reaction factor [not used in this study, see *Kimura et al*., 2009]
[%MORBext.]	PERID predepletion factor expressed by wt. % MORB melt extracted
[P](GPa)	Mantle wedge PERID pressure
[T](C)	Mantle wedge PERID temperature
[F](PERID)	Degree of melting of PERID
[Fslb liq.%]	Fraction of slab liquid in PERID at wt. % fraction of mantle mass
[β%]	Beta factor in open system melting of *Ozawa and Shimizu* [1995] shown by wt. % of mantle mass

A word of caution is appropriate. ABS4 is complicated because arc magma genesis is complicated. Forward modeling requires a current-best-guess about many processes and parameters, and thousands of papers provide suigeneric forward models to explain certain element or isotope compositions of arc magma outputs by varying certain inputs or melting processes. ABS4 provides the user with many such state-of-art quantitative tools covering most but not all of the key processes and variables. Each tool involves choices, and they are explained below. By making ABS4 freely available, it is our hope that it is a step toward a "community arc magma genesis model" like those used to explore another complex system, climate change.

C1. Source Materials and Subduction Slab Structure

Source materials for subduction zone magmas used in the ABS4 model are: slab materials from bottom to top including slab peridotite beneath subducting oceanic crust (SIbP); lower and upper gabbro (oceanic layer 3: LGAB and UGAB); dikes (oceanic layer 2: DIKE); two basalt layers (LBAS/UBAS); sediments (SED); the metasomatized base of the overlying mantle wedge (MwP); and the overlying mantle wedge itself (PERID) (see also Table A1). We and others refer to oceanic layers 2 and 3 together as Altered Oceanic Crust (AOC). ABS2/3 used a single P-T path profile at the slab surface for to calculate the prograde metamorphic reactions of AOC, SED, and MwP [*Kimura et al*., 2009]. Because of the significant thermal gradient across the subducted oceanic plate, P-T paths at the surface and at the Moho depth of the subducted plate greatly differ [*van Keken et al*., 2011]. Therefore, ABS4 calculates these metamorphic reactions along separate P–T paths for eight layers (SIbP, LGAB, UGAB, DIKE, LBAS, UBAS, SED, and MwP) using the self-consistent geodynamic model for 56 subduction zones from [*Syracuse et al*., 2010; *van Keken et al*., 2011]. This approach captures and integrates the effects of dehydration in the lower layers but melting closer to the slab surface. That is, it can add slab fluids to slab melts.

C2. Slab Dehydration/Melting Model

The composition of fluids or melts that are released from each layer during prograde metamorphism along its P-T path are calculated in all versions of ABS using the residual mineralogy and partition coefficients between the minerals and melts or fluids. The subsolidus metamorphic mineral assemblage for each layer was calculated using the Perple_X ver. 7 thermodynamic model [*Connolly and Kerrick*, 1987; *Connolly and Petrini*, 2002]. The super-solidus regions are based on the water-saturated and undersatured experimental results for AOC and SED of *Hermann and Spandler* [2008], *Schmidt et al*. [2004], and *Skora and Blundy* [2010]. ABS4 uses the same solidi for both SED and AOC, but different percent melting in P-T space based on the experimental results. Fixed major element compositions of slab SED (pelagic sediment), AOC (MORB basalt), and MwP (depleted MORB source mantle: DMM) were used for Perple_X calculations as also done by *Hacker* [2008]. The same AOC composition was used for UBAS, LBAS, DIKE, UGAB, and LGAB. The resulting mineral

modes are similar for basalt and gabbro [*Hacker*, 2008]. The troctolite composition used for mafic gabbro by *Hacker* [2008] is not considered. The same petrogenetic grid was used for both SIbP and MwP.

C3. Element Partitioning in the Slab

The maximum bound water in the slab layers was also calculated using Perple_X. Melt fractions above the solidi were based on the experimental studies cited above. Using this information, the program calculates the mass fraction of fluid or melt released from each slab layer along its P-T path. See examples of the representative pseudo-sections for AOC/SED/MwP in Appendix of *Kimura et al*. [2010]. The grids and graphical indications of the slab mineralogy and dehydration/melting profiles are in the [SIb_Mode] Worksheet in the ABS4 Excel spreadsheet (supporting information 8).

Partition coefficients used for to calculate the chemical composition of the released slab fluids/melts and residual solids in the slab layers are the same with those used in *Kimura et al*. [2010]. They are temperature dependent Ds for D(Cpx), D(Opx), D(Amp), and D(Gar), and fixed Ds for other minerals. The partition coefficients are in ABS4 Worksheet [SDMS4.0].

C4. Element Behavior in the Slab

In previous ABS versions, interaction between slab liquids and overlying slab layers was only considered for the MwP layer [*Kimura et al*., 2009]. With the increased number of slab layers from three (ABS2/3) to eight (ABS4), there is more interaction within a 1-D vertical column. In ABS4, all the dehydration/melting reactions are treated as incremental batch calculations [*Shaw*, 2000] as shown in Figure A2.

With the calculations, the fraction of melt or dehydrated fluid in any cell (area in P-T space) is treated as F, and the additional fluid or melt fraction that is lost from the underlying cell in the 1-D column (F_{x-1}) is incrementally added to the overlying cell. Precipitation of minerals or increase in F due to the additional liquids is not considered either in the phase changes of the solids or changes in F in the cells. However, the composition of the liquid and solid in each cell changes because of the addition, which results in considerable change in both trace element abundances and isotopic compositions. Isotopic compositions are calculated using a computational solution that calculates isotopic abundances based on the isotope ratios. H_2O is treated as an incompatible element using $D(H_2O) = D(Ce) = 0.01$ [*Plank et al*., 2009]. This is also applied to slab melting and H_2O contents in the slab melts are calculated by XH_2O/Xslab melt.

The interaction between ascending slab liquids and their surroundings depends not only on the degree of dehydration or melting, but also the nature of fluid flow (porous flow or fracture flow: [*Bebout*, 2007]). The differences in flow type cause different degrees of element redistribution [*Iwamori*, 1992]. We model this by using the [%R slab] factor to modify the F parameter in the batch dehydration/melting/reaction calculations (see supporting information 8). This factor alters all F used in the calculation matrix as $[F'_{x.x}] = [F_{x.x}] \times$ [%R slab]/100. It can be varied from 0 (no slab liquid movement) to several hundred. When [%R slab] = 100, $F_{x.x}$ values equal those determined by the petrogenetic grids. That is, all liquid released from one cell moves to the one above it. When [%R slab] $<$ 100, $F_{x.x}$ is smaller which results in a more effective extraction of elements from the solids. This simulates a reactive porous flow regime. The reverse is true for [%R slab] $>$ 100 that simulates fracture flow. This especially affects isotope ratios because it enhances or dilutes differences between source materials (see supporting information). Therefore, the match for isotope ratios can be improved without much change in element concentrations just by varying the [%R slab] factor. Different [%R slab] factor can be applied to the different slab layers, but we applied the same [%R slab] factor to all layers in this paper.

C5. Slab Fluid/Melt Composition

The calculated element concentrations and isotopic compositions of the resulting slab liquid (fluid or melt or both) are taken separately from the top three layers of UBAS (=AOC), SED, and MwP and then mixed together in proportions defined by the user (Figure A2c). Mixing may occur in a mélange zone at the interface between slab and mantle [*Bebout*, 2007], or higher in the mantle wedge.

C6. Slab Liquid-Mantle Peridotite Reaction

The incompatible trace element and isotopic compositions in the mixed slab liquid is the "flux" for open system melting of the mantle wedge peridotite (PERID). The open system melting calculation model of *Ozawa* [2001] and *Ozawa and Shimizu* [1995] was used along with mantle mineral modes calculated using pMELTS

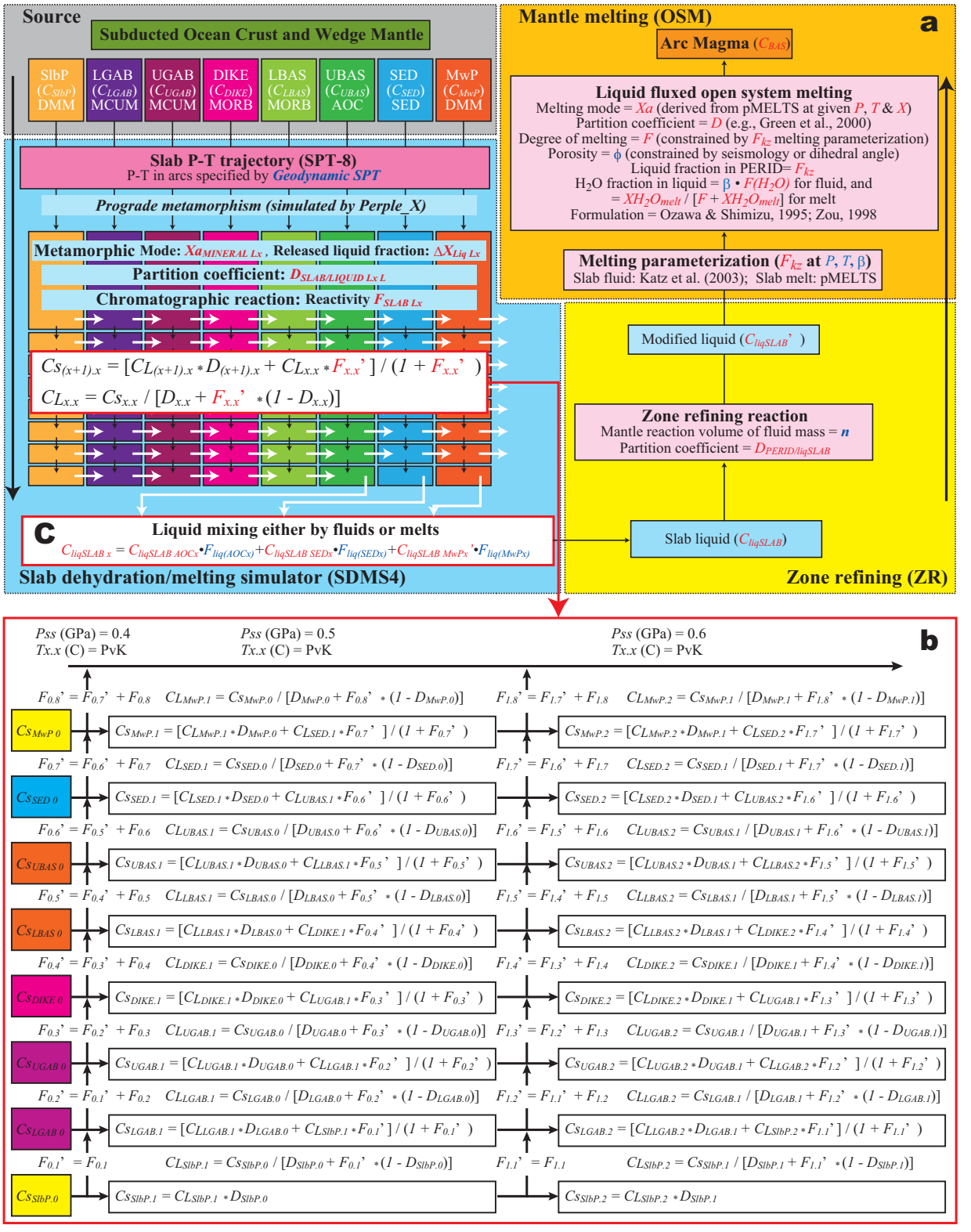

Figure A2. Calculation scheme of (a) ABS4 model with the detailed calculation matrix between slab solids and liquids by (b) incremental batch dehydration/melting/reactions. Note that only a shallow depth range (0.5 and 0.6 GPa) is shown in Figure A2b. See details in Appendix C.

[*Ghiorso et al*., 2002] as parameterized for ABS3/4 [*Kimura et al*., 2010]. The effect of water on the degree of partial melting at a given P-T-XH_2O is from *Katz et al*. [2003].

ABS4 assumes that all the water in the slab fluid/melt is added to the solid mantle to affect the degree of melting of mantle PERID [F]. The relationship between the slab flux [Fslb liq.] and [F] is dealt by the open system melting equation. When the flux is mostly water (i.e., "fluid"), [F] is close to the total melt production. However, when the flux is hydrous silicate melt, the total melt production is [F] + [Fslb liq.] (see section 6.6.4). In reality, the total melt production should vary between [F] and ([F] + [Fslb liq.]) due to the solubility of H_2O from the slab flux in the primary arc magma. The combined melt mass is not calculated directly in ABS4 but the combination is used to calculate the residual slab mantle mineralogy and the major element composition of the primary magma.

ABS4 also treats the extent of depletion of mantle wedge PERID prior to flux melting. This is the user-defined variable [%MORBext.] in the CONTROL_PANEL worksheet (supporting information 8). It is internally consistent for trace elements and isotopes but not for major elements. Mantle mineralogy is considered by reducing cpx in PERID [*Kimura et al*., 2010].

C7. Calculation Parameters and Fitting Strategy

After the target primary magma composition, and the starting compositions of SlbP, AOC, SED, MwP, and PERID are chosen, then the variables of (1) slab flux focusing [%Rslab], (2) flux release depth [Slab P], (3) flux fractions of [Fliq(AOC) – Fliq(SED) – Fliq(DMM)], (4) mantle melting pressure [P], (5) mantle melting temperature [T], (6) slab flux fraction [Fslb liq.%], and (7) PERID depletion [%MORBext.] can be explored simultaneously by using the forward fitting calculations to match the full combination of major, trace, and isotope compositions of the target magma [*Kimura et al*., 2010] (see [CONTROL_PANEL] worksheet in supporting information 8).

Another new feature of ABS4 is the use of Monte Carlo calculations to minimize the calculation time for successful matches. Fitting windows can be adjusted by [% difference] limits from the target magma compositions for LREE, MREE, HREE, Zr-Hf, Nb-Ta, Th, U, Rb, Ba, K, Pb, and Sr. Maximum-minimum value windows also can be set for the calculated SiO_2 and Sr-Nd-Hf-Pb isotope compositions. The fitting windows can reflect analytical uncertainty or the observed variance within the suite of rocks being modeled. A typical example is given in the [CONTROL_PANEL] worksheet in supporting information 8. For example, a "successful match" in this paper means that the composition of the forward-calculated melt agrees with the target composition to within 10–15% for REE and within 3 wt. % for SiO_2, Sr-Nd-Hf isotopes agree better than ± 1 per mil, and Pb isotopes agree better than ± 3 per mil. Use of random number calculations can also prevent pitfalls of artificial correlation derived from petrogenetic constraints.

C8. Errors in the Calculations of Major Elements and Residual Mantle Mineralogy

ABS3 and ABS4 assume a fixed major element composition of the slab melt using an average melt composition from hydrous MORB and sediment melting experiments [*Kimura and Yoshida*, 2006; *Moyen and Stevens*, 2006] (see yellow stars in Figure 14 for the composition). A certain amount of slab melt ([Fslb liq.] up to 30 wt. % of the PERID) with fixed composition is then added to mantle PERID which also has a fixed major element composition represented by DMM of *Workman and Hart* [2005]. The melt composition and residual mantle mineralogy from the modified PERID composition is calculated using pMELTS [*Ghiorso et al*., 2002]. The results were parameterized by *Kimura et al*. [2010] and are given in the [Peri_Mode] and [MJ_pMELTS] worksheets (supporting information 8). After the user specifies the P and T conditions of mantle melting, the degree of melting [F], major element composition of melt, and residual mantle mineralogy are calculated (see [CONTROL_PANEL] of ABS4 in supporting information 8).

The simplifying assumptions of constant slab melt and initial mantle major element compositions limit the application of ABS3/4 for major elements. Even so, the estimates by ABS4 basically reproduce the observed major element variation in the SW Japan magmas. This helps to constrain the conditions of magma genesis as noted in the main text (Figure 14).

Systematic errors in calculated trace elements and isotopes depend largely on the assumed (1) mineral modes in the slab layers and mantle peridotite, (2) partition coefficients, and (3) SED and AOC source compositions. Mass balance fittings are largely controlled by REEs and HFSEs but large errors are always observed in LILEs in this paper (see the text). We attribute the discrepancy to the three factors above.

Because of the multiple sources, statistical treatment of the errors is not possible. Consequently, we have only given the arithmetic average and standard deviation (or minimum-maximum ranges) of successful matches from the Monte Carlo calculations for each target composition.

Acknowledgments

We thank constructive comments from B. Roser at Shimane University. A. Takasu Y. Sawada, and S. Iizumi provided free access to the EPMA, XRF, and TIMS facilities at Shimane University. Discussion of the petrogenetic models with T. Yoshida at Tohoku University, M. Carr and M. Feigenson at Rutgers University, and B. Hacker at University of California Santa Barbara helped to improve the ABS model. Many of these discussions were enabled by NSF grant 0840794 and annual meetings at UCSC. J.-F. Moyen at Université de Lyon kindly provided data compiles of experimental data for slab melting. We also thank detailed and constructive review comments by C. B. Till of U.S. Geological Survey and C.-T. Lee of Rice University. This study was supported by JSPS grant 24340136.

References

Abe, N., and S. Arai (2005), Petrography and geochemistry of the mantle xenoliths: Implications for lithospheric mantle beneath the Japan arcs, *Jpn. Mag. Mineral. Petrol. Sci.*, *34*, 143–158.

Almeev, R. R., J.-I. Kimura, A. A. Ariskin, and A. Y. Ozerov (2013a), Decoding crystal fractionation in calc-alkaline magmas from the Bezymianny Volcano (Kamchatka, Russia) using mineral and bulk rock compositions, *J. Volcanol. Geotherm. Res.*, *263*, 141–171, doi:10.1016/j.jvolgeores.2013.1001.1003.

Almeev, R. R., A. A. Ariskin, J.-I. Kimura, and G. S. Barmina (2013b), The role of polybaric crystallization in genesis of andesitic magmas: Phase equilibria simulations of the Bezymianny volcanic subseries, *J. Volcanol. Geotherm. Energy*, *263*, 182–192, doi:10.1016/j.jvolgeores.2013.1001.1004.

Alonso-Perez, R., O. Müntener, and P. Ulmer (2009), Igneous garnet and amphibole fractionation in the roots of island arcs: Experimental constraints on andesitic liquids, *Contrib. Mineral. Petrol.*, *157*, 541–558.

Ayers, J. C., S. K. Dittmer, and G. D. Layne (1997), Partitioning of elements between peridotite and H_2O at 2.0–3.0 GPa and 900–1100°C, and applications to models of subduction zone processes, *Earth Planet. Sci. Lett.*, *150*, 381–398.

Baker, J., D. Peate, T. Waight, and C. Meyzen (2004), Pb isotopic analysis of standards and samples using a ^{207}Pb-^{204}Pb double spike and thallium to correct for mass bias with a double-focusing MC-ICP-MS, *Chem. Geol.*, *211*, 275–203.

Beard, J. S., and G. E. Lofgren (1991), Dehydration melting and water-saturated melting of basaltic and andesitic greenstones and amphibolites at 1, 3, 6.9 kbar, *J. Petrol.*, *32*, 365–401.

Bebout, G. E. (2007), Metamorphic chemical geodynamics of subduction zones, *Earth Planet. Sci. Lett.*, *260*, 373–393.

Bédard, J. H. (2005), Partitioning coefficients between olivine and silicate melts, *Lithos*, *83*, 394–419.

Behn, M. D., P. B. Kelemen, G. Hirth, B. R. Hacker, and H.-J. Massonne (2011), Diapirs as the source of the sediment signature in arc lavas, *Nat. Geosci.*, *4*, 641–646.

Bindeman, I. N. (2007), Erratum to I. N. Bindeman, A. M. Davis, and M. J. Drake (1998), ''Ion microprobe study of plagioclase-basalt partition experiments at natural concentration levels of trace elements'' Geochimica Cosmochimica Acta 62, 1175–1193, *Geochim. Cosmochim. Acta*, *71*, 2414.

Bindeman, I. N., A. M. Davis, and M. J. Drake (1998), Ion microprobe study of plagioclase-basalt partition experiments at natural concentration levels of trace elements, *Geochim. Cosmochim. Acta*, *62*, 1175–1193.

Brichert-Toft, J., C. Chauvel, and F. Albalède (1997), Separation of Hf and Lu for high-precision isotope analysis of rock samples by magnetic sector-multiple collector ICP-MS, *Contrib. Mineral. Petrol.*, *127*, 248–260.

Bryant, J. A., G. M. Yogodzinski, and T. G. Churikova (2007), Melt-mantle interactions beneath the Kamchatka arc: Evidence from ultramafic xenoliths from Shiveluch volcano, *Geochem. Geophys. Geosyst.*, *8*, Q04007, doi:10.1029/2006GC001443.

Calmus, T., A. Aguillon-Robles, R. C. Maury, H. Bellon, M. Benoit, J. Cotten, J. Bourgois, and F. Michaud (2003), Spatial and temporal evolution of basalts and magnesian andesites (''bajaites'') from Baja California, Mexico: The role of slab melts, *Lithos*, *66*, 77–105.

Castillo, P. R. (2006), An overview of adakite petrogenesis, *Chin. Sci. Bull.*, *51*, 257–268.

Chauvel, C., J.-C. Marini, T. Plank, and J. N. Ludden (2009), Hf-Nd input flux in the Izu-Mariana subduction zone and recycling of subducted material in the mantle, *Geochem. Geophys. Geosyst.*, *10*, Q01001, doi:10.1029/2008GC002101.

Connolly, J. A. D., and D. M. Kerrick (1987), An algorithm and computer program for calculating composition phase diagrams, *Calphad*, *11*, 1–55.

Connolly, J. A. D., and K. Petrini (2002), An automated strategy for calculation of phase diagram sections and retrieval of rock properties as a function of physical conditions, *J. Metamorph. Geol.*, *20*, 697–708.

Defant, M. J., and M. S. Drummond (1990), Derivation of some modern arc magmas by melting of young subducted lithosphere, *Nature*, *347*, 662–665.

Draper, D. S., and W. van Westrenen (2007), Quantifying garnet-melt trace element partitioning using lattice-strain theory: Assessment of statistically significant controls and a new predictive model, *Contrib. Mineral. Petrol.*, *154*, 731–746.

Feineman, M. D., F. J. Ryerson, D. J. DePaolo, and T. Plank (2007), Zoisite-aqueous fluid trace element partitioning with implications for subduction zone fluid composition, *Chem. Geol.*, *239*, 250–265.

Feineman, M. D., T. Moriguchi, T. Yokoyama, S. Terui, and E. Nakamura (2013), Sediment-enriched adakitic magmas from the Daisen volcanic field, Southwest Japan, *Geochem. Geophys. Geosyst.*, *14*, 3009–3031, doi:10.1002/ggge.20176.

Fujibayashi, N., T. Nagao, H. Kagami, M. Iwata, and K. Tazaki (1989), Spatial variation in the Sr and Nd isotope compositions of Cenozoic alkali basalts from the Chugoku district, *J. Mineral. Petrol. Econ. Geol.*, *84*, 429–443.

Furuyama, K., K. Nagao, S. Mitsui, and K. Kasatani (1993a), K-Ar ages of Late Neogene monogenetic volcanoes in the east San-in district, Southwest Japan, *Earth Sci.*, *47*, 519–532.

Furuyama, K., K. Nagao, K. Kasatani, and S. Mitsui (1993b), K-Ar ages of the Kannabe Volcano Group and the adjacent basaltic monogenetic volcanoes, east San-in district, *Earth Sci.*, *47*, 377–390.

Furuyama, K., K. Nagao, and M. Murata (2002), K-Ar ages of andesites from two volcanic arrays in western Chugoku, Southwest Japan, *Bull. Volcanol. Soc. Jpn.*, *47*, 481–487.

Gaetani, G. A., and T. L. Grove (1998), The influence of water on melting of mantle peridotite, *Contrib. Mineral. Petrol.*, *131*, 323–346.

Gazel, E., K. Hoernle, M. J. Carr, C. Herzberg, I. Saginor, P. van den Bogaard, F. Hauff, M. Feigenson, and C. Swisher (2011), Plume-subduction interaction in southern Central America: Mantle upwelling and slab melting, *Lithos*, *121*(1–4), 117–134.

Ghiorso, M. S., M. M. Hirschmann, P. W. Reiners, and V. C. Kress (2002), The pMELTS: A revision of MELTS for improved calculation of phase relations and major element partitioning related to partial melting of the mantle to 3 GPa, *Geochem. Geophys. Geosyst.*, *3*(5), 1030, doi:10.1029/2001GC000217.

Gill, J. B. (1981), *Orogenic Andesites and Plate Tectonics*, 385 pp., Springer, Heidelberg, Germany.

Green, T. H., and J. Adam (2002), Experimentally-determined trace element characteristics of aqueous fluid from partilly dehydrated mafic ocanic crust at 3.0 GPa, 650–700°C, *Eur. J. Mineral.*, *15*, 815–830.

Green, T. H., J. D. Blundy, J. Adam, and G. M. Yaxley (2000), SIMS determination of trace element partition coefficients between garnet, clinopyroxene and hydrous basaltic liquids at 2–7.5 GPa and 1080–1200°C, *Lithos*, *25*, 165–187.

Grove, T. L., and R. J. Kinzler (1986), Petrogenesis of andesites, *Annu. Rev. Earth Planet. Sci.*, *14*, 417–454.
Grove, T. L., N. Chatterjee, S. W. Parman, and E. Médard (2006), The influence of H_2O on mantle melting, *Earth Planet. Sci. Lett.*, *249*, 74–89, doi:10.1016/j.epsl.2006.1006.1043.
Grove, T. L., E. S. Holbig, J. A. Barr, C. B. Till, and M. J. Krawczynski (2013), Melts of garnet lherzolite: Experiments, models and comparison to melts of pyroxenite and carbonated lherzolite, *Contrib. Mineral. Petrol.*, *166*, 887–910.
Hacker, B. R. (2008), H_2O subduction beyond arcs, *Geochem. Geophys. Geosyst.*, *9*, Q03001, doi:10.1029/2007GC001707.
Hacker, B. R., G. A. Abers, and S. M. Peacock (2003), Subduction factory 1. Theoretical mineralogy, densities, seismic wave speeds, and H_2O contents, *J. Geophys. Res.*, *108*(B1), 2029, doi:10.1029/2001JB001127.
Haraguchi, S., T. Ishii, J.-I. Kimura, and Y. Ohara (2003), Formation of tonalite from basaltic magma at the Komahashi-Daini Seamount, northern Kyushu-Palau Ridge in the Philippine Sea, and growth of Izu-Ogasawara (Bonin)-Mariana arc crust, *Contrib. Mineral. Petrol.*, *145*, 151–168.
Hart, S. R. (1984), A large scale isotope anomaly in the Southern Hemisphere mantle, *Nature*, *309*, 753–757.
Hauff, F., K. Hoernle, and A. Schmidt (2003), Sr-Nd-Pb composition of Mesozoic Pacific oceanic crust (Site 1149 and 801, ODP Leg 185): Implications for alteration of ocean crust and the input into the Izu-Bonin-Mariana subduction system, *Geochem. Geophys. Geosyst.*, *4*(8), 8913, doi:10.1029/2002GC000421.
Hermann, J., and D. Rubatto (2009), Accessory phase control on the trace element signature of sediment melts in subduction zones, *Chem. Geol.*, *265*, 512–526.
Hermann, J., and C. J. Spandler (2008), Sediment melts at sub-arc depths: An experimental study, *J. Petrol.*, *49*, 717–740.
Herzberg, C. (2011), Identification of source lithology in the Hawaiian and Canary Islands: Implications for origins, *J. Petrol.*, *52*, 113–146.
Herzberg, C., and P. D. Asimow (2008), Petrology of some oceanic island basalts: PRIMELT2.XLS software for primary magma calculation, *Geochem. Geophys. Geosyst.*, *9*, Q09001, doi:10.1029/2008GC002057.
Hickey-Vargas, R. L. (1998), Origin of the Indian Ocean-type isotopic signature in basalts from Philippine Sea plate spreading centers: An assessment of local versus large-scale processes, *J. Geophys. Res.*, *103*(B9), 20,963–20,979.
Hirschmann, M. M., M. S. Ghiorso, F. A. Davis, S. M. Gordon, S. Mukherjee, T. L. Grove, M. Krawczynski, E. Medard, and C. B. Till (2008), Library of Experimental Phase Relations (LEPR): A database and Web portal for experimental magmatic phase equilibria data, *Geochem. Geophys. Geosyst.*, *9*, Q03011, doi:10.1029/2007GC001894.
Hoang, N., and K. Uto (2003), Geochemistry of Cenozoic basalts in the Fukuoka district (northern Kyushu, Japan): Implications for asthenosphere and lithospheric mantle interaction, *Chem. Geol.*, *198*, 249–268.
Hochstaedter, A., J. Gill, R. Peters, P. Broughton, and P. Holden (2001), Across-arc geochemical trends in the Izu-Bonin arc: Contributions from the subducting slab, *Geochem. Geophys. Geosyst.*, *2*(3), 1019, doi:10.1029/2000GC000105.
Hyndman, R., and S. M. Peacock (2003), Serpentinization of the forearc mantle, *Earth Planet. Sci. Lett.*, *212*, 417–432.
Iizumi, S., S. Otani, and K. Hara (1999), Sr and Nd isotope ratios of Middle Miocene volcanic rocks from Shimane Peninula, San'in district, Southwest Japan, *Mem. Geol. Soc. Jpn.*, *53*, 389–391.
Ikawa, T., M. Onimura, T. Imaoka, and H. Kagami (1999), Petrography and Sr and Nd isotope ratios of the Sekidogadake Granophyre and associated rhyolites, central part of Yamaguchi Prefecture, Southwest Japan, *Mem. Geol. Soc. Jpn.*, *53*, 333–348.
Imaoka, T., K. Kiminami, K. Nishida, M. Takemoto, T. Ikawa, H. Kagami, and S. Iizumi (2011), K-Ar age and geochemistry of the SW Japan Paleogene cauldron cluster: Implications for Eocene-Oligocene thermo-tectonic reactivation, *J. Asian Earth Sci.*, *40*, 509–533.
Ishioka, J., and S. Iizumi (2003), Petrochemical and Sr-Nd isotope investigations of Cretaceous intrusive rocks and their enclaves in the Togouchi-Yoshiwa district, northwest Hiroshima prefecture, SW Japan, *Geochem. J.*, *37*, 449–470.
Ishizuka, O., et al. (2006), Early stages in the evolution of Izu-Bonin arc volcanism: New age, chemical, and isotopic constraints, *Earth Planet. Sci. Lett.*, *250*, 385–401.
Ishizuka, O., R. N. Taylor, M. Yuasa, and Y. Ohara (2011), Making and breaking an island arc: A new perspective from the Oligicene Kyushu-Palau arc, Philippine Sea, *Geochem. Geophys. Geosyst.*, *12*, Q05005, doi:10.1029/2010GC003440.
Iwamori, H. (1991), Zonal structure of Cenozoic basalts related to mantle upwelling in southwest Japan, *J. Geophys. Res.*, *96*(B4), 6157–6170.
Iwamori, H. (1992), Degree of melting and source composition of Cenozoic basalts in southwest Japan: Evidence for mantle upwelling by flux melting, *J. Geophys. Res.*, *97*(B7), 10,983–10,995.
Jacques, G., K. Hoernle, J. B. Gill, F. Hauff, H. Wehrmann, D. Garbe-Schönberg, P. van den Bogaard, I. Bindeman, and L. E. Lara (2013), Across-arc geochemical variations in the Southern Volcanic Zone, Chile (34.5–38.0°S): Constraints on mantle wedge and slab input compositions, *Geochim. Cosmochim. Acta*, *123*, 218–243.
Johannes, W., and F. Holtz (1996), *Petrogenesis and Experimental Petrology of Granitic Rocks*, 335 pp., Springer, Heiderberg, Germany.
Kagami, H., and T. Imaoka (2008), Investigation of petrogenesis of granites based on Sr and Nd isotopes, *Earth Sci.*, *62*, 131–138.
Kagami, H., H. Honma, T. Shirahase, and T. Nureki (1988), Rb-Sr whole rock isochron ages of granites from northern Shikoku and Okayama, Southwest Japan: Implications for the migration of the Late Cretaceous to Paleogene igneous activity in space and time, *Geochem. J.*, *22*, 69–79.
Kagami, H., S. Iizumi, Y. Tainosho, and M. Owada (1992), Spatial variations of Sr and Nd isotope ratios of Cretaceous-Paleogene granitoid rocks, Southwest Japan Arc, *Contrib. Mineral. Petrol.*, *112*, 165–177.
Kagami, H., et al. (2000), Continental basalts in the accretionary complexes of the South-west Japan arc: Constraints from geochemival and Sr amd Nd isotopic data of metadiabase, *Island Arc*, *9*, 3–20.
Kakubuchi, S., T. Nagao, and K. Nagao (2000), K-Ar ages and magmatic history of the Abu Monogenetic Volcano Group, *Jpn. Mag. Mineral. Petrol. Sci.*, *29*, 191–198.
Katsumata, A. (2010), Depth of the Moho discontinuity beneath the Japanese islands estimated by traveltime analysis, *J. Geophys. Res.*, *115*, B04303, doi:10.1029/2008JB005864.
Katsumata, A., and N. Kamaya (2003), Low-frequency continuous tremor around the Moho discontinuity away from volcanoes in the southwest Japan, *Geophys. Res. Lett.*, *30*(1), 1020, doi:10.1029/2002GL0159812.
Katz, R. F., M. Spiegelman, and C. H. Langmuir (2003), A new parameterization of hydrous mantle melting, *Geochem. Geophys. Geosyst.*, *4*(9), 1073, doi:10.1029/2002GC000433.
Kay, R. W. (1980), Volcanic arc magmas: Implications of a melting-mixing model for element recycling in the crust-upper mantle system, *J. Geol.*, *88*, 497–522.
Kelemen, P. B., S. R. Hart, and S. Bernstein (1998), Silica enrichment in the continental upper mantle via melt/rock reaction, *Earth Planet. Sci. Lett.*, *164*, 387–406.
Kelemen, P. B., G. M. Yogodzinski, and D. W. Scholl (2013), Along-strike variation in the Aleutian island arc: Genesis of high-Mg# andesite and implications for continental crust, in *Inside the Subduction Factory*, edited by J. Eiler, AGU, Washington, D. C., 223–276, doi:10.1029/138GM11.

Kelley, K. A., T. Plank, J. Ludden, and H. Staudigel (2003), Composition of altered oceanic crust at ODP Sites 801 and 1149, *Geochem. Geophys. Geosyst.*, *4*(6), 8910, doi:10.1029/2002GC000435.
Kelley, K. A., T. Plank, S. Newman, E. M. Stolper, T. L. Grove, S. Parman, and E. H. Hauri (2010), Mantle melting as a function of water content beneath the Mariana arc, *J. Petrol.*, *51*, 1711–1738.
Kessel, R., M. W. Schmidt, P. Ulmer, and T. Pettke (2005), Trace element signature of subduction-zone fluids, melts and superctical liquids at 120–180 km depth, *Nature*, *437*, 724–727.
Kimura, J.-I. (2012), *Arc Basalt Simulator (ABS) Version 3*, EarthChem Library. [Available at: http://www.earthchem.org/library.]
Kimura, J.-I., and Y. Yamada (1996), Evaluation of major and trace element XRF analyses using flux to sample ratio of two to one glass beads, *J. Mineral. Petrol. Econ. Geol.*, *91*, 62–72.
Kimura, J.-I., and T. Yoshida (2006), Contributions of slab fluid, mantle wedge and crust to the origin of Quaternary lavas in the NE Japan arc, *J. Petrol.*, *47*, 2185–2232.
Kimura, J.-I., and R. J. Stern (2008), Neogene volcanism of the Japan island arc: The K-h relationship revisited, in *Ores and Orogenesis: Circum-Pacific Tectonics, Geologic Evolution, and Ore Deposits: Arizona Geological Society Digest 22*, edited by J. E. Spencer and S. R. Titley, pp. 187–202, Arizona Geological Society, Tucson, Arizona.
Kimura, J.-I., Y. Takaku, and T. Yoshida (1995), Igneous rock analysis using ICP-MS with internal standardization, isobaric ion overlap correction, and standard addition methods, *Sci. Rep. Fukushima Univ.*, *56*, 1–12.
Kimura, J.-I., W. I. Manton, C.-H. Sun, S. Iizumi, T. Yoshida, and R. J. Stern (2001), Chemical diversity of the Ueno Basalts, central Japan: Identification of mantle and crustal contributions to arc basalts, *J. Petrol.*, *43*, 1923–1946.
Kimura, J.-I., M. Kawahara, and S. Iizumi (2003a), Lead isotope analysis using TIMS following single column-single bead Pb separation, *Geosci. Rep. Shimane Univ.*, *22*, 49–53.
Kimura, J.-I., et al. (2003b), Late Cenozoic volcanic activity in the Chugoku area, Southwest Japan arc during back arc basin opening and reinitiation of subduction, *Island Arc*, *12*, 22–45.
Kimura, J.-I., R. J. Stern, and T. Yoshida (2005a), Reinitiation of subduction and magmatic responces in SW Japan during Neogene time, *Geol. Soc. Am. Bull.*, *117*, 969–986.
Kimura, J.-I., M. Tateno, and I. Osaka (2005b), Geology and geochemistry of Karasugasen lava dome, Daisen-Hiruzen Volcano Group, southwest Japan, *Island Arc*, *14*, 115–136.
Kimura, J.-I., T. W. Sisson, N. Nakano, M. L. Coombs, and P. W. Lipman (2006), Isotope geochemistry of early Kilauea magmas from the submarine Hilina bench: The nature of Hilina mantle component, *J. Volcanol. Geotherm. Res.*, *151*, 51–72, doi:10.1016/j.jvolgeores.2005.1007.1024.
Kimura, J.-I., P. van Keken, B. R. Hacker, H. Kawabata, T. Yoshida, and R. J. Stern (2009), Arc Basalt Simulator (ABS) version 2, a simulation model for slab dehydration, fluid-mantle reaction, and fluid-fluxed mantle melting for arc basalts: Modeling scheme and application, *Geochem. Geophys. Geosyst.*, *10*, Q09004, doi:10.1029/2008GC002217.
Kimura, J.-I., J. R. K. Adam, M. Rowe, N. Nakano, M. Katakuse, P. van Keken, B. Hacker, and R. J. Stern (2010), Origin of cross-chain geochemical variation in Quaternary lavas from northern Izu arc: A quantitative mass balance approach on source identification and mantle wedge processes, *Geochem. Geophys. Geosyst.*, *11*, Q10011, doi:10.1029/2010GC003050.
Kita, S., T. Okada, J. Nakajima, T. Matsuzawa, and A. Hasegawa (2006), Existence of a seismic belt in the upper plane of the double seismic zone extending in the along-arc direction at depths of 70–100 km beneath NE Japan, *Geophys. Res. Lett.*, *33*, L24310, doi:10.1029/2006GL028239.
Kogiso, T., M. M. Hirschmann, and M. Pertermann (2004), High-pressure partial melting of mafic lithologies in the mantle, *J. Petrol.*, *45*, 2407–2422.
Kuritani, T., E. Ohtani, and J.-I. Kimura (2011), Intensive hydration of the mantle transition zone beneath China caused by ancient slab stagnation, *Nat. Geosci.*, *4*, 713–716.
Kushiro, I. (1969), The system forsterite–diopside–silica with and without water at high pressures, *Am. J. Sci.*, *267A*, 269–294.
Kushiro, I. (1973), Origin of some magmas in oceanic and circum-oceanic regions, *Tectonophysics*, *17*, 211–222.
LaTourrette, T., R. L. Hervig, and J. R. Holloway (1995), Trace element partitioning between amphibole, phlogopite, and basanite melt, *Earth Planet. Sci. Lett.*, *135*, 13–30.
Leeman, W. P., J. F. Lewis, R. C. Evarts, R. M. Conrey, and M. A. Streck (2005), Petrologic constraints on the thermal structure of the Cascades arc, *J. Volcanol. Geotherm. Res.*, *140*, 67–105.
Li, Y.-B., et al. (2013), High-Mg adakite and low-Ca boninite from a Bonin fore-arc seamount: Implications for the reaction between slab melts and depleted mantle, *J. Petrol.*, *54*(6), 1149–1175, doi:10.1093/petrology/egt1008.
Macpherson, C. G., S. T. Dreher, and M. F. Thirlwall (2006), Adakites without slab melting: High pressure differentiation of island arc magma, Mindanao, the Philippines, *Earth Planet. Sci. Lett.*, *243*, 581–593.
Mahoney, S. H., L. M. Wallace, M. Miyoshi, P. Villamor, R. S. J. Sparks, and T. Hasenaka (2011), Volcano-tectonic interactions during rapid plate-boundary evolution in the Kyushu region, *SW Japan*, Geol. Soc. Am. Bull., *123*, 2201–2223.
Martin, H., R. H. Smithies, R. Raap, J.-F. Moyden, and D. Champion (2005), An overview of adakite, tonalite-trondhjemite-granodiorite (TTG), and sanukitoid: Relationships and some implications for crustal evolution, *Lithos*, *79*, 1–24.
Maruyama, S., A. Hasegawa, M. Santosh, T. Kogiso, S. Omori, H. Nakamura, K. Kawai, and D. Zhao (2009), The dynamics of big mantle wedge, magma factory, and metamorphic–metasomatic factory in subduction zones, *Gondowana Res.*, *16*, 414–430.
Matsumoto, I., Y. Sawada, and H. Kagami (1994), Rb-Sr isochron ages of Cretaceous Kisa Volcanics and granitoids in the central Chugoku district, Southwest Japan, and their geological significance, *J. Geol. Soc. Jpn.*, *100*, 399–407.
Merzbacher, C., and D. H. Eggler (1984), A magmatic geohygrometer: Application to Mount St. Helens and other dacitic magmas, *Geology*, *12*, 587–590.
Miyake, Y. (1994), Geochemistry of igneous rocks of Shimane peninsula, formed within a Miocene back-arc rifting zone at the Japan Sea margin, *Geochem. J.*, *28*, 451–472.
Morris, P. A. (1995), Slab melting as an explanation of Quaternary volcanism and aseismicity in southwest Japan, *Geology*, *23*, 395–398.
Moyen, J.-F. (2009), High Sr/Y and La/Yb ratios: The meaning of the "adakitic signature," *Lithos*, *112*, 556–574.
Moyen, J.-F., and G. Stevens (2006), Experimental constraints on TTG petrogenesys: Implications for Archean geodynamics, in *Archean Geodynamics and Environments*, edited by K. Benn et al., pp. 149–175, AGU, Washington, D. C., doi:10.1029/164GM11.
Müntener, O., P. B. Kelemen, and T. L. Grove (2001), The role of H_2O during crystallization of primitive arc magmas under uppermost mantle conditions and genesis of igneous pyroxinites: An experimental study, *Contrib. Mineral. Petrol.*, *141*, 643–658.
Nagao, T., N. Fujibayashi, H. Kagami, K. Tazaki, and S. Takada (1990), Origin of the Sr-rich Cenozoic alkali basalts in Yokota area, Chugoku Mountains, Southwest Japan, *J. Geol. Soc. Jpn.*, *96*, 795–803.

Nakajima, J., and A. Hasegawa (2007), Subduction of the Philippine Sea plate beneath southwestern Japan: Slab geometry and its relationship to arc magmatism, *J. Geophys. Res.*, *112*, B08306, doi:10.1029/2006JB004770.
Obara, K. (2002), Nonvolcanic deep tremor associated with subduction in southwest Japan, *Science*, *296*, 1679–1681.
Okino, K., Y. Shimakawa, and S. Nagaoka (1994), Evolution of the Shikoku Basin, *J. Geomagn. Geoelectr.*, *46*, 463–479.
Omori, S., S. Kita, S. Maruyama, and M. Santosh (2009), Pressure-temperature conditions of ongoing regional metamorphism beneath the Japanese Islands, *Godwana Res.*, *16*, 458–469.
Ozawa, K. (2001), Mass balance equations for open magmatic systems: Trace element behavior and its application to open system melting in the upper mantle, *J. Geophys. Res.*, *106*(B7), 13,407–13,434.
Ozawa, K., and N. Shimizu (1995), Open-system melting in the upper mantle: Constraints from the Hayachine-Miyamori ophiolite, northeastern Japan, *J. Geophys. Res.*, *100*(B11), 22,315–22,335.
Peacock, S. M., and K. Wang (1999), Seismic consequence of warm versus cool subduction metamorphism: Examples from southwest and northeast Japan, *Science*, *286*, 937–939.
Pearce, J. A., and I. J. Parkinson (1993), Trace element models for mantle melting: Application to volcanic arc petrogenesis, in *Magmatic Processes and Plate Tectonics, Geol. Soc. Spec. Publ., 76*, edited by H. M. Prichard et al., pp. 373–403. The Geological Society, Piccadilly, London.
Pearce, J. A., P. D. Kempton, G. M. Nowell, and S. R. Noble (1999), Hf-Nd element and isotope perspective on the nature and provenance of mantle and subduction components in Western Pacific Arc-Basin systems, *J. Petrol.*, *40*, 1579–1611.
Pilet, S., M. L. Baker, O. Müntener, and E. M. Stolper (2011), Monte Carlo simulations of metamorphic enrichment in the lithosphere and implicaitons for the source of alkaline basalts, *J. Petrol.*, *52*, 1415–1442.
Plank, T., L. B. Cooper, and C. E. Manning (2009), Emerging geothermometers for estimating slab surface temperatures, *Nat. Geosci.*, *2*, 611–615.
Plank, T., K. A. Kelley, M. M. Zimmer, E. H. Hauri, and P. J. Wallace (2013), Why do mafic arc magmas contain ~4 wt% water on average?, *Earth Planet. Sci. Lett.*, *364*, 168–179.
Pouclet, A., J.-S. Lee, P. Vidal, B. Cousens, and H. Bellon (1995), Cretaceous to Cenozoic volcanism in South Korea and in the Sea of Japan: Magmatic constraints on the opening of the back-arc basin, in *Volcanism Associated with Extension at Consuming Plate Margins, Geol. Soc. Spec. Publ., 81*, edited by J. L. Smellie, pp. 169–191. The Geological Society, Piccadilly, London.
Resanov, A. I., H. Kagami, and S. Iizumi (1994), Rb-Sr isochron ages of Cretaceous—Paleogene granitoid rocks in the central part of the Chugoku district, Southwest Japan, *J. Geol. Soc. Jpn.*, *100*, 651–657.
Rollinson, H. (1993), *Using Geochemical Data: Evaluation, Presentation, Interpretation*, Addison-Wesley, Essex, U. K.
Roser, B. P., J.-I. Kimura, and K. Hisatomi (2000), Whole-rock elemental abundances in sandstones and mudrocks from the Tanabe Group, Kii Peninsula, Japan., *Geosci. Rep. Shimane Univ.*, *19*, 101–112.
Sakuyama, M. (1984), Magma mixing and magma plumbing systems in island arcs, *Bull. Volcanol.*, *47*, 685–703.
Sano, Y., A. Kameda, N. Takahata, J. Yamamoto, and J. Nakajima (2009), Tracing extinct spreading center in SW Japan by helium-3 emanation, *Chem. Geol.*, *266*, 50–56.
Sato, D., I. Matsumoto, and A. Kamei (2011), Petrology and bulk rock chemical composition of the Wakurayama Dacite from Matsue City, Shimane Prefecture, sowthwest Japan, *J. Geol. Soc. Jpn.*, *117*(8), 439–450.
Sato, M., K. Shuto, M. Uematsu, T. Takahashi, M. Ayabe, K. Takanashi, H. Ishimoto, and H. Kawabata (2013), Origin of Late Oligocene to Middle Miocene adakitic andesites, high magnesian andesites and basalts from the back-arc margin of the SW and NE Japan arcs, *J. Petrol.*, *54*, 481–524.
Schmidt, M. W., D. Vielzeuf, and E. Auzanneau (2004), Melting and dissolution of subducting crust at high pressures: The key role of white mica, *Earth Planet. Sci. Lett.*, *228*, doi:10.1016/j.epsl.2004.1009.1020.
Seno, T., and Maruyama, S. (1984), Paleogeographic reconstructions and origin of the Philippine Sea, *Tectonophysics*, *102*, 53–84.
Shaw, D. M. (2000), Continuous (dynamic) melting theoly revisited, *Can. Mineral.*, *38*, 1041–1063.
Shimoda, G., Y. Tatsumi, S. Nohda, K. Ishizaka, and B. M. Jahn (1998), Setouchi high-Mg andesites revisited: Geochemical evidence for melting of subducting sediments, *Earth Planet. Sci. Lett.*, *160*, 479–492.
Shinjoe, H. (1997), Origin of the granodiolite in the forearc region of southwest Japan: Melting of the Shimanto accretionary prism, *Chem. Geol.*, *134*, 237–255.
Sisson, T. W., and T. L. Grove (1993), Experimental investigations of the role of H_2O in calc-alkaline differentiation and subduction zone magmatism, *Contrib. Mineral. Petrol.*, *113*, 143–166.
Sisson, T. W., J.-I. Kimura, and M. L. Coombs (2009), Basanite-bepherinite suite from early Kilauea: Carbonated melts of phlogopite-garnet peridotite at Hawaii's leading magmatic edge, *Contrib. Mineral. Petrol.*, *158*, 803–829.
Skora, S., and J. Blundy (2010), High-pressure hydrous phase relations of radiolarian clay and implications for the involvement of subducted sediment in arc magmatism, *J. Petrol.*, *51*, 2211–2243.
Skora, S., and J. Blundy (2012), Monazite solubility in hydrous silicic melts at high pressure conditions relevant to subduction zone metamorphism, *Earth Planet. Sci. Lett.*, *321–322*, 104–114.
Staudigel, H., T. Plank, B. White, and H.-U. Schmincke (1996), Geochemical fluxes during seafloor alteration of the basaltic upper crust: DSDP Sites 417 and 418, in *Subduction Top to Bottom*, edited by G. E. Bebout et al., AGU, Washington, D. C., pp. 19–38, doi:10.1029/GM096p0019.
Stevenson, R. K., and P. J. Patchett (1990), Implications for the evolution of continental crust from Hf isotope systematics of Archean detrital zircons, *Geochim. Cosmochim. Acta*, *54*, 1683–1697.
Straub, S. M., A. B. LaGatta, A. L. M.-D. Pozzo, and C. H. Langmuir (2008), Evidence from high-Ni olivines for a hybridized peridotite/pyroxenite source for orogenic andesites from the central Mexican Volcanic Belt, *Geochem. Geophy. Geosyst.*, *9*, Q03007, doi:10.1029/2007GC001583.
Straub, S. M., A. Gomez-Tuen, F. M. Stuart, G. F. Zellmer, R. Espinasa-Perena, Y. Cai, and Y. Iizuka (2011), Formation of hybrid arc andesites beneath thick continental crust, *Earth Planet. Sci. Lett.*, *303*, 337–347.
Streck, M. J., W. P. Leeman, and J. Chesley (2007), High-magnesian andesite from Mount Shasta: A product of magma mixing and contamination, not a primitive mantle melt, *Geology*, *35*, 351–354.
Sun, C.-H., R. J. Stern, T. Yoshida, and J.-I. Kimura (1998), Fukutoku-oka-no-ba volcano: A new perspective on the alkalic volcano province in the Izu-Bonin-Mariana arc, *Island Arc*, *7*, 732–442.
Sun, S.-s., and W. F. McDonough (1989), Chemical and isotopic systematics of oceanic basalts: Implications for mantle composition and processes., in *Magmatism in the Ocean Basins, Geol. Soc., Spec. Publ., 42*, edited by A. D. Saunders and M. J. Norry, pp. 313–345, The Geological Society, Piccadilly, London.
Syracuse, E. M., P. E. v. Keken, and G. A. Abers (2010), The global range of subduction zone thermal models, *Phys. Earth Planet. Inter.*, doi:10.1016/j.pepi.2010.1002.1004.

Takagi, T., and H. Kagami (1995), Rb-Sr isochron ages and initial Sr isotope ratios of Ukan granodiorite and Kayo granite, central Okayama prefecture, southwest Japan, *Bull. Geol. Surv. Jpn.*, *46*, 219–224.

Tamaki, K., K. Suyehiro, J. Allan, J. C. Ingle, and K. A. Pisciotto (1992), Tectonic synthesis and implications of Japan sea ODP Drilling, in *Proceedings of Ocean Drilling Program, Scientific Results*, edited by K. Tamaki et al., pp. 1333–1348, Ocean Drill. Prog., College Station, Tex.

Tamura, Y., H. Yuhara, and T. Ishii (2000), Primary arc basalts from Daisen volcano, Japan: Equilibrium crystal fractionation versus disequilibrium fractionation during supercooring, *J. Petrol.*, *41*, 431–448.

Tamura, Y., M. Yuhara, T. Ishii, N. Irino, and H. Shukuno (2003), Andesites and dacites from Daisen volcano, Japan: Partial-to-total remelting of an andesitic magma body, *J. Petrol.*, *44*, 2243–2260.

Tatsumi, Y., and T. Koyaguchi (1989), An absalokite from a phlogopite lherzorite source, *Contrib. Mineral. Petrol.*, *102*, 34–40.

Tatsumi, Y., and S. Eggins (1995), *Subduction Zone Magmatism*, Blackwell Sci, Boston.

Tatsumi, Y., and T. Hanyu (2003), Geochemical modeling of dehydration and partial melting of subducting lithosphere: Toward a comprehensive understanding of high-Mg andesite formation in the Setouchi volcanic belt, SW Japan, *Geochem. Geophys. Geosyst.*, *4*(9), 1081, doi:10.1029/2003GC000530.

Tatsumi, Y., R. Arai, and K. Ishizaka (1999), The petrology of a melilite-olivine nephelinite from Hamada, SW Japan, *J. Petrol.*, *40*, 497–509.

Tatsumi, Y., H. Shukuno, K. Tani, N. Takahashi, S. Kodaira, and T. Kogiso1 (2008a), Structure and growth of the Izu-Bonin-Mariana arc crust: 2. Role of crust-mantle transformation and the transparent Moho in arc crust evolution, *J. Geophys. Res.*, *113*, B02203, doi:10.1029/2007JB005121.

Tatsumi, Y., T. Takahashi, Y. Hirahara, Q. Chang, T. Miyazaki, J.-I. Kimura, M. Ban, and A. Sakayori (2008b), New Insights into andesite genesis: The role of mantle-derived calc-alkalic and crust-derived tholeiitic melts in magma differentiation beneath Zao Volcano, NE Japan, *J. Petrol.*, *49*, 1971–2008, doi:10.1093/prtrology/egn1055.

Tiepolo, M., R. Vannucci, P. Bottazzi, R. Oberti, A. Zanetti, and S. Foley (2000a), Partitioning of rare earth elements,Y, Th, U, and Pb between pargasite, kaersutite, and basanite to trachyte melts: Implications for percolated and veined mantle, *Geochemi. Geophys. Geosyst.*, *1*(8), 1039, doi:10.1023/2000GC000064.

Tiepolo, M., R. Vannucci, R. Oberti, S. Foley, P. Bottazzi, and A. Zanetti (2000b), Nb and Ta incorporation and fractionation in titanian pargasite and kaersutite: Crystal-chemical constraints and implications for natural systems, *Earth Planet. Sci. Lett.*, *176*, 185–201.

Tiepolo, M., R. Oberti, A. Zanetti, R. Vannucci, and S. Foley (2007), Trace-element partitioning between amphibole and silicate melt, in *Amphiboles: Crystal Chemistry, Occurrence, and Health Issues: Reviews in Mineralogy and Geochemistry* edited by F. C. Hawthorne et al., pp. 417–452, Mineral. Soc. Am. and Geochem. Soc. The Mineralogical Society of America, Chantilly, Virginia.

Till, C. B., T. L. Grove, and M. J. Krawczynski (2012a), A melting model for variably depleted and enriched lherzolite in the plagioclase and spinel stability fields, *J. Geophyi. Res.*, *117*, B06206, doi:10.1029/2011JB009044.

Till, C. B., T. L. Grove, and A. C. Withers (2012b), The beginnings of hydrous mantle wedge melting, *Contrib. Mineral. Petrol.*, *163*, 669–688.

Tollstrup, D. L., and J. B. Gill (2005), Hafnium systematics of the Mariana arc: Evidence for sediment melt and residual phases, *Geology*, *33*, 737–740.

Tollstrup, D. L., J. B. Gill, A. J. R. Kent, D. Prinkey, R. Williams, Y. Tamura, and O. Ishizuka (2010), Across-arc geochemical trends in the Izu-Bonin arc: Contributions from the subducting slab, revisited, *Geochem. Geophys. Geosyst.*, *11*, Q01X10, doi:10.1029/2009GC002847.

Torii, M., A. Hayashida, and Y. Otofuji (1986), Rotation of the Southwest Japan arc and formation of the Japan Sea, in *Development of the Japanese Islands: History as a Mobile Belt and the Present State*, edited by A. Taira and K. Nakamura, pp. 235–240, Iwanami Shoten, Tokyo.

Tsuchiya, N., S. Suzuki, J.-I. Kimura, and H. Kagami (2005), Evidence for slabmelt/mantle reaction: Petrogenesis of Early Cretaceous and Eocene high-Mg andesites from the Kitakami Mountains, Japan, *Lithos*, *79*, 179–206.

Tsuji, Y., J. Nakajima, and A. Hasegawa (2008), Tomographic evidence for hydrated oceanic crust of the Pacific slab beneath northeastern Japan: Implications for water transportation in subduction zones, *Geophys. Res. Lett.*, *35*, L14308, doi:10.1029/2008GL034461.

Tsukui, M., H. Nishido, and K. Nagao (1985), K-Ar ages of the Hiruzen Volcano Group and Daisen Volcano, *J. Geol. Soc. Jpn.*, *91*, 279–288.

Umino, S., and I. Kushiro (1989), Experimental studies on boninite petrogenesis, in *Boninite and Related Rocks*, edited by A. J. Crawford, pp. 89–109, Unwin Hyman, London.

Uto, K., E. Takahashi, E. Nakamura, and I. Kaneoka (1994), Geochronology of alkali volcanism in Oki-Dogo Island, southwest Japan: Geochemical evolution of basalts related to the opening of the Japan Sea, *Geochem. J.*, *28*, 431–449.

van Keken, P. E., B. Kiefer, and S. M. Peacock (2002), High resolution models of subduction zones: Implications for mineral dehydration reactions and the transport of water into the deep mantle, *Geochem. Geophys. Geosyst.*, *3*(10), 1056, doi:10.1029/2001GC000256.

van Keken, P. E., B. R. Hacker, E. M. Syracuse, and G. A. Abers (2011), Subduction factory: 4. Depth-dependent flux of H_2O from subduction slabs worldwide, *J. Geophys. Res.*, *116*, B01401, doi:10.1029/2010JB00922.

Willbold, M., and A. Stracke (2006), Trace element composition of mantle end-members: Implications for recycling of oceanic and upper and lower continental crust, *Geochem. Geophys. Geosyst.*, *7*, Q04004, doi:10.1029/2005GC001005.

Wilson, M. (1989), *Igneous Petrogenesis: A Grobal Tectonic Approach*, 466 pp., Unwin-Hyman, London.

Wood, B. J., and J. D. Blundy (1997), A predictive model for rare earthe element partitioning between clinopyroxene and anhydrous silicate melt, *Contrib. Mineral. Petrol.*, *129*, 166–181.

Workman, R. K., and S. R. Hart (2005), Major and trace element composition of the depleted MORB mantle (DMM), *Earth Planet. Sci. Lett.*, *231*, 53–72.

Yamada, R., T. Yoshida, and J.-I. Kimura (2013), Chemical and isotopic characteristics of the Kuroko-forming volcanism, *Resour. Geol.*, *62*, 369–383.

Yamamoto, T., and N. Hoang (2009), Synchronous Japan Sea opening Miocene fore-arc volcanism in the Abukuma Mountains, NE Japan: An advancing hot asthenosphere flow versus Pacific slab melting, *Lithos*, *112*, 575–590.

Yamauchi, S., Y. Sawada, A. Takasu, H. Komuro, H. Murakami, S. Kobayashi, and R. Tayama (2009), Geology of the Saigo District with 1/50000 scale geological map, *Geol. Surv. Jpn.*, 121.

Yogodzinski, G. M., R. W. Kay, O. N. Volynets, A. V. Koloskov, and S. M. Kay (1995), Magnesian andesite in the western Aleutian Komandorsky region: Implications for slab melting and processes in the mantle wedge, *Geol. Soc. Am. Bull.*, *107*, 505–519.

Yogodzinski, G. M., J. M. Lees, T. G. Churikova, F. Dorendorf, G. Welner, and O. N. Volynets (2001), Geochemical evidence for the melting of subducting oceanic lithosphere at plate edges, *Nature*, *409*, 500–504.

Yuge, T., T. Imaoka, and S. Iizumi (1998), Whole-rock chemistry and Sr and Nd isotope ratios of Cretaceous rhyolite and granodiorite in Abu district, Yamaguchi Prefecture, Southwest Japan, *J. Geol. Soc. Jpn.*, *104*, 159–170.

Yuhara, M., Y. Takahashi, and H. Kagami (1998), Rb-Sr whole rock isochron ages and source materials of granitic rocks in Awaji Island, southwest Japan arc, *Bull. Geol. Surv. Jpn.*, *49*, 477–491.

Yuhara, M., T. Miyazaki, H. Kagami, and M. Yuhara (2003), Rb-Sr and K-Ar geochronology and petrogenesis of the Aji granite in the eastern Sanuki district, Ryoke belt, southwest Japan, *J. Mineral. Petrol. Sci.*, *98*, 19–30.

Zellmer, G. F., Y. Iizuka, M. Miyoshi, Y. Tamura, and Y. Tatsumi (2012), Lower crustal H_2O controls on the formation of adakitic melts, *Geology*, *40*, 487–490, doi:10.1130/G32912.32911.

Zhao, D., T. Yanada, A. Hasegawa, N. Umino, and W. Wei (2012), Imaginng the subducting slabs and mantle upwelling under the Japan Islands, *Geophys. J. Int.*, *190*, 816–828.